Inverse and Transient Thermal Analysis for Rapid Hyperthermia Therapy Planning, Delivery and Evaluation

by

Jialun He

B.S. Huazhong University of Science and Technology (1988)
M.S. Institute of Engineering Thermophysics, Chinese Academy of Sciences (1991)

Submitted to the Department of Mechanical Engineering
In Partial Fulfillment of the Requirements for the Degree of

Doctor of Philosophy

at the

Massachusetts Institute of Technology

June 2003

Signature of Author__________
Department of Mechanical Engineering
May 9, 2003

Certified by__________
Dr. H. Frederick Bowman
Director, Hyperthermia Program, Harvard-MIT Division of HST
Thesis Supervisor

Accepted by__________
Professor Ain, A. Sonin
Chairman, Department Committee on Graduate Students

Inverse and Transient Thermal Analysis for Rapid Hyperthermia Therapy Planning, Delivery and Evaluation

by

Jialun He

Submitted to the Department of Mechanical Engineering
In Partial Fulfillment of the Requirements for the Degree of Doctor of Philosophy

Abstract

The efficacy of hyperthermia therapy can be enhanced if a thermal management system is available for therapy planning, delivery and evaluation. The integrated thermal management system is not yet available, though some components of the system have been developed. For example, MIT Hyperthermia Program has developed algorithms for fast forward temperature computation, which include hyperthermia thermal model using Finite Basis Element Method (FBEM) and power model for ultrasound applicators. These components can provide simulated prediction prior to hyperthermia therapy and process evaluation after the therapy. This thesis describes the development of other critical components for the thermal management system: the inverse thermal analysis and the transient thermal analysis.

For the inverse thermal analysis, iterative algorithms are used for both the Finite Basis Element Method (FBEM) and Finite Element Method (FEM) to predict the desired power field if the optimal temperature field is given. The simulation results show that both FBEM and FEM predict the optimal power deposition field accurately. FBEM is faster than FEM by an order of magnitude for moderate root mean square (RMS) errors. For the combined inverse thermal analysis that links the optimal temperature field to the control parameters of the energy delivery machine, an inverse algorithm based on source superposition has been developed. Numerical simulations with normalized source array for three simple geometry tumor models have been demonstrated. The simulation results show that the inverse procedure can estimate the optimal control magnitude of each individual source to achieve the optimal temperature field with less than 1°C of RMS error.

For the transient thermal analysis, a fast algorithm based on source superposition, Green's function solution and Laplace transform has been developed. Various practical transient elements have been formulated. The method is validated by the comparisons to the exact solutions of problems with simple geometries. The validation results show that the numerical results approach the exact solutions as the size of the element decreases. The speed-accuracy comparisons show that the computation time per node is about 0.1 second with temperature error around 0.1°C, which makes the algorithm very attractive for real-time temperature reconstruction.

Thesis Supervisor:
Dr. H. Frederick Bowman, Director, Hyperthermia Program, Division of HST
Doctoral Committee:
Drs. Frederick Bowman, Gregory Martin, Borivoje Mikic (Chair), Goran Svensson

Acknowledgements

I would like to first express my deep gratitude to my advisor Dr. H. Frederick Bowman, for his guidance and support in the development of the work, for having faith in me when I struggled. Thanks are also extended to other members of my thesis committee. Dr. Gregory Martin is the frequent source of technical support and information on this project. He provided many useful suggestions and guidelines. I am fortunate to have Prof. Borivoje Mikić in my thesis committee. I learned a lot from the two graduate level heat transfer courses he offered at MIT. I am also honored to have Prof. Goran Svensson in my thesis committee. The MIT community is really supportive. Dr. Daniel Sidney was my officemate. I appreciate his help on my research project.

I would not have had been able to finish a Ph.D. at MIT without the love, understanding and support of my wife, although she occasionally took pity on me for staying at MIT forever. I am also deeply indebted to my parents and parents-in-law for their love and unconditional support. Finally I would like to thank my beautiful and lovely angel, my newborn daughter Anna, for bringing me joy and love during my last year at MIT.

Contents

List of Figures

List of Tables

List of Variables, Functions and Abbreviations

Variables

a	characterized length, Basis Element radius (m)
A	Area, (m^2); or coefficient
Bi	Biot number, $\frac{hL}{k_m}$
c_b	blood specific heat (J/kg-°C)
h	heat transfer coefficient (W/m^2-°C)
h_i	interpolation functions of local coordinates for FEM
k_m	tissue thermal conductivity (W/m-°C)
L	length scale (m)
L_p	tissue perfusion length (m)
N_p	number of perfusion lengths in integration volume radius, dimensionless
Pe	Peclet number, $\frac{\omega\rho_b c_b}{k_m} a^2$
P_f	packing factor, dimensionless
q	heat flux, (W/m^2)
q^B	relative power, $\frac{Q}{k_m}$ (°C/m^2)
q^+	relative power, $\frac{Qa^2}{k_m}$ (°C)
Q	absorbed power (W/m^3)

r	radial coordinate (m)
r^+	dimensionless radial coordinate, $\frac{r}{a}$
R	dimensionless Basis Element coordinate
R'	Basis Element coordinate (m)
R'_+	matching function coordinate (m)
R_+	dimensionless matching function coordinate
R_c	radius of curvature (m)
S	boundary surface (m^2)
s	complex number used in Laplace transform
t	time (s)
t^+	dimensionless time, $\frac{\alpha_m}{a^2}t$
T	temperature elevation above the arterial blood temperature (°C)
u	Green's function (m^{-1})
V	volume (m^3)
V_{int}	integration volume (m^3)
W	clinical perfusion (ml/min-100g)
x	Cartesian coordinate (m)
y	Cartesian coordinate (m)
z	Cartesian coordinate (m)

α	coefficient
α_m	tissue thermal diffusivity (m^2/s)
β	coefficient
γ	coefficient
θ	temperature in complex domain
Θ_0	macroscopic Finite Basis Element (°C)
Θ_j	Finite Basis Element (°C)
κ	dimensionless thermal conductivity
λ	$\sqrt{\frac{\omega\rho_b c_b}{k_m}}$

ρ_b	blood density (kg/m^3)
ω	local perfusion rate (1/s)
Ω	domain

Matrices and Vectors, in **BOLD**

$\boldsymbol{B}$	temperature gradient matrix
$\boldsymbol{H}$	temperature interpolation matrix
$\boldsymbol{J}$	Jacobian matrix
$\boldsymbol{K}$	stiffness matrix
$\boldsymbol{K_T}$	temperature coefficient matrix
$\boldsymbol{K_q}$	power coefficient matrix
$\boldsymbol{M}$	mass matrix
$\boldsymbol{n}$	normal vector (m)
$\boldsymbol{r}$	position vector (m)
$\boldsymbol{r_p}$	position vector of a source center (m)
$\boldsymbol{R_s}$	load matrix
$\boldsymbol{T}$	temperature matrix (°C)

Superscripts

$'$	gradient or transpose matrix (for marix)
$^+$	dimensionless parameter
$-$	virtual parameter in FEM
T	transpose matrix
s	boundary surface
m	mth element

Functions

det	determinant of a matrix
$sinh(x)$	$\frac{1}{2}(e^{x} - e^{-x})$

$cosh(x)$	$\frac{1}{2}(e^{x}+e^{-x})$
$erfc(x)$	$1-erf(x)=1-\frac{2}{\sqrt{\pi}}\int_{0}^{x}e^{-\xi^{2}}d\xi$
$L_1(r^+)$	$\frac{1}{2}[e^{-r^{+}\sqrt{Pe}}erfc(\frac{r^{+}}{2\sqrt{t^{+}}}-\sqrt{Pe\cdot t^{+}})+e^{r^{+}\sqrt{Pe}}erfc(\frac{r^{+}}{2\sqrt{t^{+}}}+\sqrt{Pe\cdot t^{+}})]$
$L_3(r^+)$	$\frac{1}{2\sqrt{Pe}}[e^{-r^{+}\sqrt{Pe}}erfc(\frac{r^{+}}{2\sqrt{t^{+}}}-\sqrt{Pe\cdot t^{+}})-e^{r^{+}\sqrt{Pe}}erfc(\frac{r^{+}}{2\sqrt{t^{+}}}+\sqrt{Pe\cdot t^{+}})]$
$L_4(r^+)$	$e^{-Pe\cdot t^{+}}[2e^{-\frac{r^{+2}}{4t^{+}}}\sqrt{\frac{t^{+}}{\pi}}-r^{+}\cdot erfc(\frac{r^{+}}{2\sqrt{t^{+}}})]$
$L_5(r^+)$	$e^{-Pe\cdot t^{+}}\cdot erfc(\frac{r^{+}}{2\sqrt{t^{+}}})$

Abbreviations

DFCI	Dana-Farber Cancer Institute (located in Boston)
FBEM	Finite Basis Element Method
FEM	Finite Element Method
FSUM	Focused Segmented Ultrasound Machine
JCRT	Joint Center for Radiation Therapy (located in Boston)
RMS	Root Mean Square
SAR	Specific Absorption Rate (volumetric power deposition)

Chapter 1

Introduction

1.1 Hyperthermia

Cancer is a major threat to human life. Researchers throughout the world are looking for improved treatments over the current methods of surgery, radiotherapy, chemotherapy and immunotherapy. Hyperthermia is an experimental cancer treatment that elevates the temperature of tumor tissue to a therapeutic level of 42~43°C for a period of time. Hyperthermia can produce heat-induced cytotoxic response and increase the cytotoxic effects of ionizing radiation and chemotherapeutic drugs to malignant tissue (Gautherie, 1990). Therefore, it is primarily used in conjunction with radiation and drugs to enhance the treatment efficacy (Field and Hand, 1990).

The reasons for using hyperthermia to treat cancer are based primary on the fact that the vasculature and blood supply in cancerous and normal tissues react differently to external heat source. The blood flow is the major mechanism for maintaining a fixed temperature inside human body. The tumor tissue tends to have a reduced capacity of blood flow (Song, 1982). Its temperature tends to be higher when subjected to hyperthermia heat field. On the contrary, in normal tissue, there may be a substantial increase in blood flow to increase the cooling effect and reduce the damage to normal tissue. The deficient supply of blood and nutrients in tumor cells results in the development of hypoxic cells, which are resistant to ionizing radiation. However, those cells are not heat-resistant.

The effectiveness and safety of hyperthermia as a clinical cancer treatment depend on the preferential elevation of tumor temperature to therapeutic levels while restraining the normal tissue temperature to a safe level of less than 40°C. The ideal hyperthermia treatment would deliver and control the thermal dose by non-invasive and open-loop method, as with radiation therapy. Hyperthermia treatment, however, is more complicated than radiation, whereas the latter only depends on energy deposition mechanism, the former depends on both the energy delivery mechanism and energy removal mechanism.

1.2 Project History

This project has a history of more than two decades of continuing research. In the early stage, the focus was on ultrasound device development. In the early 80's, MIT Hyperthermia Center, led by Professor Lele, developed the Steered, Intensity Modulated, Focused Ultrasound System, alias SIMFU (Lele, 1983). In order to deliver energy to deep-seated tumors, an improved ultrasound system, the Focused Segmented Ultrasound Machine (Bowman, 1991), alias FSUM, was developed by Joint Center for Radiation Therapy (JCRT) in the late 80's and early 90's.

With the power delivery machine in place, the focus of the project changed to a more clinical orientation during the 90's. A geometry planning system, called HYPER/Plan, was developed by JCRT. Meanwhile, the MIT Hyperthermia Program, led by Dr. Fred Bowman, concentrated their efforts on thermal dosimetry via quantitative thermal modeling and minimum invasive thermometry.

The ideal quantitative thermal model should be able to provide therapist the tools for treatment planning before the therapy, real time temperature field feedback during the therapy and thermal dose evaluation after the therapy. MIT Hyperthermia Program has carried out a series of projects in this field. Dr. Martin developed a rapid computational model for clinical hyperthermia based on Finite Basis Element Method (FBEM) (Martin, 1995). Mr. Breedlove investigated the heat transfer between blood vessels and perfused tissue during hyperthermia therapy (Breedlove, 1997). Dr. Sidney studied 3-D ultrasound models and thermal field visualization (Sidney, 1997). These models are applicable to steady state forward loop.

The purpose of thermometry is to provide necessary dense temperature and perfusion data for clinical application. MIT Hyperthermia Program has made a series progress in minimum invasive thermometry. Dr. Szajda developed a temperature sensing system (Szajda 1995). Other major progress includes a multi-site perfusion monitoring sub-system (Bodenhofer, 1998) and instrumented hyperthermia biopsy needle (Kim, 1998).

1.3 Motivation

The current hyperthermia treatment system is in its infancy. There are several trial systems. One of the systems, developed partly by MIT Hyperthermia Program through the last decade and currently used in Dana-Farber Cancer Institute (DFCI), has integrated patient geometry and anatomy from CT (computer tomography) scans into a treatment planning system. The equipment performance can be optimized if the tissue thermal response to a thermal dose can be predicted. Therefore, a comprehensive thermal management system, which includes quantitative tissue thermal model, power delivery model for Specific Absorption Rate (SAR), and temperature feedback control model, is highly desirable.

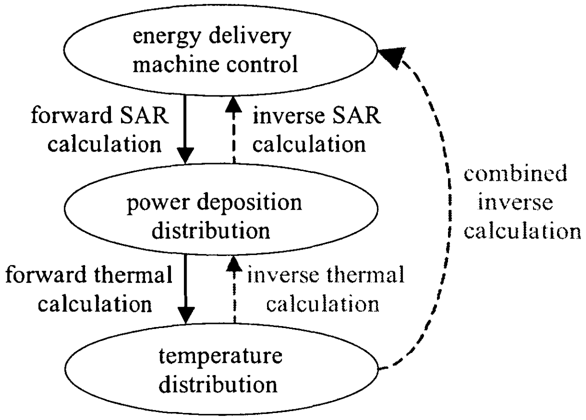

Figure 1-1 Overview of hyperthermia thermal management system

The basic form of the thermal management system can be shown in Figure 1-1. The system consists of two forward calculations and two inverse calculations. The forward calculation begins with the hyperthermia applicator excitation mode. This excitation mode creates a power deposition field and then a temperature deposition field in the target tissue. This process may be decoupled into two steps, since the temperature field has very small effects on tissue energy absorption. The inverse procedure starts from a given optimal temperature field. The inverse thermal calculation may be used to find the corresponding power deposition field and inverse SAR calculation to find the machine control mode. The integrated thermal management system is not yet available, though some components of the system have been developed. For example, MIT Hyperthermia Program has developed algorithms for fast forward temperature computation, which include hyperthermia thermal model using Finite Basis Element Method (Martin, 1995) and forward SAR model (Sidney, 1997) for ultrasound applicators. These components can provide simulated prediction prior to hyperthermia therapy and process evaluation after the therapy.

Other major components, such as inverse algorithm for optimal temperature distribution, transient algorithm for real-time temperature reconstruction, and control algorithm for temperature feedback control also play important roles in the thermal management system. The purpose of this thesis is to provide critical components for the thermal management system which, when included, can greatly improve the effectiveness and safety of the clinical hyperthermia therapy. The first major component is inverse algorithm for temperature field optimization. The inverse algorithm should be able to provide the therapist the optimal power pattern in the tumor tissue and the optimal control parameters of the energy delivery machines.

The second major component under development is the transient algorithm for real-time temperature reconstruction. The current model cannot provide real-time power field and temperature field information. The lack of real-time information limits the therapist ability to assess and make accurate adjustment during the therapy. The transient algorithm should be able to provide real-time temperature field reconstruction using whatever sparse measurement information available during the therapy. The ideal real-time application should be able to provide complete and accurate information on power field and temperature field; and to provide decision-making information for manual control or automatic feedback control of energy delivery machines.

These algorithms, like other existing components in the thermal management system, should be able to compromise the speed and accuracy of computation to provide fast solution for routine clinical treatment.

1.4 Thesis Organization and Contribution

This thesis is organized into five chapters. Chapter 2 presents the theoretical background in tissue heat transfer and the popular bioheat transfer equation commonly used in clinical hyperthermia. Two numerical methods, Finite Basis Element Method (FBEM) and Finite Element Method (FEM), are described and formulated in detail and their implementation methods are also included. These numerical models are used in the following chapters as the numerical tools to provide numerical simulation and comparison.

Chapter 3 is on inverse thermal analysis. First, a brief introduction to inverse thermal problems in general is given, and then the review of current progress in inverse thermal problems for clinical hyperthermia. The inverse thermal problems in hyperthermia are categorized and summarized. Second, the solutions of inverse thermal analysis for desired power field are presented analytically for one-dimensional tumor model and numerically for three-dimensional cubic tumor model. The inverse algorithms for FBEM and FEM have been formulated. The numerical results from FBEM and FEM are presented and compared, as well as their speed and accuracy. Third, the algorithm for combined inverse thermal analysis, which can link the optimal temperature field to the control parameters of the energy delivery machine, is derived. The concept of using normalized source to represent a concentrated source and placing normalized sources into source array is introduced. The numerical simulations of the combined thermal analysis are presented in three tumor models, i.e. the cubic tumor model, the spherical tumor model and the ellipsoidal tumor model. The effect of source placement and perfusion are also discussed.

Chapter 4 is on transient thermal analysis. The theoretical background of transient Finite Basis Element Method is introduced. The solution method based on Green's function and forward and inverse Laplace transform is derived. The formulation of various practical transient basis elements, for example, free-space element, bounded element and the elements for variable thermal properties and perfusion, is presented. The transient Finite Basis Element Method validation is performed by the comparisons to problems with exact analytical solutions. The effects of integration volume, element size and boundary vicinity are also discussed.

Chapter 5 contains conclusion and discussions the limitation and direction of future work in thermal management system development.

The Author's Contributions

The author's contributions are primarily in inverse and transient thermal analysis (Chapter 3 and Chapter 4). In functional format, the contributions may briefly categorized and itemized as:

1. Modeling and Algorithm Formulation
    - The inverse FBEM algorithms for desired temperature pattern
    - The inverse FEM algorithm for desired temperature pattern
    - The algorithm for combined inverse thermal analysis
    - The transient Finite Basis Element Method to solve transient bioheat transfer equation
2. Implementation and Programming
    - The implementation of inverse FBEM algorithm and inverse FEM algorithm.
    - The formulation of various practical transient Finite Basis Elements
3. Simulation and Validation
    - The simulation of inverse FBEM and inverse FEM for desired power field
    - The simulation with normalized source array for three simple geometry tumor models
    - The validation of transient Finite Basis Element Method.

Chapter 2

Quantitative Modeling

2.1 Tissue Thermal Models

Tissue thermal models describe the bioheat transfer mechanism in human tissue. Compared to solid heat conduction, tissue heat transfer is very complicated due to the fact that heat transfer is greatly influenced by blood flow and the irregular geometry of vasculature, which makes the application of heat transfer equations coupled with the Navier-Stokes flow equations and practically unsolvable. Chen and Holmes (Chen, 1980), Weinbaun and Jiji (Weinbaun, 1984) have developed tissue thermal models based on vascular heat transfer. Application of these models to regular vasculature, such as a whole limb (Song, 1988) and a pig renal cortex (Xu, 1991), has been achieved by further simplification from the original vascular models. Although great effort has been made to simplify these models for more application, they are still too complicated, coupled with too many assumed parameters, to use in clinical application.

A simplified assumption is that to treat the blood flow vector field as a scalar field called "perfusion". It is first developed by Pennes (1948), from the experiments of invasive temperature measurement of human forearm. This empirical model expresses the effects of blood flow into a single term in the heat transfer equation. The added term, called "perfusion", is proportional to the arterial temperature. If the arterial temperature is not too far away from tissue temperature, the bioheat transfer equation can be expressed as:

$$\frac{1}{\alpha_m}\frac{\partial T}{\partial t} = \nabla^2 T - \lambda^2 T + \frac{Q}{k_m} \tag{2.1}$$

$$\lambda = \sqrt{\frac{\omega \rho_b c_b}{k_m}} \tag{2.2}$$

where

T	temperature elevation above the arterial blood temperature (°C)
α_m	tissue thermal diffusivity (m^2/s)
ω	local perfusion rate (1/s)
ρ_b	blood density (kg/m^3)
k_m	tissue thermal conductivity (W/m°C)
c_b	blood specific heat (J/kg°C)
Q	absorbed power (W/m^3)
t	time (s)

There are many experimental and theoretical investigations, which prove the effect of the perfusion model in the tissue area where there is no thermally significant blood vessel (Roemer 1989) (Chato 1989), i.e. the diameter of the vessel is not large enough to significantly affect the tissue temperature.

For simplicity, it is better to write the bioheat transfer equation in dimensionless form.

$$\frac{\partial T}{\partial t^+} = \nabla^{+2} T - Pe \cdot T + q^+ \tag{2.3}$$

where the dimensionless parameters are defined as:

$$\begin{cases} r^+ = \dfrac{r}{a} \\ t^+ = \dfrac{\alpha_m}{a^2} t \\ Pe = \dfrac{\omega \rho_b c_b}{k_m} a^2 \\ q^+ = \dfrac{Q a^2}{k_m} \end{cases} \tag{2.4}$$

where a is the characterized length.

The bioheat transfer equation is an elliptical second-order partial differential equation. The temperature field can be solved if a well-defined boundary condition and initial condition are given. The boundary condition can be given in the general form as:

$$\alpha T + \beta \frac{\partial T}{\partial n} = \gamma \tag{2.5}$$

where α, β and γ are coefficients which can be given for certain boundary condition, $\boldsymbol{n}$ is the unit normal vector of the boundary surface.

2.2 Numerical Methods

The rapid development of computer technology in the last decades provides powerful tools for the development and adoption of numerical methods in many fields traditionally dominated by analytical and empirical methodology, such as heat transfer. Many numerical methods have been used to solve tissue heat transfer problem, including finite difference method (Spiegel, 1987; Moros, 1992), finite element method (Charny, 1989), etc. The use of commercially available finite element software package is also documented (Martin, 1995). Generally these methods require the formulation of a series of linear equations directly or implicitly. The solution of the linear equations is computationally intensive. The adoption of these numerical methods to real-time clinical application is still under developed.

In order to overcome the limitation of computing power for real-time application, Newman (1990) proposed a fast algorithm based on source superposition. The method, named Finite Basis Element Method, was implemented and validated for steady state temperature calculation by Martin (1995). Their results show that the temperature filed can be calculated within one minute with acceptable errors (RMS error is less than 0.3°C). As a comparison, the calculation of an equivalent temperature field with commercially available software package (NEKTON) requires 30 minutes (Newman, 1995).

The irregularity of the tissue geometry requires that the numerical method should work well in irregular domain. The FBEM takes into account the irregularities in tissue geometry, as well as the irregularities in tissue's properties. In the flowing sessions, both the theoretical background and implementation method are introduced for FBEM and FEM. The latter has become a quite standard numerical method to solve partial differential equations. Therefore it can provide numerical comparison and validation.

2.2.1 Finite Basis Element Method (FBEM)

Theoretical Background

The steady state Finite Basis Element Method (FBEM) has been developed (Martin, 1995) for the calculation of temperature field based on Green's function. The steady state tissue heat transfer equation can be written as:

$$\nabla^2 T - \lambda^2 T + \frac{Q}{k_m} = 0 \tag{2.6}$$

The Green's function solution for the equation is:

$$T(\mathbf{r}) = \int_V \frac{Q(\mathbf{r}_p)}{k_m} u(\mathbf{r},\mathbf{r}_p) dV - \int_S T_B(s)\mathbf{n}\cdot\nabla u ds \tag{2.7}$$

where u is the Green's function, $\boldsymbol{r}$ is the position vector and $\boldsymbol{r_p}$ is the position vector of a source center. In an infinite domain, the Green's function is:

$$u(r,r_p) = \frac{e^{-\lambda|r-r_p|}}{4\pi|r-r_p|} \tag{2.8}$$

The temperature consists of volume integration and boundary integration. Note that the Green's function attenuates exponentially over distance, the volume integration can be divided into two regions, i.e. the near field (V_{int}) and far field, such that the integration in the far field is negligibly small. The near field region can be called as thermally significant region while the far field region can be called as thermally less significant region.

$$T(\mathbf{r}) = \int_{V-V_{\text{int}}} \frac{Q(\mathbf{r}_p)}{k_m} u(\mathbf{r},\mathbf{r}_p) dV + \int_{V_{\text{int}}} \frac{Q(\mathbf{r}_p)}{k_m} u(\mathbf{r},\mathbf{r}_p) dV \tag{2.9}$$

$$V_{int} = \frac{4}{3}\pi(N_p L_p)^3,\ V_{int} < V \tag{2.10}$$

where L_p is perfusion length:

$$L_p = \sqrt{\frac{k_m}{\omega \rho_b c_b}} = \frac{1}{\lambda} \tag{2.11}$$

and N_p is the number of perfusion length which determines the radius of near field, hence determines the accuracy of the solution. The near field region, or the thermally significant region can be further divided into smaller volumes, which is called basis elements. The temperature at any given point is the superposition of all the elements. This process can be generalized as:

$$T(\mathbf{r}) = \Theta_0(\mathbf{r}, \mathbf{r}_0) + P_f \sum_{j=1}^{N} \Theta_j(\mathbf{r}, \mathbf{r}_j) \tag{2.12}$$

where

Θ_0	macroscopic Finite Basis Element
Θ_j	Finite Basis Element (FBE)
P_f	packing factor

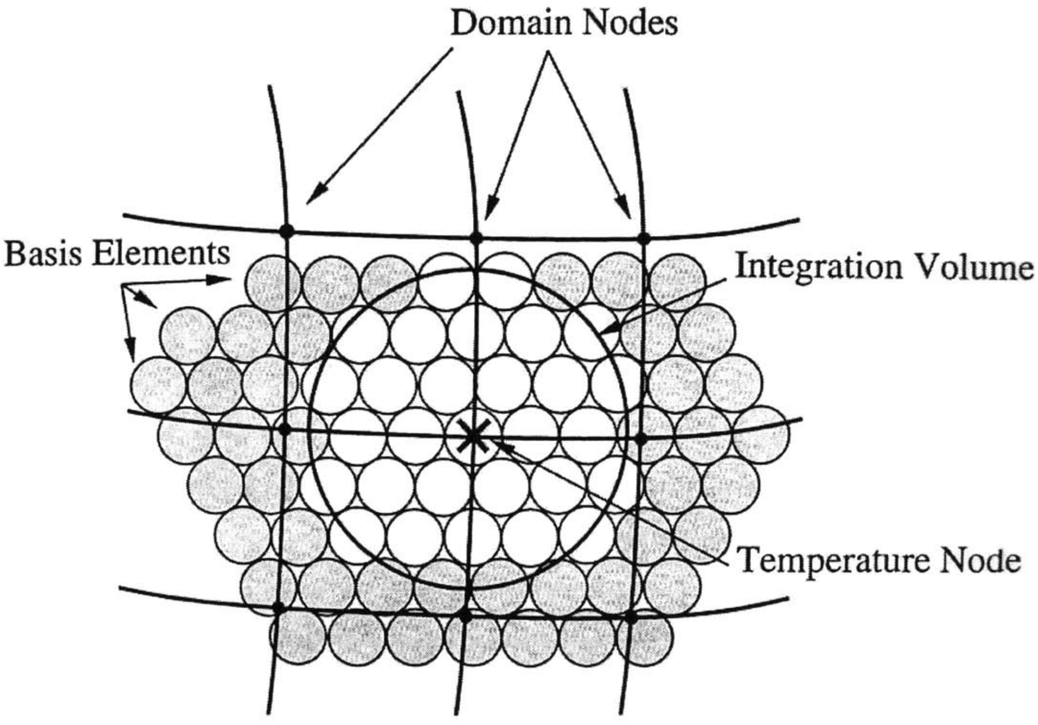

Picture courtesy of Dr. Gregory Martin

Figure 2-1 Close hexagonal packing of the Basis Elements in the domain

Figure 2-1 shows a diagram of the close hexagonal packing for the Basis Elements. The grid points are the domain nodes on which the temperature will be calculated. For example, if temperature at the cross point is to be calculated, the Basis Elements center exactly at that point. The unshaded elements are within thermally significant region. The contribution of these sources on the temperature is summed. The shaded elements are in the thermally less significant region. The contribution of these sources on the temperature is either ignored or lumped together to form a microscopic Basis Elements, depending on the accuracy requirements.

The temperature depends on power deposition, i.e. the equation can be expressed as a function of descretized power:

$$T_i = \sum_{j=1}^{M} Q_j K_{ij} \tag{2.13}$$

in matrix form:

$$\begin{bmatrix} T_1 \\ T_2 \\ \vdots \\ T_N \end{bmatrix} = \begin{bmatrix} K_{11} & K_{12} & \cdots & K_{1M} \\ K_{21} & K_{22} & \cdots & K_{2M} \\ \cdots & \cdots & \cdots & \cdots \\ K_{N1} & K_{M2} & \cdots & K_{NM} \end{bmatrix} \begin{bmatrix} Q_1 \\ Q_2 \\ \vdots \\ Q_M \end{bmatrix} \tag{2.14}$$

or

$$\mathbf{T} = \mathbf{KQ} \tag{2.15}$$

The major advantage of FBEM over other numerical methods, such as FEM and finite difference method, is that temperature at any point can be calculated directly by the superposition of basis elements, without knowledge of neighboring temperature. That's the underlined reason that FBEM is faster than FEM by an order of magnitude.

Implementation

For mathematical and computational simplicity, the source in the domain is represented by finite spherical sources. Note that the spherical elements cannot cover all the volume in the domain. The packing factor P_f is introduced to distribute the effect of the source in the uncovered volume uniformly to nearby elements. This limits the accuracy level that can be achieved by Finite Basis Element Methods. Therefore, it would be wise to choose the densest possible packing. The close hexagonal packing is one of the densest possible packing methods of equal spheres. It's packing density is $\pi/(3\sqrt{2})$ or 0.74. In close hexagonal packing, layers of spheres are packed so that spheres in alternating layers overlie one another. Figure 2-2 is a two dimensional diagram of the Basis Elements in close hexagonal packing. The shaded elements are on the base layer. Each of the elements on the upper layer (represented by blue circles) lies on the top of three base layers elements. So there are 12 neighboring elements for each of the elements. Elements in the third layer (represented by red circles) repeat the layout scheme of the base layer elements. Figure 2-3 is a three dimensional diagram of the Basis Elements in close hexagonal packing.

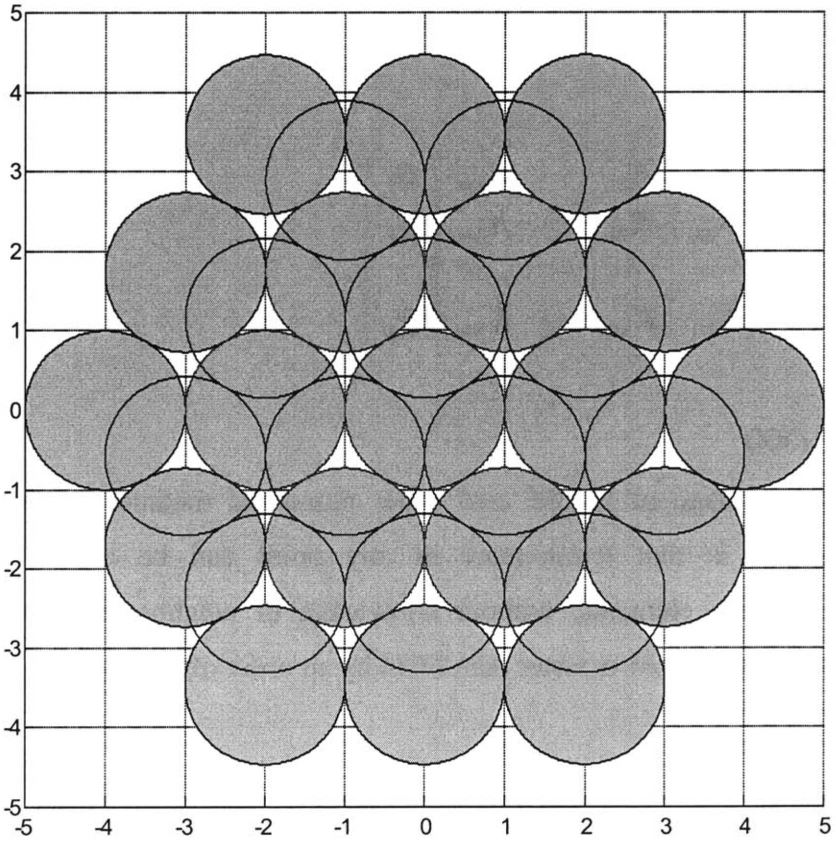

Figure 2-2 Two-dimensional diagram of the Basis Elements in close hexagonal packing

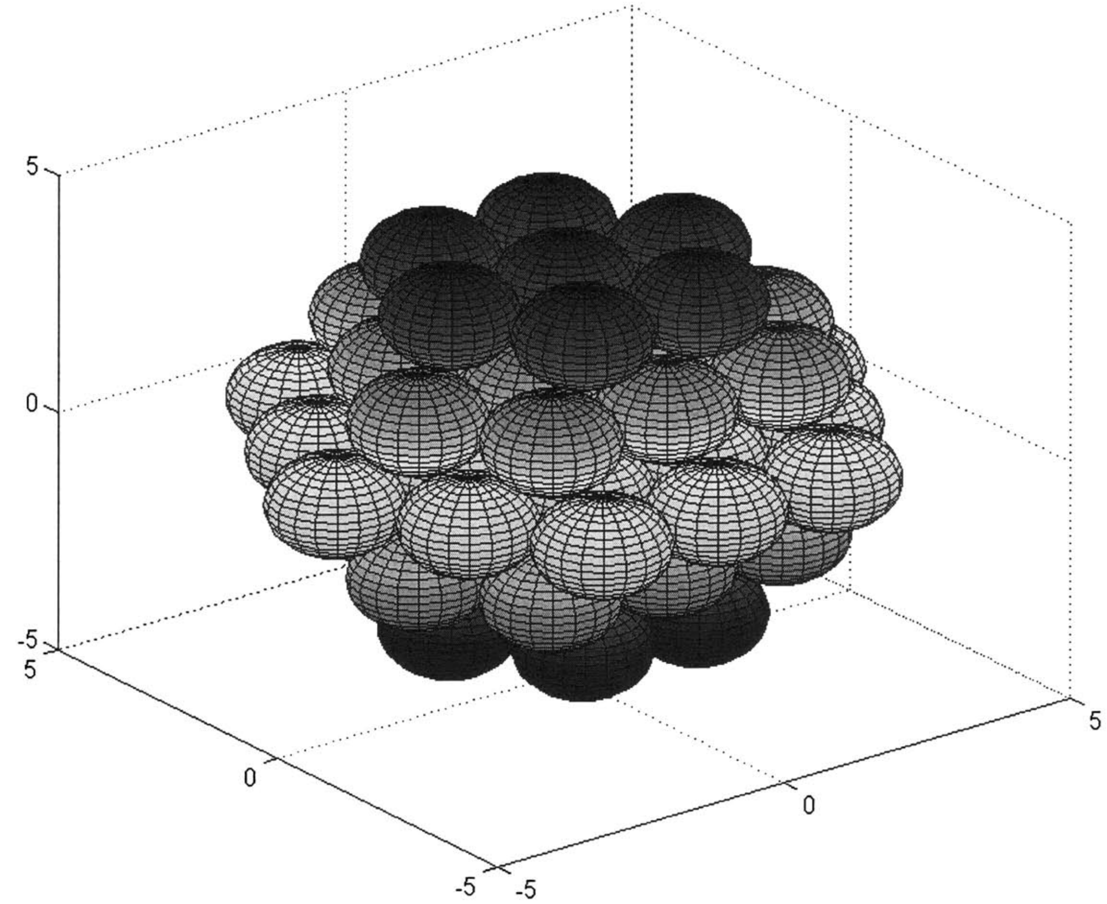

Figure 2-3 Three-dimensional diagram of the Basis Elements in close hexagonal packing

2.2.2 Finite Element Method (FEM)

Principle of virtual temperature

For any arbitrary virtual temperature field $\overline{T}$, which satisfies the same boundary condition in equation (2.5), we may multiply the virtual temperature $\overline{T}$ to equation (2.6) and integrate over the whole domain.

$$\int_V \overline{T}(\nabla^2 T - \lambda^2 T + \frac{Q}{k_m})dV = 0 \tag{2.16}$$

note that:

$$\overline{T}\nabla^2 T = \nabla\cdot(\overline{T}\nabla T) - (\nabla\overline{T})\cdot(\nabla T) \tag{2.17}$$

and defining:

$$q^B = \frac{Q}{k_m} \tag{2.18}$$

the volume integration of the first term on the right handed side can be transformed to a corresponding surface integration. The partial differential equation can be rewritten into an integral form as

$$\int_V [(\nabla T)\cdot(\nabla\overline{T}) + \lambda^2\overline{T}T]dV = \int_V \overline{T}q^B dV + \int_S \overline{T}^s \frac{\partial T}{\partial n} dS \tag{2.19}$$

This equation can also be called as the principle of virtual temperature. In matrix form, the equation is:

$$\int_V (\overline{\boldsymbol{T}}'^T \boldsymbol{T}' + \overline{T}\lambda^2 T)dV = \int_V \overline{T}q^B dV + \int_{S_q} \overline{T}^s q^s dS \tag{2.20}$$

where

$$\boldsymbol{T}'^T = \begin{bmatrix} \frac{\partial T}{\partial x} & \frac{\partial T}{\partial y} & \frac{\partial T}{\partial z} \end{bmatrix} \tag{2.21}$$

The principle of virtual temperature shows the heat transfer equilibrium: if *T* is the solution of the temperature in the domain under consideration, equation (2.20) must hold for any arbitrary virtual continuous temperature distribution that holds the same boundary conditions as *T* on the boundary of the domain.

Finite Element Equation

The whole domain under consideration can be discretized into a series of numbered elements, which is composed by a series of numbered nodes. Suppose the element is numbered by *m*, the total number of elements is *M*, and the total number of nodes is *N*. The principle of virtual temperature can be rewritten into the discretized form:

$$\begin{aligned} &\sum_m \int_{V^{(m)}} [(\overline{\boldsymbol{T}}'^{(m)})^T \boldsymbol{T}'^{(m)} + \lambda^2 \overline{T}^{(m)} T^{(m)}] dV^{(m)} \\ &= \sum_m \int_{V^{(m)}} \overline{T}^{(m)} q^{B(m)} dV^{(m)} + \sum_m \int_{S_1^{(m)},\dots,S_q^{(m)}} \overline{T}^{s(m)} q^{s(m)} dS^{(m)} \end{aligned} \tag{2.22}$$

The temperature of any point inside element *m* is given by:

$$T^{(m)}(x,y,z) = \boldsymbol{H}^{(m)}(x,y,z)\hat{\boldsymbol{T}} \qquad (2.23)$$

$\boldsymbol{H}^{(m)}$ is called temperature interpolation matrix (*1* by *N*). $\boldsymbol{T}$ is nodal temperature arranged in matrix form (*N* by *1*). The temperature gradient can be interpolated as:

$$\boldsymbol{T}'^{(m)}(x,y,z) = \boldsymbol{B}^{(m)}(x,y,z)\hat{\boldsymbol{T}} \qquad (2.24)$$

Where $\boldsymbol{B}$ matrix (*3* by *N*) can be obtained by differentiating $\boldsymbol{H}$ matrix with respect to the three coordinates *(x,y,z),* respectively.

$$\boldsymbol{B}^{(m)}(x,y,z) = \nabla \boldsymbol{H}^{(m)}(x,y,z) \qquad (2.25)$$

The power deposition interpolation matrix is the same as the temperature interpolation matrix:

$$q^{B(m)}(x,y,z) = \boldsymbol{H}^{(m)}(x,y,z)\hat{\boldsymbol{q}}^{B} \qquad (2.26)$$

The interpolation matrix for boundary temperature is:

$$T^{s(m)}(x,y,z) = \boldsymbol{H}^{s(m)}(x,y,z)\hat{\boldsymbol{T}} \qquad (2.27)$$

Substituting all the interpolation matrices into equation (2.22), we have:

$$\begin{aligned}
&\bar{\hat{\boldsymbol{T}}}^{T}\left\{\sum_{m}\int_{V^{(m)}}[\boldsymbol{B}^{(m)T}\boldsymbol{B}^{(m)}\hat{\boldsymbol{T}} + \lambda^{2}\boldsymbol{H}^{(m)T}\boldsymbol{H}^{(m)}\hat{\boldsymbol{T}}]dV^{(m)}\right\} \\
&= \bar{\hat{\boldsymbol{T}}}^{T}\left\{\sum_{m}\int_{V^{(m)}}\boldsymbol{H}^{(m)T}\boldsymbol{H}^{(m)}\hat{\boldsymbol{q}}^{B}dV^{(m)} + \sum_{m}\int_{S_1^{(m)},\dots,S_q^{(m)}}\boldsymbol{H}^{s(m)T}q^{s(m)}dS^{(m)}\right\}
\end{aligned} \qquad (2.28)$$

Since the virtual temperature is arbitrary, it can be eliminated from equation (2.28). Then the equation can be written as:

$$\begin{aligned}
&\left\{\sum_{m}\int_{V^{(m)}}[\boldsymbol{B}^{(m)T}\boldsymbol{B}^{(m)} + \lambda^{2}\boldsymbol{H}^{(m)T}\boldsymbol{H}^{(m)}]dV^{(m)}\right\}\hat{\boldsymbol{T}} \\
&= \left\{\sum_{m}\int_{V^{(m)}}\boldsymbol{H}^{(m)T}\boldsymbol{H}^{(m)}dV^{(m)}\right\}\hat{\boldsymbol{q}}^{B} + \sum_{m}\int_{S_1^{(m)},\dots,S_q^{(m)}}\boldsymbol{H}^{s(m)T}q^{s(m)}dS^{(m)}
\end{aligned} \qquad (2.29)$$

defining:

$$\boldsymbol{K}_{T} = \sum_{m}\int_{V^{(m)}}[\boldsymbol{B}^{(m)T}\boldsymbol{B}^{(m)} + \lambda^{2}\boldsymbol{H}^{(m)T}\boldsymbol{H}^{(m)}]dV^{(m)} \qquad (2.30)$$

$$\boldsymbol{K}_{q} = \sum_{m}\int_{V^{(m)}}\boldsymbol{H}^{(m)T}\boldsymbol{H}^{(m)}dV^{(m)} \qquad (2.31)$$

$$\boldsymbol{R}_{s} = \sum_{m}\int_{S_1^{(m)},\dots,S_q^{(m)}}\boldsymbol{H}^{s(m)T}q^{s(m)}dS^{(m)} \qquad (2.32)$$

finally, the finite element equation is:

$$\boldsymbol{K}_T\hat{\boldsymbol{T}} = \boldsymbol{K}_q\hat{\boldsymbol{q}}^B + \boldsymbol{R}_s \tag{2.33}$$

Equation (2.33) is a general bioheat transfer finite element equation, which can be used to perform forward thermal calculation, as well as inverse thermal calculation. If the power deposition pattern and the boundary condition are given, the temperature distribution can be calculated from equation (2.33). This is the forward thermal calculation in hyperthermia. If the temperature field and the boundary condition are given, equation (2.33) can also calculate the power deposition field. This is inverse thermal calculation in hyperthermia.

Formulation of Isoparametric Elements

The basic procedure in the isoparametric finite element formulation is to express the element coordinates and element parameters in standard local coordinate system of the element. Considering a general 3-D element, if the global coordinate system is *(x,y,z)* and the local coordinate system is *(r,s,t)*, the coordinate at any point of the element can be interpolated as:

$$x = \sum_{i=1}^{q} h_i x_i; \qquad y = \sum_{i=1}^{q} h_i y_i; \qquad z = \sum_{i=1}^{q} h_i z_i \tag{2.34}$$

where x,y,z are the coordinates at any point inside the element and x_i, y_i, z_i, $(i=1,\dots,q)$ are the coordinates of the q element nodes. h_i $(i=1,\dots,q)$ are the interpolation functions of the local coordinates of any element, which has coordinates (r,s,t) that each varies from -1 to 1. The fundamental property of the interpolation functions is that its value in the local coordinate system is unity at node *i* and zero at all other nodes. The interpolation functions are generally expressed in the form of polynomials of different orders according to the element.

In the isoparametric formulation, the temperatures are interpolated in the same ways as the geometry:

$$T = \sum_{i=1}^{q} h_i T_i \tag{2.35}$$

All the integration may be calculated in local coordinate system. The derivative term may be calculated in local coordinate system by the chain rule:

$$\frac{\partial}{\partial x} = \frac{\partial}{\partial r}\frac{\partial r}{\partial x} + \frac{\partial}{\partial s}\frac{\partial s}{\partial x} + \frac{\partial}{\partial t}\frac{\partial t}{\partial x} \tag{2.36}$$

since the interpolation matrix can not give us an explicit form of $r=r(x,y,z),\ldots\ldots$, but only the implicit form of $x=x(r,s,t),\ldots\ldots$, an inverse relation is needed to be evaluated.

$$\begin{bmatrix} \dfrac{\partial}{\partial r} \\ \dfrac{\partial}{\partial s} \\ \dfrac{\partial}{\partial t} \end{bmatrix} = \begin{bmatrix} \dfrac{\partial x}{\partial r} & \dfrac{\partial y}{\partial r} & \dfrac{\partial z}{\partial r} \\ \dfrac{\partial x}{\partial s} & \dfrac{\partial y}{\partial s} & \dfrac{\partial z}{\partial s} \\ \dfrac{\partial x}{\partial t} & \dfrac{\partial y}{\partial t} & \dfrac{\partial z}{\partial t} \end{bmatrix} \begin{bmatrix} \dfrac{\partial}{\partial x} \\ \dfrac{\partial}{\partial y} \\ \dfrac{\partial}{\partial z} \end{bmatrix} \tag{2.37}$$

or the matrix notation:

$$\frac{\partial}{\partial \boldsymbol{r}} = \boldsymbol{J}\frac{\partial}{\partial \boldsymbol{x}} \tag{2.38}$$

where $\boldsymbol{J}$ is the Jacobi's matrix. If the inverse of $\boldsymbol{J}$ exists, we have:

$$\frac{\partial}{\partial \boldsymbol{x}} = \boldsymbol{J}^{-1}\frac{\partial}{\partial \boldsymbol{r}} \tag{2.39}$$

The volume integration in (x,y,z) may be changed to (r,s,t) in the following way.

$$dV = dxdydz = \det \boldsymbol{J} drdsdt \tag{2.40}$$

The calculation of elemental mass matrix and stiffness matrix in local coordinates system is:

$$\boldsymbol{M} = \int_{-1}^{1}\int_{-1}^{1}\int_{-1}^{1} \boldsymbol{H}^T(r,s,t)\rho \boldsymbol{H}(r,s,t)\det \boldsymbol{J} drdsdt \tag{2.41}$$

$$\boldsymbol{K} = \int_{-1}^{1}\int_{-1}^{1}\int_{-1}^{1} \boldsymbol{B}^T(r,s,t)\rho \boldsymbol{B}(r,s,t)\det \boldsymbol{J} drdsdt \tag{2.42}$$

These integrations can be calculated analytically for low order polynomials or numerically for high order polynomials.

Formulation of Two-Dimensional Triangular Elements

The simplest element in two-dimensional geometry is a triangular element with three nodes, one at each corner, as shown in Figure 2-4. The elemental matrices can be formed directly in its original coordinate system, or in the local coordinate system.

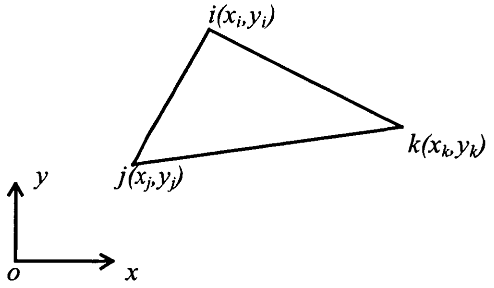

Figure 2-4 Diagram of two-dimensional triangular element for Finite Element Method

The interpolation polynomial is linear for triangular element.

$$L_i(x,y) = a_i + b_i x + c_i y \tag{2.43}$$

The coefficients (a_i, b_i, c_i) can be solved, if the coordinates of the three nodes are given, by the fundamentally properties of interpolation functions (unity at node i and zero at others). The results are:

$$a_i = \frac{x_j y_k - x_k y_j}{2A} \tag{2.44}$$

$$b_i = \frac{y_j - y_k}{2A} \tag{2.45}$$

$$c_i = -\frac{x_j - x_k}{2A} \tag{2.46}$$

where A is the area of the triangle:

$$A = \frac{1}{2}\begin{vmatrix} 1 & x_i & y_i \\ 1 & x_j & y_j \\ 1 & x_k & y_k \end{vmatrix} \tag{2.47}$$

The above interpolation expressed in global coordinates and can be evaluated directly without the help of local coordinate system. Also we can construct a local coordinate system based on the above relations, which is called area coordinate system. The relation between global coordinates and local coordinates is:

$$\begin{bmatrix} L_1 \\ L_2 \\ L_3 \end{bmatrix} = \begin{vmatrix} a_1 & b_1 & c_1 \\ a_2 & b_2 & c_2 \\ a_3 & b_3 & c_3 \end{vmatrix} \begin{bmatrix} 1 \\ x \\ y \end{bmatrix} \tag{2.48}$$

The integration in the local coordinates is guided by the formula:

$$\iint_A L_1^{\alpha} L_2^{\beta} L_3^{\gamma} dA = \frac{\alpha!\beta!\gamma!}{(\alpha+\beta+\gamma+2)!} 2A \tag{2.49}$$

Formulation of Three-Dimensional Tetrahedral Elements

The simplest element in three-dimensional geometry is a tetrahedral element with four nodes, one at each corner, as shown in Figure 2-5.

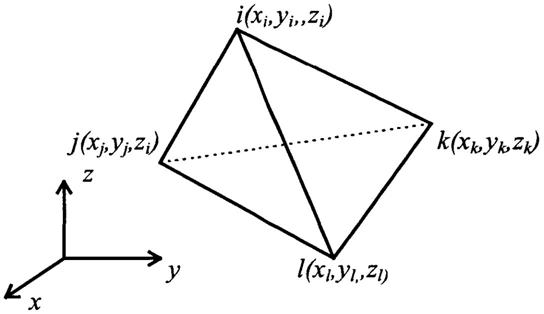

Figure 2-5 Diagram of three-dimensional tetrahedral element for Finite Element Method

The interpolation polynomial is linear for tetrahedral element:

$$L_i(x, y) = a_i + b_i x + c_i y + d_i z \tag{2.50}$$

the coefficients (a_i, b_i, c_i, d_i) can be solved, if the coordinates of the four nodes are given, by the fundamental properties of interpolation functions (unity at node i and zero at others). The results are:

$$a_i = \frac{1}{6V} \begin{vmatrix} x_j & y_j & z_j \\ x_k & y_k & z_k \\ x_l & y_l & z_l \end{vmatrix} \tag{2.51}$$

$$b_i = -\frac{1}{6V} \begin{vmatrix} 1 & y_j & z_j \\ 1 & y_k & z_k \\ 1 & y_l & z_l \end{vmatrix} \tag{2.52}$$

$$c_i = -\frac{1}{6V}\begin{vmatrix} x_j & 1 & z_j \\ x_k & 1 & z_k \\ x_l & 1 & z_l \end{vmatrix} \tag{2.53}$$

$$d_i = -\frac{1}{6V}\begin{vmatrix} x_j & y_j & 1 \\ x_k & y_k & 1 \\ x_l & y_l & 1 \end{vmatrix} \tag{2.54}$$

where V is the volume of the tetrahedral:

$$V = \frac{1}{6}\begin{vmatrix} 1 & x_i & y_i & z_i \\ 1 & x_j & y_j & z_j \\ 1 & x_k & y_k & z_k \\ 1 & x_l & y_l & z_l \end{vmatrix} \tag{2.55}$$

The above interpolation expressed in global coordinates and can be evaluated directly without the help of the local coordinate system. Also we can construct a local coordinate system based on the above relations, which is called volume coordinate system. The relation between global coordinates and local coordinates is:

$$\begin{bmatrix} L_1 \\ L_2 \\ L_3 \\ L_4 \end{bmatrix} = \begin{vmatrix} a_1 & b_1 & c_1 & d_1 \\ a_2 & b_2 & c_2 & d_2 \\ a_3 & b_3 & c_3 & d_3 \\ a_4 & b_4 & c_4 & d_4 \end{vmatrix}\begin{bmatrix} 1 \\ x \\ y \\ z \end{bmatrix} \tag{2.56}$$

The integration in the local coordinates is guided by the formula:

$$\iiint_V L_1^{\alpha} L_2^{\beta} L_3^{\gamma} L_4^{\delta} dV = \frac{\alpha!\beta!\gamma!\delta!}{(\alpha+\beta+\gamma+\delta+3)!}6V \tag{2.57}$$

Implementation

Three-dimensional tumor models are used in numerical simulation. The domain is divided into small tetrahedral elements and the mesh is generated. Sparse matrix form is used in matrix formulation in order to minimize the requirement for large computer memory. An iterative sparse matrix solver (SPLIB) is used to solve the linear equations. All the source codes are written in FORTRAN language.

Chapter 3

Inverse Thermal Analysis

3.1 Introduction to Inverse Thermal Problem

Inverse problem can be defined as finding the cause from a known result. Inverse problems are mathematically challenging and practically important. Inverse problems can be found in many fields from pure science to engineering application. As a matter of fact, those problems that involve data interpretation and design optimization are "inverse" in nature.

The space program drew much attention to inverse heat transfer problems in the 50's and 60's, during which significant progress in solution methods has been developed. For example, it is practically impossible to measure the surface temperature of a space vehicle directly by placing temperature sensors on the surface of the shield during its reentry of atmosphere. Therefore temperature sensors were placed beneath the hot surface of the shield. The surface temperature was estimated from the measured data by inverse analysis.

As a comparison, most of the standard thermal problems can be categorized as direct thermal problems. The approaches to solve these kinds of problems have progressed for almost two centuries. The mathematical models governing the physics have been developed as a series of heat transfer equations in differential or integral form. The coefficients of the equations, such as physical properties (density, velocity, etc.) and thermal properties (conductivity, specific heat, etc.) must be specified. In order to solve the equations, the geometry of the body, the boundary condition and initial condition must be known. These thermal problems are *well-posed* mathematically, which means that the following three conditions must be satisfied:

1) The solution must exist;
2) The solution must be unique;
3) The solution must be stable under small fluctuation to the input data.

On the contrary, inverse thermal problems are *Ill-posed.* There might be no solution, or multiple solutions, or unstable solution, or the above combined. An *Ill-posed* problem cannot be solved directly. A successful solution of an inverse thermal problem generally involves its reformation as an approximate well-posed problem. Therefore, most of the solutions are not "exact" solutions, but rather "least squares optimized" solutions. Tikhonov (1977) proposed a regularization procedure, which modifies the least squares equation by adding smoothing terms in order to reduce the unstable effects of the measurement errors. Others popular solutions include Alifanov's iterative regularization techniques (Alifanov, 1977, 1994) and Beck's function estimation approach (Beck, 1962, 1985).

In general, many of the inverse thermal problems fall into the three groups (Kurpisz, 1995) of *Inverse Boundary Problems*, *Parameter Estimation* and *Inverse Initial Problems.* The inverse boundary problems involve the estimation of the surface heat flux history of a body from transient temperature measurement in the interior locations. After the heat flux, or the boundary condition, is determined, it is easy to calculate the temperature field within the whole body. The parameter estimation is used to estimate one or more thermal properties of a body. Typical parameters to be estimated are: thermal conductivity, density, specific heat, thermal diffusivity and other properties that are difficult to measure. For clinical hyperthermia, it is very difficult to have a dense measurement of blood perfusion data within the tumor region and the neighboring normal tissue region. It is desirable to estimate the perfusion data wherever the direct measured data are not available. The inverse initial problems involve the determination of the initial condition from the temperature measurement inside a body at a later time.

3.2 Inverse Thermal Problem for Hyperthermia

The inverse problems in hyperthermia are much less investigated. From a few investigations shown in literature, the inverse thermal problems for hyperthermia can be categorized as

1) Estimate the thermal properties, such as blood perfusion, from limited temperature measurement. (Clegg 1985, 1989; Newman et al 1990)
2) Determine the power patterns from optimal temperature fields. (Ocheltree and Frizzell 1987)
3) Determine the instrument control of power delivery machines from optimal temperature fields. (McGough 1992, Nikita 1993)

The first category is a standard parameter estimation problem in inverse thermal analysis. The blood perfusion, even if it can be measured directly, is limited to a number of specified nodes due to the safety requirement. So it is highly desirable to determine the whole perfusion field within a body. Clegg (1985, 1989) developed methods to estimate the spatial fields of blood perfusion and the corresponding temperature fields from limited number of direct temperature measurements made during hyperthermia therapy. These methods estimate the perfusion field first, and then the data can be used to solve the temperature field. The estimated temperature fields were compared with the measured temperature. Iteration was needed until the estimated and measured temperature agreed with each other in least squared sense. These methods are extremely computational intensive, which in turn, limits their application to real time hyperthermia treatment.

In clinical hyperthermia, although there is no consensus on what is an optimal thermal dose, the assumption of the existence of an optimal thermal dose is still valid from physics intuition. The purpose of hyperthermia therapy is to delivery optimal thermal doses to target tumor region. The technical difficulty is how to delivery those doses. If an optimal temperature distribution for hyperthermia therapy is given, the technical question will be how to produce and maintain this kind of temperature distribution. With this inverse thinking, Ocheltree and Frizzell (1987) developed steady state analytical models for simple geometry and numerical model based on finite difference method for 3-D application. The purpose of their study is to determine an approach which will allow direct calculation of the initial treatment configuration based on the desired temperature profile, tissue properties including blood perfusion, and hyperthermia system parameters such as beam size for a scanned ultrasound applicator.

McGough (1992) developed a direct computation method, which obtains ultrasound hyperthermia applicator phased-array element driving signals from a desired temperature distribution. His approach combines a technique, which computes arrays element driving signals from focal point locations and intensities, with a new technique, which calculates focal point locations and power deposition values from temperature requirements.

Nikita (1993) described a method for the evaluation of optimal amplitude and phase excitations for the radiating elements of a phased array hyperthermia system, in order to achieve desired steady state temperature distribution inside and outside of malignant tissues. Optimal excitations are obtained by minimizing the squared error between desired and estimated temperatures inside the tumor volume, subject to the constraint that temperatures do not exceed an upper limit. She used an iterative optimization procedure to determine unknown power deposition by evaluating Jacobian Matrix, which is very complicated and time consuming in computation.

There are two steps in the inverse procedure, the first one is from a given temperature field, we need to find out the corresponding power field. The second step is from the optimal power field, to find out the control mode of the energy delivery machine. These two steps can be combined if we want to correlate the machine control mode directly to temperature field. Clinically it is desirable to relate the temperature field directly to the control parameters of power delivery instruments. This kind of problem is generally regarded as optimization with constraint, where the safety restriction should be strictly followed.

In the rest of the chapter, the second and third types of inverse thermal problems will be investigated; the algorithms for rapid computation will be formed and demonstrated in simulation for various simple geometry tumor models.

3.3 Inverse Thermal Analysis: Desired Power Field

In the last two decades, numerous energy delivery systems has been developed and used in clinical hyperthermia. Most of the latest systems allow more precise control of the power deposition pattern. Therefore it is desirable to determine the desired power deposition patterns from an optimal temperature distribution.

Based on the knowledge that the effectiveness and safety of hyperthermia depends on the preferential heating of tumor tissue to a therapeutic temperature, with minimal temperature elevation in the surrounding normal tissue, we assume that the desired hyperthermia therapy should keep the tumor tissue temperature to a therapeutic level and deliver zero power to normal tissue.

3.3.1 Analytical Solutions

Analytical solution can be derived for some simple geometry models, for example, half-space tumor and spherical tumor model. The analytical solutions can provide insight information for the power patterns in the normal tissue region, tumor region and the boundary between the two regions. Analytical solution can also be used to compare with the results from numerical simulation.

Half-Space Tumor Model

Let's first consider a one dimensional tumor model in Cartesian Coordinates, or half-space tumor model. The tumor region is at x<0 while the normal tissue is at x>0. The property of the tissue is uniform. The governing equation for the one-dimensional problem is:

$$\frac{d^2T}{dx^2} - \lambda^2 T + q^B = 0 \tag{3.1}$$

In the tumor tissue region, the temperature is uniformly distributed as T_0, i.e. the temperature gradient is zero. Therefore the power deposition in the tumor region is:

$$q^B = \lambda^2 T_0 \tag{3.2}$$

In the normal tissue, there is no power deposition, so $q^B=0$. The equation can be simplified as:

$$\frac{d^2T}{dx^2} - \lambda^2 T = 0 \tag{3.3}$$

The boundary condition for the normal tissue region is at $x=0$, $T=T_0$, at $x=\infty$, $T=0$. The solution of the equation for $x\geq 0$ is:

$$T = T_0 e^{-\lambda x} \tag{3.4}$$

The heat flux at $x=0$ is:

$$q_0 = -k_m \frac{dT}{dx}\bigg|_{x=0} = k_m \lambda T_0 \tag{3.5}$$

The temperature gradient is not continuos at *x=0*. According to energy conservation, the power deposition at the boundary is equal to the heat flux at *x=0*, and is given in equation (3.5).

Figure 3-1 shows the temperature distribution and power deposition field in a one-dimensional half-space tumor model. There is no power in the normal tissue. The power on the boundary between the normal tissue and tumor is a boundary delta function. The power deposition inside the tumor region is used to compensate the blood perfusion effect.

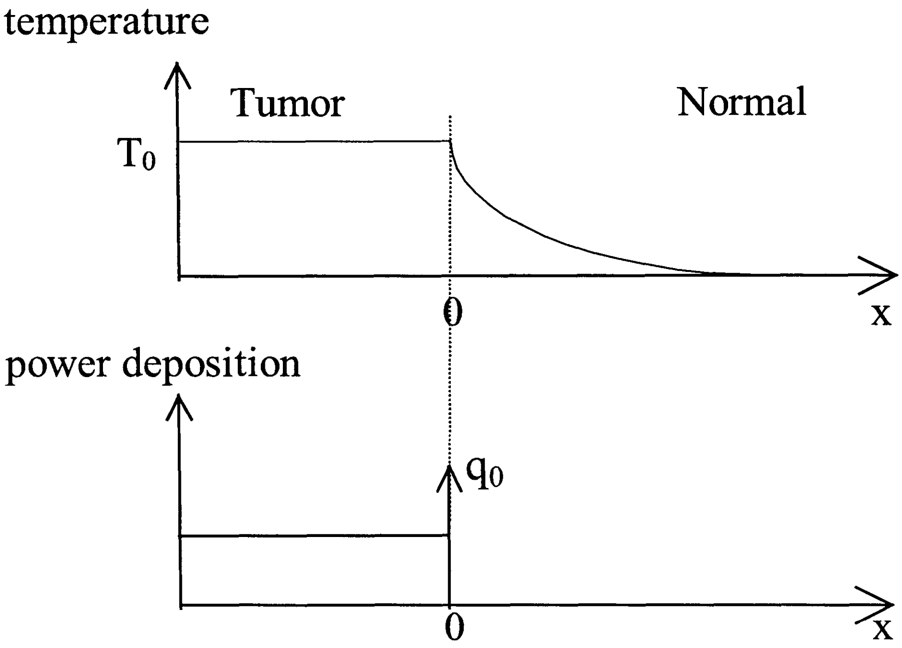

Figure 3-1 Temperature distribution and power depositions field in a one-dimensional half-space tumor model

Spherical Tumor Model

If the tumor's surface is not flat but curved, a spherical tumor model can be used as a simplified model. The spherical tumor has a radius of r_0. The governing equation is:

$$\frac{1}{r}\frac{d^2}{dr^2}(rT) - \lambda^2 T + q^B = 0 \tag{3.6}$$

Within the tumor region, the temperature is constant at T_0. Therefore the power deposition in the tumor region is:

$$q^B = \lambda^2 T_0 \tag{3.7}$$

In the normal tissue region, $q^B=0$. The boundary condition is at $r=r_0$, $T=T_0$. The temperature profile for the normal tissue region ($r>r_0$) is:

$$T = \frac{r_0 T_0}{r} e^{-\lambda(r-r_0)} \tag{3.8}$$

The boundary heat flux at $r=r_0$ is:

$$q_{r_0} = -k_m \frac{dT}{dr}\bigg|_{r=r_0} = (\frac{1}{r_0} + \lambda) k_m T_0 \tag{3.9}$$

The temperature profile for the spherical model is similar to that of the plate model except that due to the effect of curvature, the temperature in the normal tissue region decays faster in the spherical model than in the plate model and the boundary heat flux is greater in the spherical model than in the plate model.

The analytical results show some important factors that must be considered for power delivery machine design. The power deposition inside the tumor tissue is volumetric distributed source, which is used to compensate the heat loss by blood perfusion. It is also required to deposit power on the boundary between normal and tumor tissue. This source is a concentrated surface source (infinite large source on infinite small area, a boundary delta function). The existence of boundary delta function makes the problem a little bit tricky. In clinical practice, it's really difficult to produce power deposition in a delta function. The problem also arises in numerical calculation where a singular source is very difficult to handle and the results in the vicinity of the singular source are outrageous.

3.3.2 Numerical Solutions

Although the simplified analytical models show many general properties of the temperature and power deposition field, in clinical practice, it would be much more accurate if the tumor geometrical and physiological data can be used in the modeling and calculation. Therefore, numerical methods for more realistic three-dimensional models and non-uniform properties are needed.

The numerical methods used here are Finite Element Method (FEM) and Finite Basis Element Method (FBEM), which have been introduced in Chapter 2. FBEM proved to be cost-effective fast in forward temperature field calculation, compared to FEM (Martin, 1995). We explore the use of FBEM in inverse calculation of the entire temperature field and compare the results with those from standard FEM.

Finite Element Method

For three-dimensional problem, the number of nodes increases dramatically. If N is the number of nodes in one direction, the number of nodes in the three-dimensional domain is generally the order of N^3. In two-dimensional problem, the stiffness matrix can be stored in banded form. The number of elements in the matrix is to the order of the number of nodes times the bandwidth of the matrix, i.e. $N^2N=N^3$. In three-dimensional case, if the stiffness matrix were stored in banded form, the number of elements in the matrix would be to the order of $N^3N^2=N^5$. Since most of the elements in the banded matrix are zero, this storage is very ineffective. In practically, the three-dimensional stiffness matrix is stored in sparse matrix form, which stores only the non-zero elements of the matrix. If the average connectivity of the matrix is n, the number of elements in the sparse matrix is to the order of $N^3n=nN^3$. n is a number depends on the method of forming stiffness matrix, and is generally to the order of m^3, if m is the connectivity in one direction. For example, if the matrix is formed by first order finite difference method, the connectivity is about 9; if the matrix is formed by linear tetrahedral elements, the connectivity is 27.

Since the number of elements in the stiffness matrix is generally so large that direct solution, such as Gauss elimination is less efficient than an iterative method.

The domain for inverse FEM can be sketched in figure 3-2. The region can be divided into two parts, one is tumor tissue region and the other is normal tissue region. The tumor tissue region is enclosed by the normal tissue region. In the tumor tissue region, the optimal temperature is given, the power field is what we want and the internal boundary condition between tumor tissue and normal tissue is unknown. In the normal tissue region, there is no power deposition, the temperature field is unknown and the internal boundary condition between tumor tissue and normal tissue is partially unknown. The algorithm is shown as

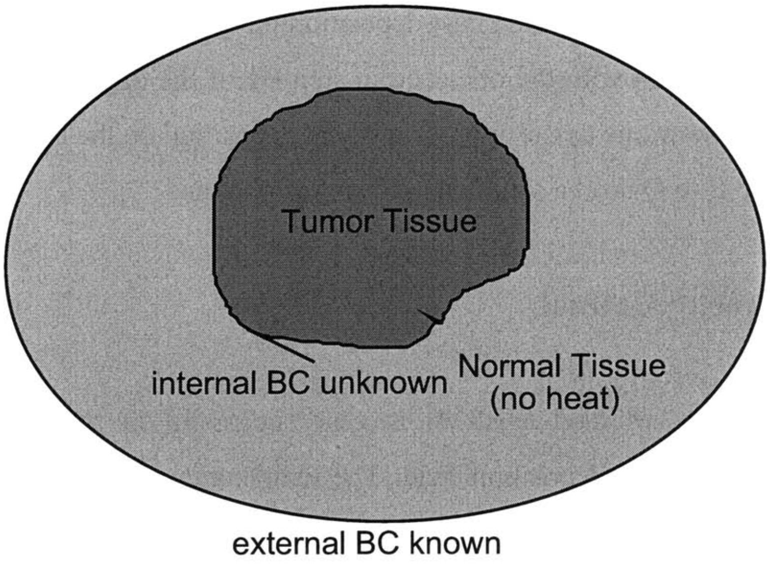

Figure 3-2 Schematic diagram of the tissue regions and boundaries for inverse FEM

A. Initial calculation

A1: Divide the domain under consideration into two regions: tumor tissue region and normal tissue region. The tumor tissue region is generally enclosed by normal tissue region. Form $\boldsymbol{K_T}$ matrix and $\boldsymbol{K_q}$ matrix for the two regions respectively

A2: Initialize the temperature distribution in the tumor tissue region to the optimal therapeutic temperature, typically 42~43°C. Initialize the external boundary condition of the normal tissue region accordingly.

A3: Guess the boundary heat source between normal tissue region and tumor tissue region.

B. The calculation of temperature in the normal tissue region

B1: Form the effective stiffness matrix and the effective load matrix for the temperature calculation in the normal tissue region.

B2: Solve the temperature distribution in the normal tissue region by a matrix solver.

C. The calculation of heat deposition in the tumor tissue region

C1: Form the effective stiffness matrix and the effective load matrix for the calculation of heat deposition in the normal tissue region.

C2: Solve the heat deposition distribution in the tumor tissue region by a matrix solver.

D: Comparison and loop control

D1: Compare the newly calculated heat deposition on the boundary between the normal and tumor tissue region with the one used in step B1, if the difference is beyond a tolerate limit, use the new one as the appropriate heat deposition on the boundary.

D2: Repeat step B to D until a satisfied precision is obtained.

Finite Basis Element Method

Finite Basis Element Method (FBEM) is very successful in the direct computation of temperature field from power deposition field. The temperature field can be calculated directly from power deposition field without any information of the temperature in neighboring nodes. Due to the nature of direct calculation, it is fast and does not need lots of memory to store any matrix. For inverse computation, the power deposition field is unknown. Iteration is needed in order to adjust the power deposition field to the optimal temperature field.

The domain for inverse FBEM can be sketched in figure 3-3. The region can be divided into two parts, one is tumor tissue region and the other is normal tissue region. For FBEM, the temperature is calculated directly from the power source and we only need to optimize the temperature in the tumor tissue region. Therefore the iteration region is only in the tumor tissue region. This is quite different from FEM where the whole region needs to be included in iteration. This is an advantage of FBEM over FEM in inverse calculation.

The iterative algorithm is given as:

1. Guess initial power deposition field
2. Calculate the temperature node by node, and adjust the power with a relaxation factor accordingly.
3. Calculate the error after iteration. Repeat 2 until the error is acceptable.

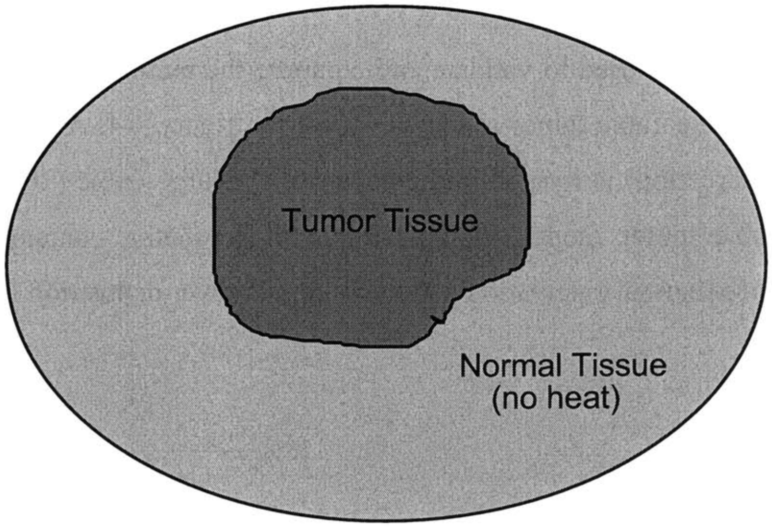

Figure 3-3 Schematic diagram of the tissue regions and boundaries for inverse FBEM

The discretized linear equations of FBEM can be expressed in matrix form as:

$$\boldsymbol{Ax} = \boldsymbol{b} \qquad (3.10)$$

where the stiffness matrix is the addition of three special matrix, $\boldsymbol{A}$=$\boldsymbol{D}$+$\boldsymbol{U}$+$\boldsymbol{L}$, where $\boldsymbol{D}$ is a diagonal matrix, $\boldsymbol{U}$ is a upper triangular matrix and $\boldsymbol{L}$ is a lower triangular matrix. We introduce an iterative routine:

$$\boldsymbol{Mx}^{n+1} = \boldsymbol{Mx}^{n} + (\boldsymbol{b} - \boldsymbol{Ax}^{n}) \qquad (3.11)$$

or

$$\boldsymbol{x}^{n+1} = \boldsymbol{x}^{n} + \boldsymbol{M}^{-1}(\boldsymbol{b} - \boldsymbol{Ax}^{n}) \qquad (3.12)$$

where $\boldsymbol{M}$ is an auxiliary matrix. The auxiliary matrix should be close to $\boldsymbol{A}$ and easy to compute its inversion. If we chose $\boldsymbol{M}$=$\boldsymbol{D}$+$\boldsymbol{L}$, the iterative routine is called Gauss-Seidel iterative method.

$$\boldsymbol{x}^{n+1} = (\boldsymbol{D} + \boldsymbol{L})^{-1}(-\boldsymbol{U})\boldsymbol{x}^{n} + (\boldsymbol{D} + \boldsymbol{L})^{-1}\boldsymbol{b} \qquad (3.13)$$

For Successive Over-Relaxation method (SOR), the iteration error is tuned up by a factor of ω,

$$\boldsymbol{x}^{n+1} = \boldsymbol{x}^{n} + \omega(\boldsymbol{D} + \boldsymbol{L})^{-1}(\boldsymbol{b} - \boldsymbol{Ax}^{n}) \qquad (3.14)$$

From the observation of simulation results, the SOR method performed much more efficiently compared to Gauss-Seidel iteration method. The optimal relaxation factor can be obtained by trial and error method.

Cubic Tumor Model

A cubic tumor model is used to validate and compare the numerical algorithms presented in the previous session. The cubic tumor model is showed in figure 3-4. A small cubic tumor (100 mm length in each direction) is located in the center of the large cubic (200 mm length in each direction). This cubic tumor model, though simple in geometry, contains all the important features of the inverse thermal calculation and the optimal power deposition field.

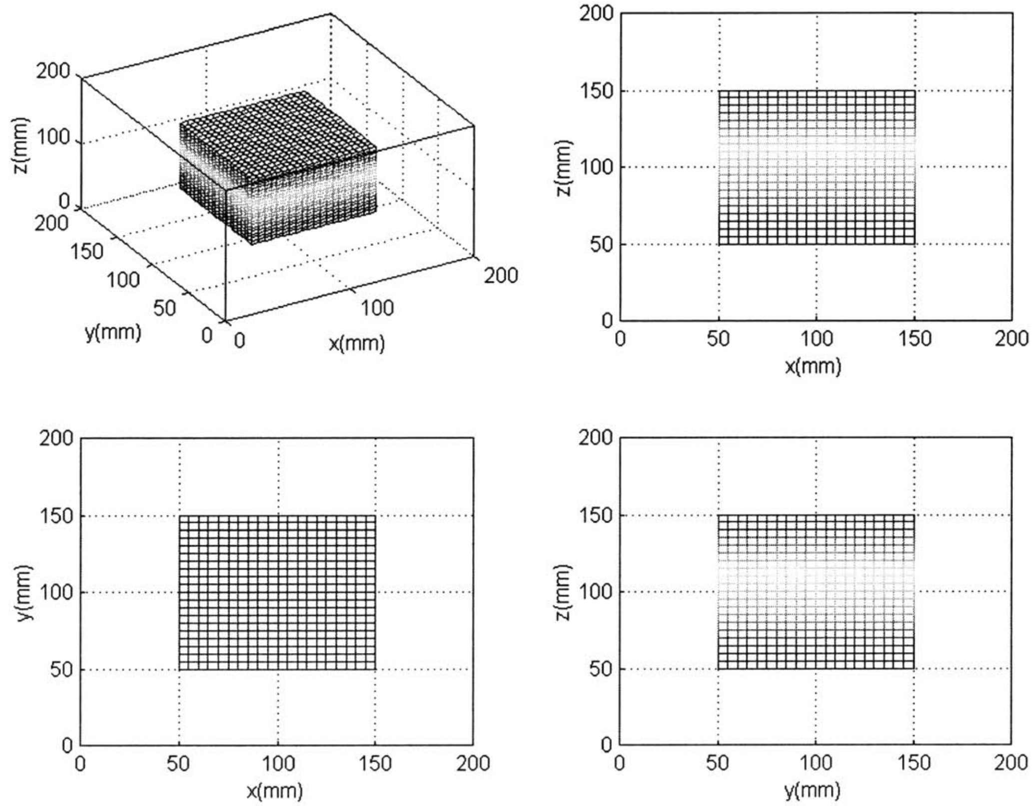

Figure 3-4 The geometry of a cubic tumor model

Since it has been proved that both FEM and FBEM can handle irregular domain and property irregularity, so we expect that the conclusion from simple geometry should be able to extended to more complex geometry.

The tissue thermal properties, perfusion and other parameters used in the simulation are shown in Table 3-1. These properties are typical tissue properties. For simplicity, we assume these properties are uniform in the region.

$\omega=1.996x10^{-3}\ (1/s)$	local perfusion rate
$W=11.98\ (ml/min\text{-}100g)$	clinical perfusion rate
$\rho_b=1000\ (kg/m^3)$	blood density
$k_m=0.5\ (W/m°C)$	tissue thermal conductivity
$c_b=4.175\ (kJ/kg°C)$	blood specific heat
$L_p=0.007746\ (m)$	perfusion length
$Q=5x10^4\ (W/m^3)$	absorbed power

Table 3-1 Tissue thermal properties, perfusion and other parameters used in the numerical simulation

Results for Finite Element Method

The numerical results are showed in Figure 3-5 Inverse FEM for Cubic Tumor Model. The figure consists of four subplots. The plot in the upper-left corner is the temperature field for the central plane of z, i.e. z = 100mm. It looks like a "highland". The plot in the lower-left corner is another view of temperature profile for the central line of y and z plane, i.e. y = z = 100mm. This temperature profile agrees with the results we get from one-dimensional analytical solution in the previous session. The plot in the upper-right corner is the power deposition field for the central plane of z. It looks like a "castle". The plot in the lower-right corner is another view of power profile for the central line of y and z plane. The plots show that more power is deposited on the tumor boundary to compensate the heat flux. Since the temperature gradient is not continuous on the boundary, a boundary delta function is expected. For the internal tumor region, there is no temperature gradient. The power is used to compensate the effect of perfusion. The results are what we expected from analytical solution.

The iterative solution converges very fast. The satisfied results can be obtained within about 3~5 iteration.

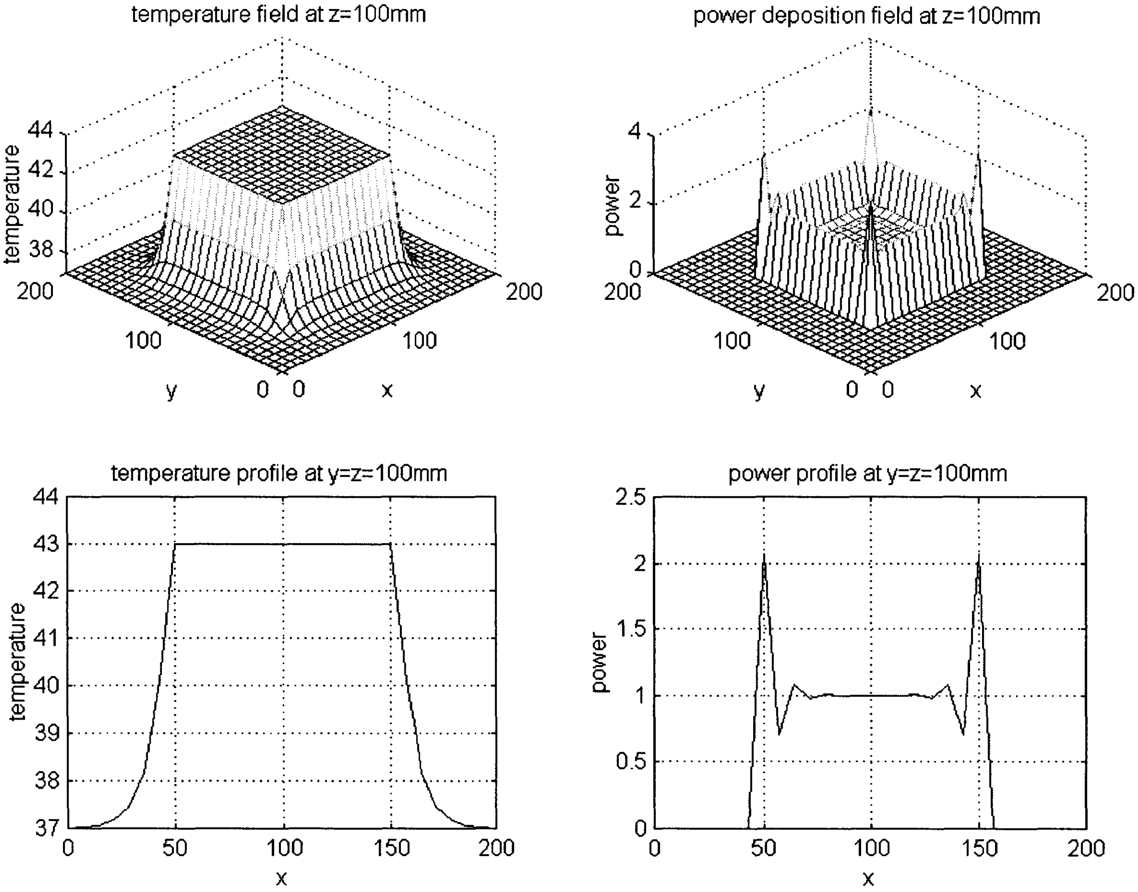

Figure 3-5 Power and temperature distribution for inverse thermal analysis: desired power field (Inverse FEM, cubic tumor model, central plane view)

Results for Finite Basis Element Method

Similar results from inverse FBEM are showed in Figure 3-6. The results are very close to what we get from inverse FEM. Inverse FBEM needs more iteration compared to inverse FEM. The results can be obtained after about 7~9 iteration, which also depends on the tolerate error level and the choice of relaxation factor. This is a disadvantage of inverse FBEM. However, a smaller iteration region in inverse FBEM provides advantage of inverse FBEM over a larger iteration region in inverse FEM. Overall, inverse FBEM is still close to an order of magnitude faster than FEM.

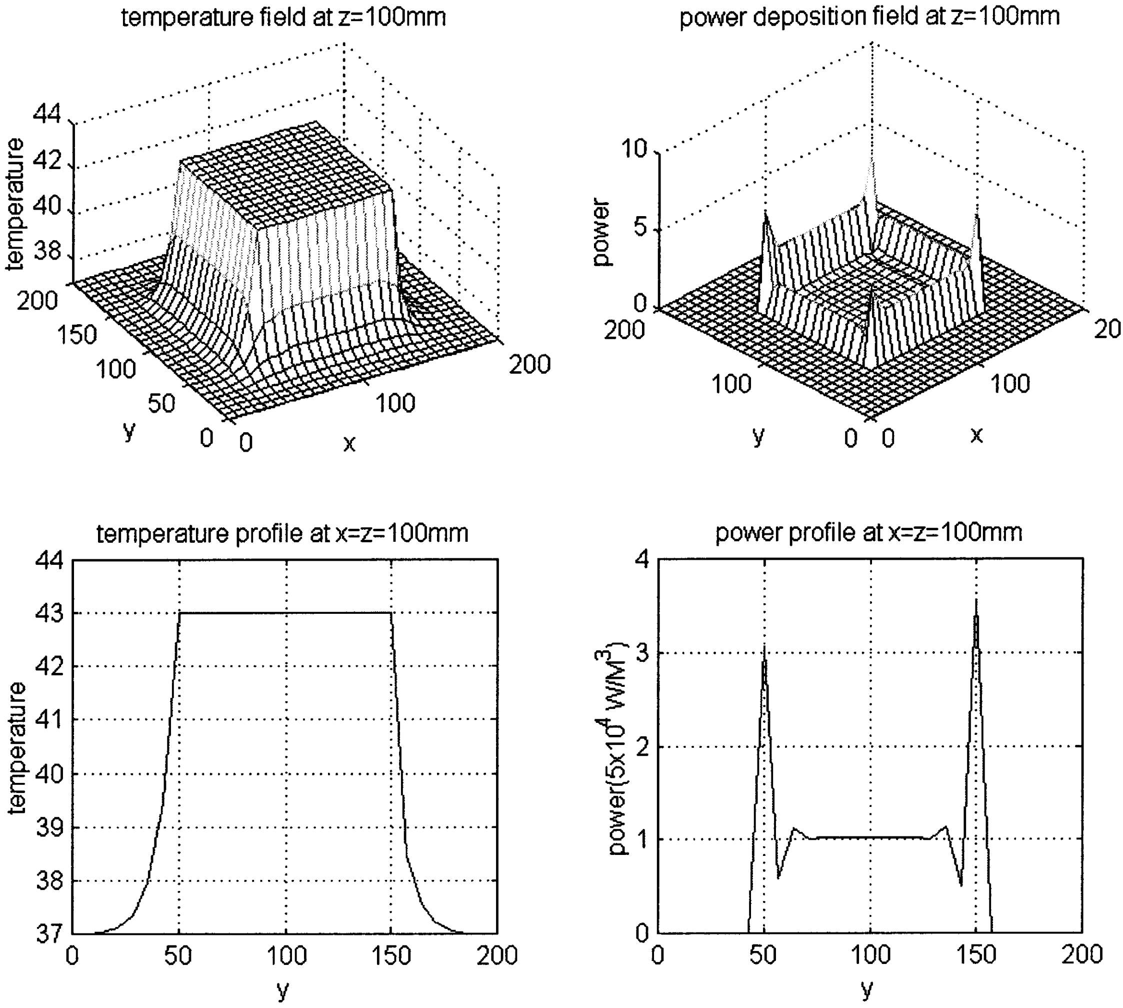

temperature field at z=100mm

power deposition field at z=100mm

temperature profile at x=z=100mm

power profile at x=z=100mm

Figure 3-6 Power and temperature distribution for inverse thermal analysis: desired power field (Inverse FBEM, cubic tumor model, central plane view)

The optimal power fields obtained here require point source and surface source at some specific points or on the boundaries. The infinite energy intensity at singular point or on surface can hardly be produced by current energy delivery machine. In order to overcome the limitation, optimization methods, which take into account the current status of energy delivery machine, will be introduced in the next session.

Speed-Accuracy Comparison

The iteration speed-accuracy comparisons for inverse FEM and inverse FBEM are showed in Figure 3-7. For the FBEM, three sizes of elements are used, which are represented by the three levels of desired accuracy, i.e. medium accuracy, low accuracy and lower accuracy. The computational time for FBEM with low and lower accuracy is shorter than that of FEM even with the same RMS error. However, FEM has speed advantage over FBEM with medium accuracy. Therefore the advantage of FBEM in computational speed is for relative large element size.

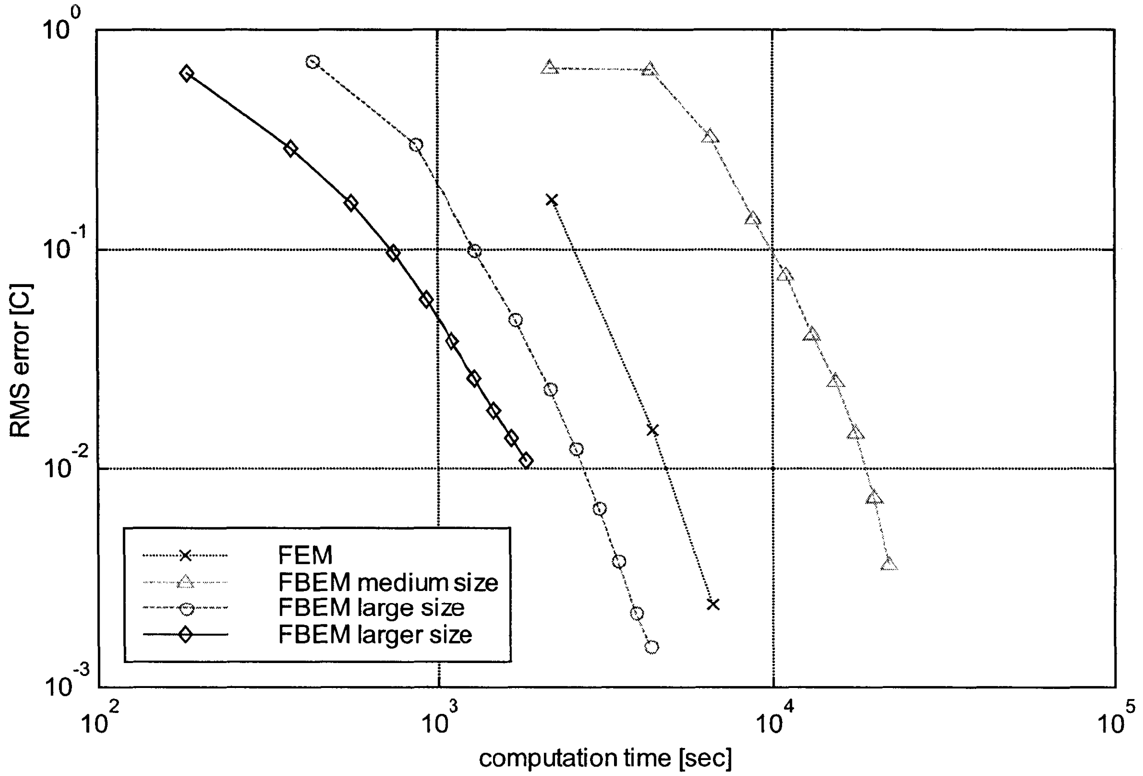

Figure 3-7 Iteration speed-accuracy comparisons for inverse FEM and inverse FBEM

3.4 Combined Inverse Thermal Analysis

In clinical application, it is more desirable to relate the temperature of a target domain directly to the control parameter of the power delivery instruments, for example, power magnitude of transducers. The general relation between temperature and power field can be showed as:

$$[T_{n\times 1}] = [E_{n\times n}] \cdot [Q_{n\times 1}] \qquad (3.15)$$

where T_{nx1} is temperature matrix, E_{nxn} is power coefficient matrix, n is the number of nodes used, Q_{nx1} is the power matrix, which can be further expressed as:

$$[Q_{n\times 1}] = [F_{n\times m}][P_{m\times 1}] \qquad (3.16)$$

where F_{nxm} is a power control coefficient matrix, which relates the power matrix Q_{nx1} to the control matrix P_{mx1} of energy delivery machine. m is the number of the control parameters in the energy delivery machine. The two processes can be combined as:

$$[T_{n\times 1}] = [G_{n\times m}][P_{m\times 1}] \qquad (3.17)$$

where:

$$[G_{n\times m}] = [E_{n\times n}][F_{n\times m}] \qquad (3.18)$$

G_{nxm} is feedback matrix of inverse procedure. The size of control matrix *(m)* is limited by the current status of the energy delivery machine. For example, the ultrasound machine we currently used (FSUM) has 56 transducers, i.e. *Max(m)=56*. There is no limit on the size of the temperature matrix *(n)*, which can be chosen according to accuracy requirement and efficiency in computation. If $n=m$, equation (3.17) gives an exact solution to power control matrix. If $n>m$, there is no exact solution for P, an inverse least-squares procedure can give the best estimate:

$$[P_{m\times 1}] = [H_{mxn}][T_{n\times 1}] \qquad (3.19)$$

$$[H_{m\times n}] = ([G'][G])^{-1}_{mxm}[G']_{mxn} \qquad (3.20)$$

where H_{mxn} is the inverse control matrix we are looking for. The size of the matrix needed to inverse has been reduced to m by m, therefore it is quite easy to inverse. The additional advantage of least-squares approach is that weight factor can be integrated into the procedure to protect selected locations from overheating.

3.4.1 Normalized Source and Source Array

There are many heating methods currently used in hyperthermia. Most of them involve delivery of wave energy to the target tissue. The wave energy is converted to thermal energy through the process of absorption. Although it is quite straight forward in theory that given the specification of an applicator, the tissue geometry and its properties, the power deposition field should be able to predict. In practice, significant simplification must be made in order to derive a practical solution method.

Many energy delivery machines have multiple transducers in order to produce more complex power field. Each transducer can be controlled individually. For example, a Focused Segmented Ultrasound Machine (FSUM) is currently used in DFCI. It has 56 plane wave, non-phased square transducers mounted in a hemispherical shaped applicator. When a concentrated source (focused source) is used to heat a target tumor region, the resulting power deposition field may probably be normalized as Gaussian distribution.

The temperature distribution for a Gaussian source (e^{-r^2}) in infinite free space is derived by Martin (1995) as:

$$\theta = \frac{1}{4r} e^{Pe/4} \left[e^{-r\sqrt{Pe}} erfc\left(\frac{1}{2}\sqrt{Pe} - r \right) - e^{r\sqrt{Pe}} erfc\left(\frac{1}{2}\sqrt{Pe} + r \right) \right] \qquad (3.21)$$

The Gaussian Power distribution and the resulting temperature distribution are showed in Figure 3-8. The plots in the left column show the power field of Gaussian source and the right column show the resulting temperature field.

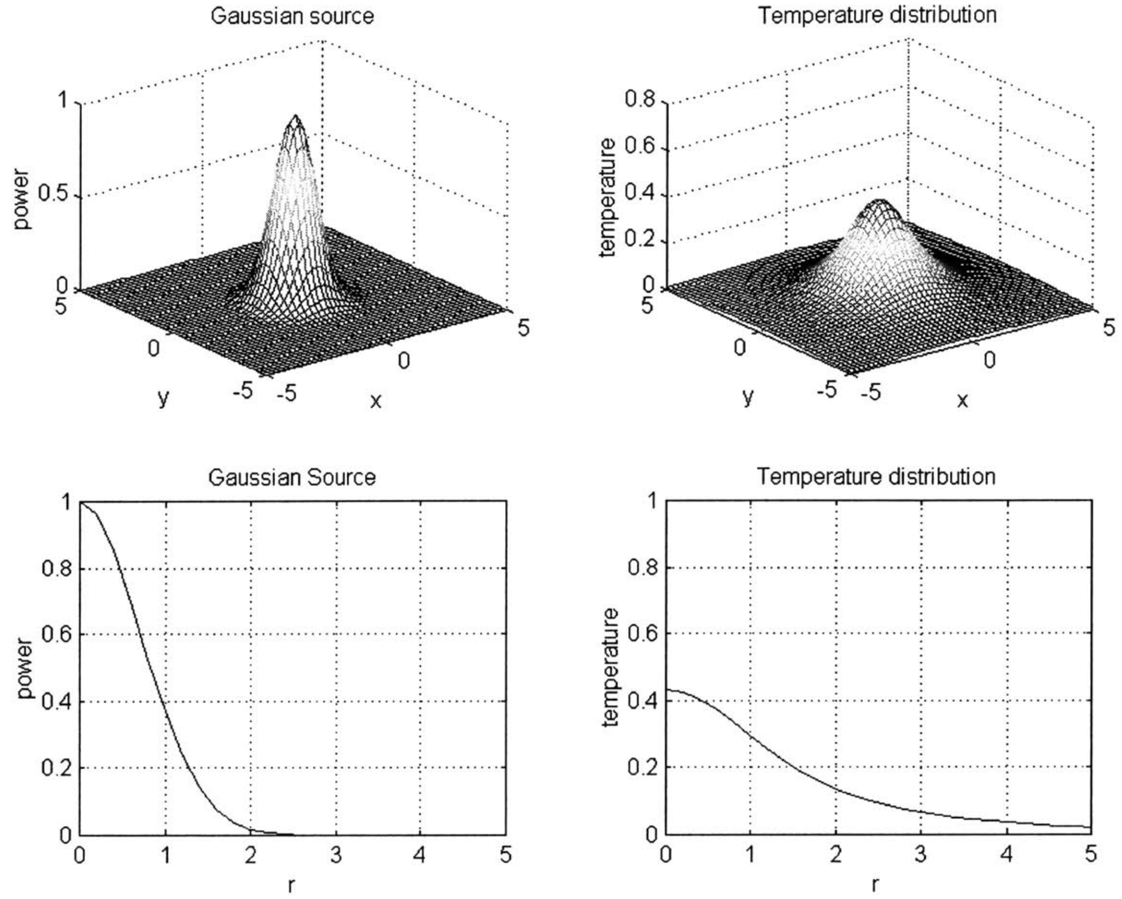

Figure3-8 Gaussian source and resulting temperature distribution (Pe=0.1)

If we can use a normalized source to describe the effect of single transducer, the effect of multiple transducer can be describe as the effect of many normalized sources. If the placement of the transducers can be arranged individually, we can place the transducers to from a source array. We can choose the source placement and the intensity of the individual source wisely to achieve an optimal temperature field.

3.4.2 Cubic Tumor Model

Exactly the same cubic tumor model is used for the combined inverse thermal analysis. The heating sources are normalized source array. The source array consists of 64 sources. The strength of the source can be adjusted individually. The source placement is showed in Figure 3-

9 for 3-D view. The centers of the sources are placed on the grid point of the four layers. There are 4 sources in one direction, 4×4 (16) on one surface (layer) and 4×4×4 (64) in the tumor region. The sources are placed in equal-distance with respect to each other.

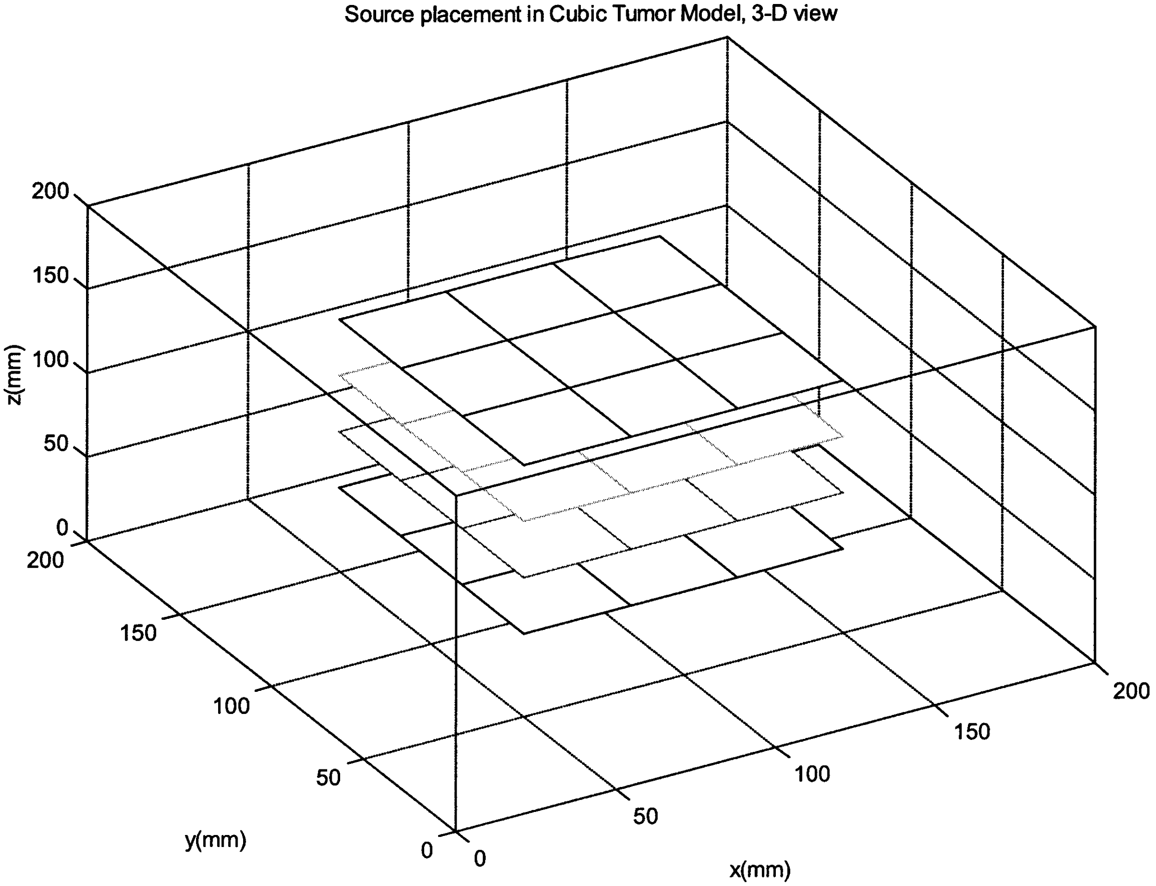

Figure 3-9 Source placement in cubic tumor model, 3-D view

Figure 3-10 shows the 2-D cross section view of the source placement in cubic tumor model. Most of the sources (56 out of 64) are placed on the boundary between tumor tissue and normal tissue. Only 8 sources are placed inside the tumor region. The source placement is consistent with the analysis from one-dimensional analytical solution. It is a good practice to place more heating sources on the boundary in order to compensate the heat loss on the boundary. The sources inside the tumor region are used to compensate the heat carried out by blood perfusion.

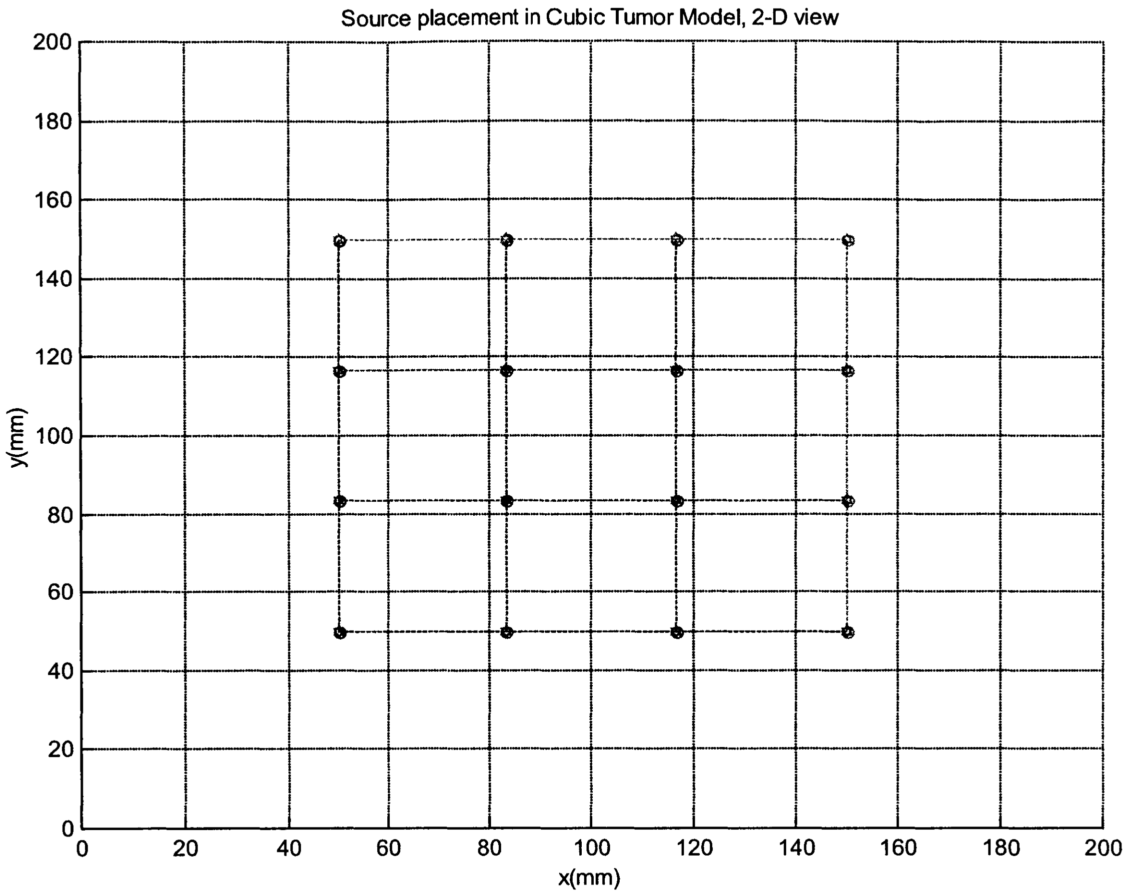

Figure 3-10 Source placement in cubic tumor model, 2-D cross-section view

The results are showed in Figure 3-11 for central plane view. The left column plots in the figure are power deposition field, where the upper plot is a 3-D view and the lower plot is a 2-D contour view. The right column plots in the figure are temperature field, where the upper plot is a 3-D view and the lower plot is a 2-D contour view. The temperature distribution inside the tumor region is close to uniform temperature around 43°C. The power intensity on the boundary is higher than those inside the tumor in order to compensate the heat loss through the boundary.

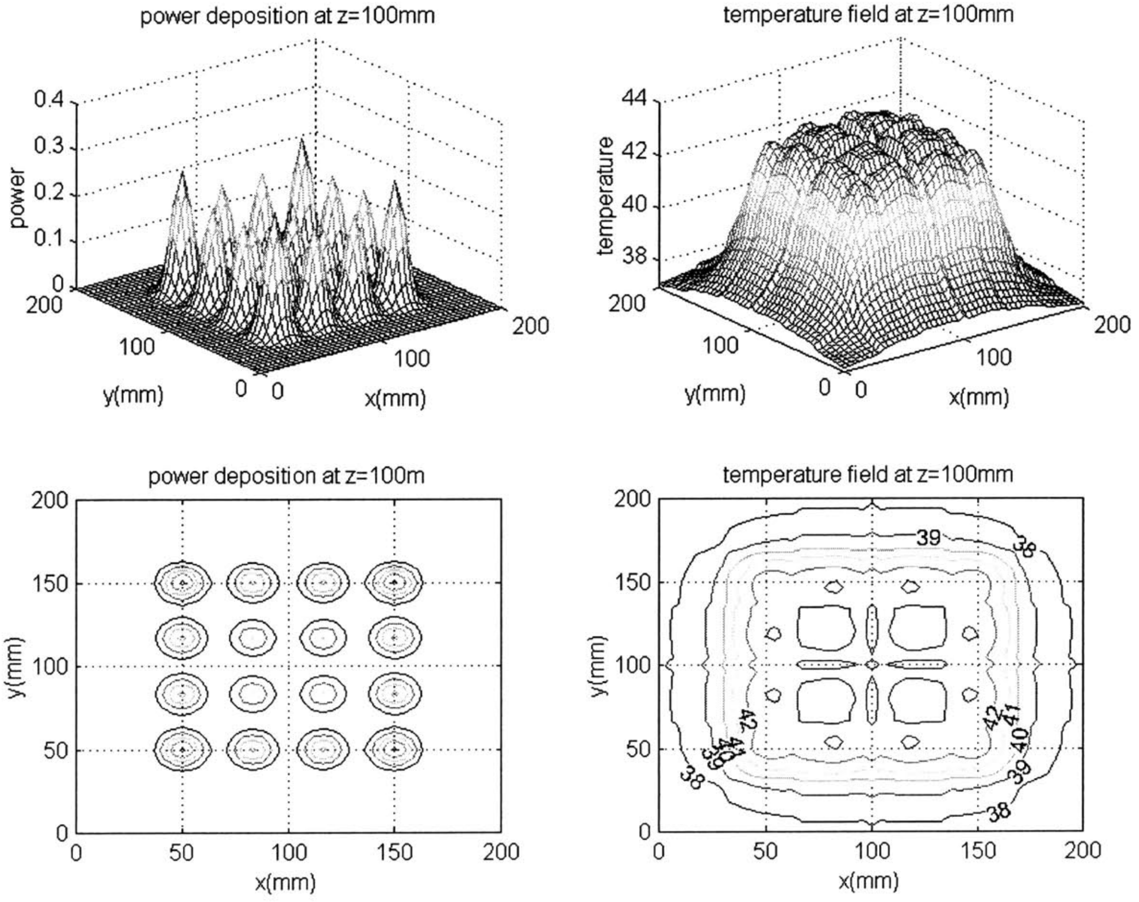
power deposition at z=100mm

temperature field at z=100mm

power deposition at z=100m

temperature field at z=100mm

Figure 3-11 Power and temperature distribution for combined inverse thermal analysis

(Cubic tumor, central plane view, Pe=0.1, RMS = 0.57°C)

Figure 3-12 shows the results for boundary plane view. The temperature disparities are much larger on the boundary than those inside the tumor region. The power intensities on the boundary are much higher than those inside the tumor region. The temperature fluctuation is also much higher on the boundary. We can see that overheating occurs within very small volume of the source focus point. Overall, the root mean square (RMS) of temperature disparity is reasonable (about 10% of temperature elevation).

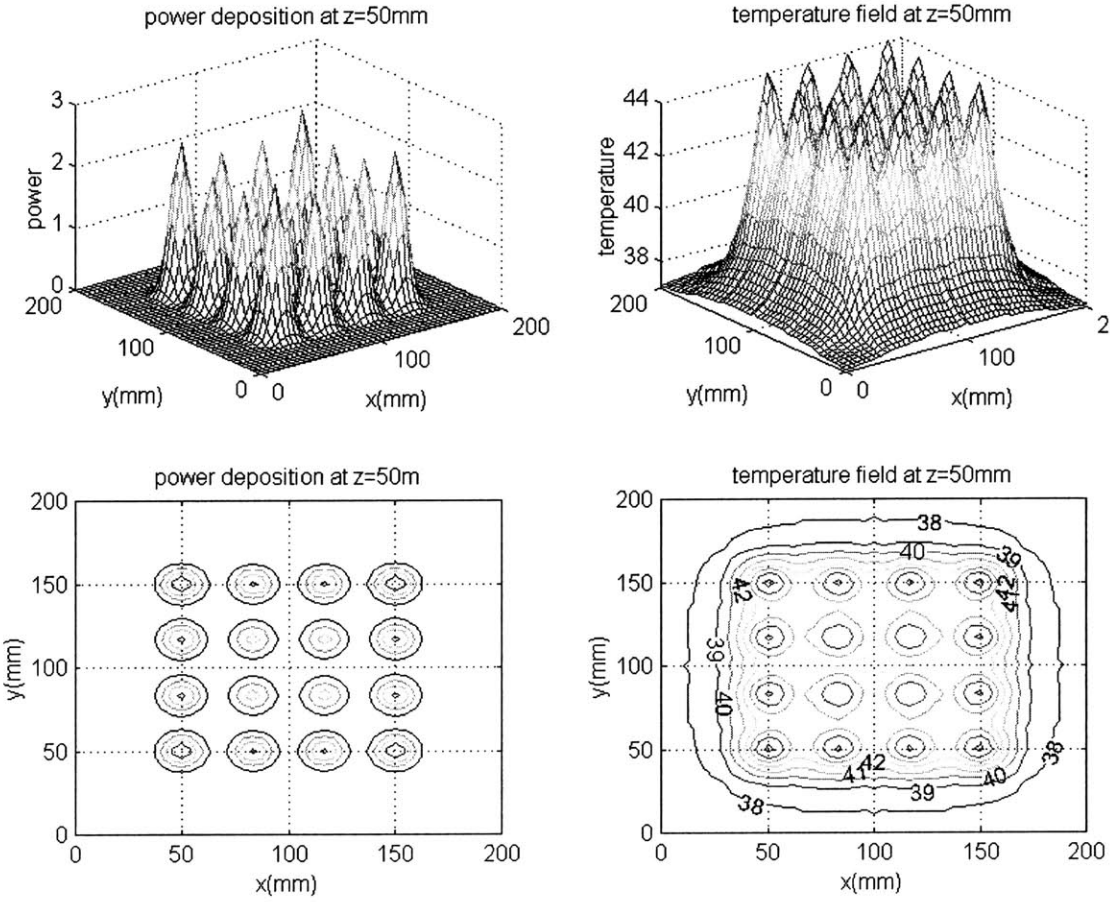

Figure 3-12 Power and temperature distribution for combined inverse thermal analysis (Cubic tumor, boundary plane view, Pe=0.1, RMS = 0.57°C)

3.4.3 Spherical Tumor Model

A spherical tumor model is more realistic compared to the cubic tumor model we used before. Figure 3-13 shows the geometry of a spherical tumor model. The origin of spherical tumor is located at the center of the domain, i.e. at *x=100 mm, y=100 mm* and *z=100 mm*. The radius is 55.3 mm. The volume of the tumor is 0.708×10^6 mm^3, *70.8%* of the volume of the cubic tumor. The surface area is 3.84×10^4 mm^2, *64%* of the surface area of the cubic tumor.

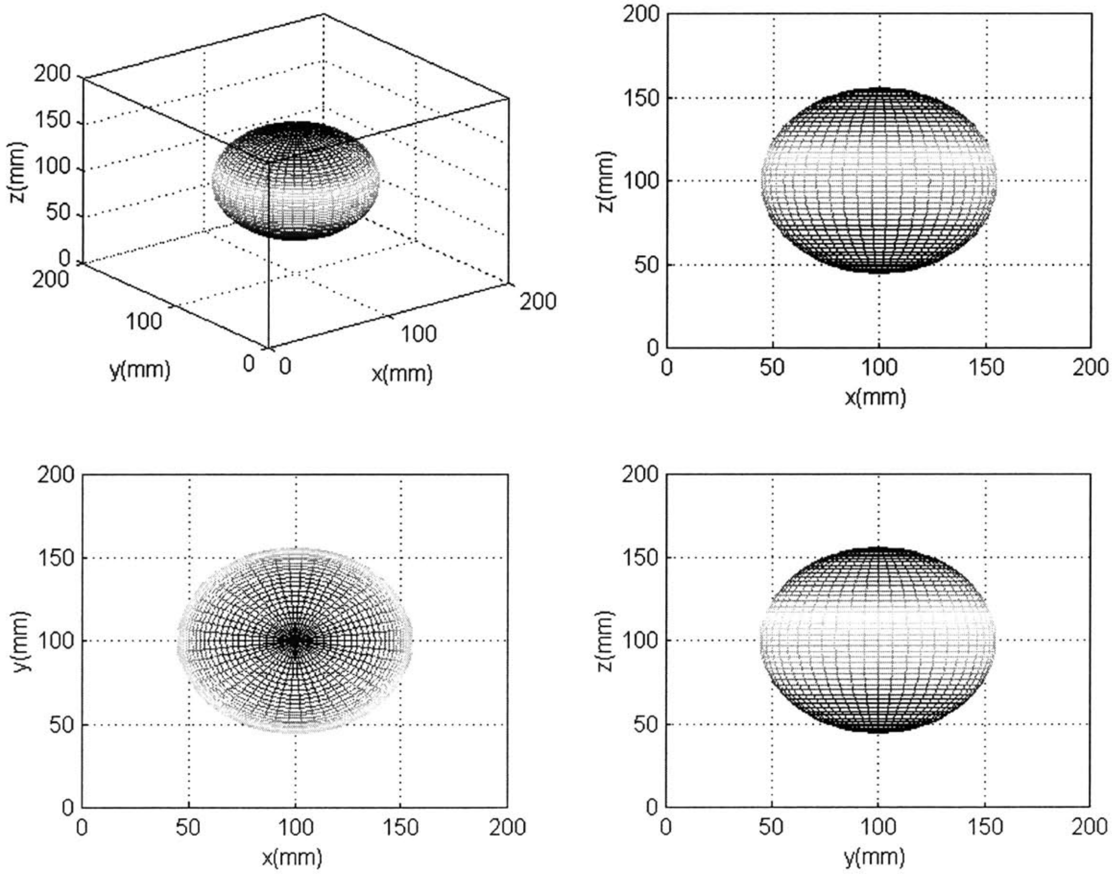

Figure 3-13 The geometry of a spherical tumor (radius 55.3 mm)

Same source placement scheme is used for the spherical tumor for simplicity and ease of comparison. Some of the sources are placed outside of the tumor so they have to be turned off. The cross-section view of source placement for the spherical tumor model is showed in Figure 3-14. Only 32 sources are placed inside the tumor region. 4 sources are placed on each of the boundary layers (*z=50* mm and *z=150* mm) and 12 sources are placed on each of the inner layers (*z=83.3* mm and *z=113.3* mm). There are 8 sources, or a quarter of the total sources, are inside the tumor. The remaining three quarters are placed on the boundary.

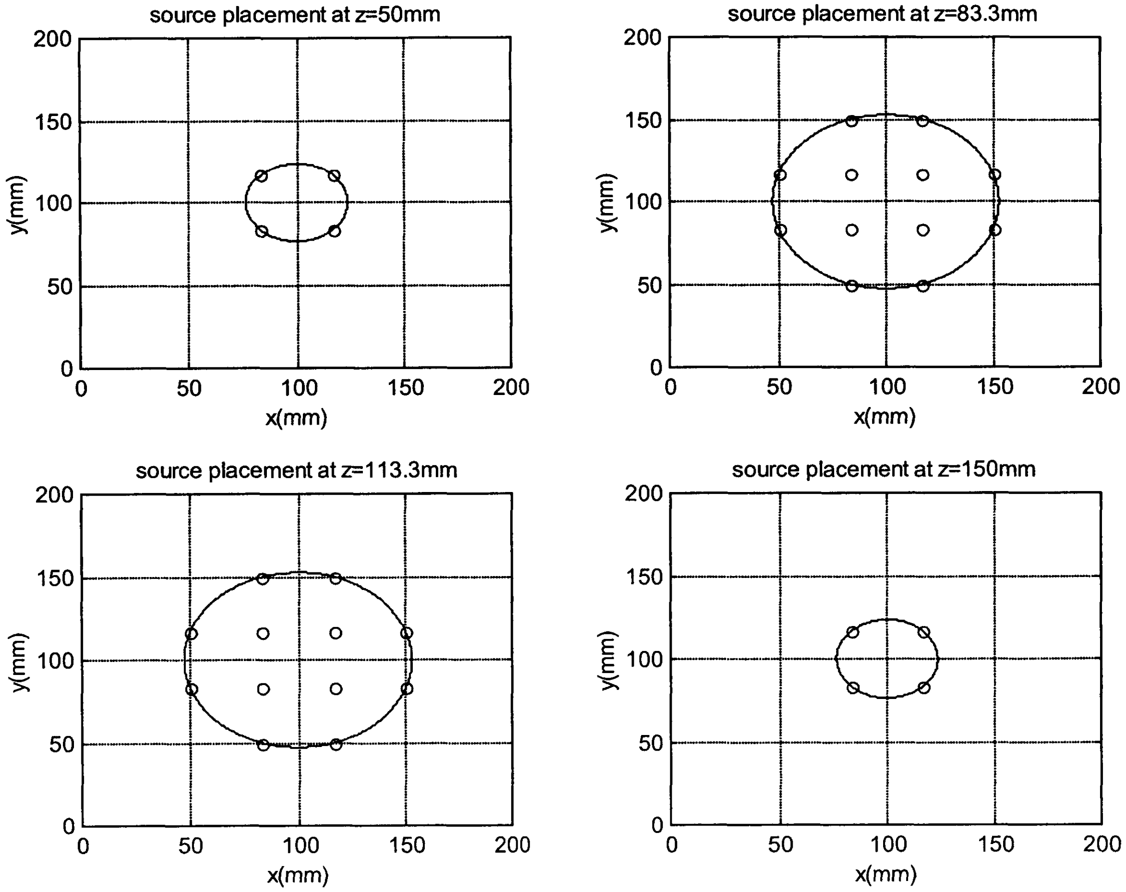

Figure 3-14 Cross-section view of source placement for spherical tumor model

Figure 3-15 shows the central plane view of the power and temperature distribution. The left column plots in the figure are power deposition field, where the upper plot is a 3-D view and the lower plot is a 2-D contour view. The right column plots in the figure are temperature field, where the upper plot is a 3-D view and the lower plot is a 2-D contour view. The figure shows higher power intensity for boundary sources and lower power intensity for inner sources. The temperature distribution is close to uniform inside the tumor region.

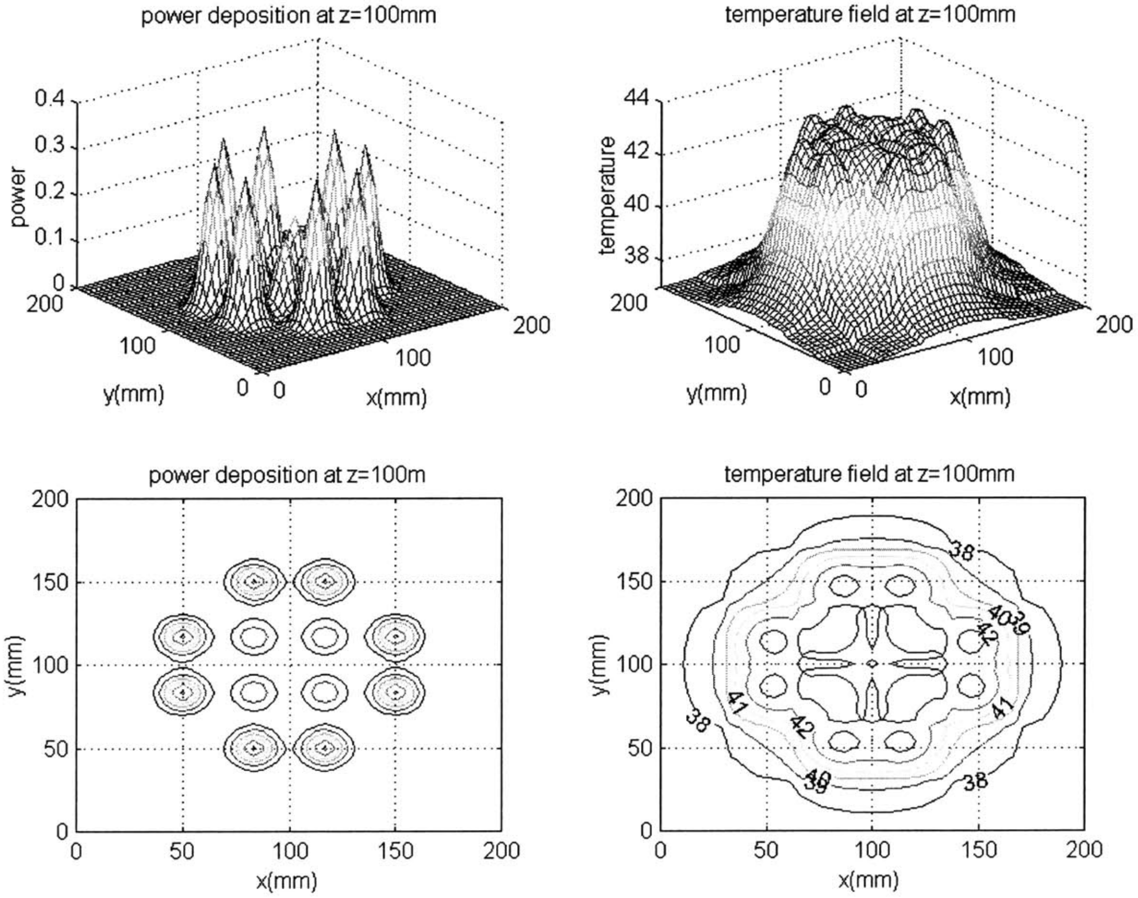

Figure 3-15 Power and temperature distribution for combined inverse thermal analysis (Spherical tumor, central plane view, Pe=0.1, RMS = 0.8322°C)

Figure 3-16 shows the boundary plane view of the power and temperature distribution. The power intensities on the boundary are higher, as well as the temperature fluctuation. Overheating can also be found within a small volume of the focus points. The RMS is 0.8322°C, which is higher than the RMS in cubic tumor model. But it is still within a reasonable range. One interesting fact is that the volume of the spherical tumor is 70.8% of the volume of the cubic tumor; the surface area of the surface area of the spherical tumor is 64% of the surface area of the cubic tumor model; the sources are half of the sources placed in cubic tumor. There is less number of sources per unit area or per unit volume in the spherical tumor. This is one of the reasons that the RMS in the spherical tumor model is higher than that of the cubic tumor model. Other factors can be the shape of the tumor and the choice of source placement.

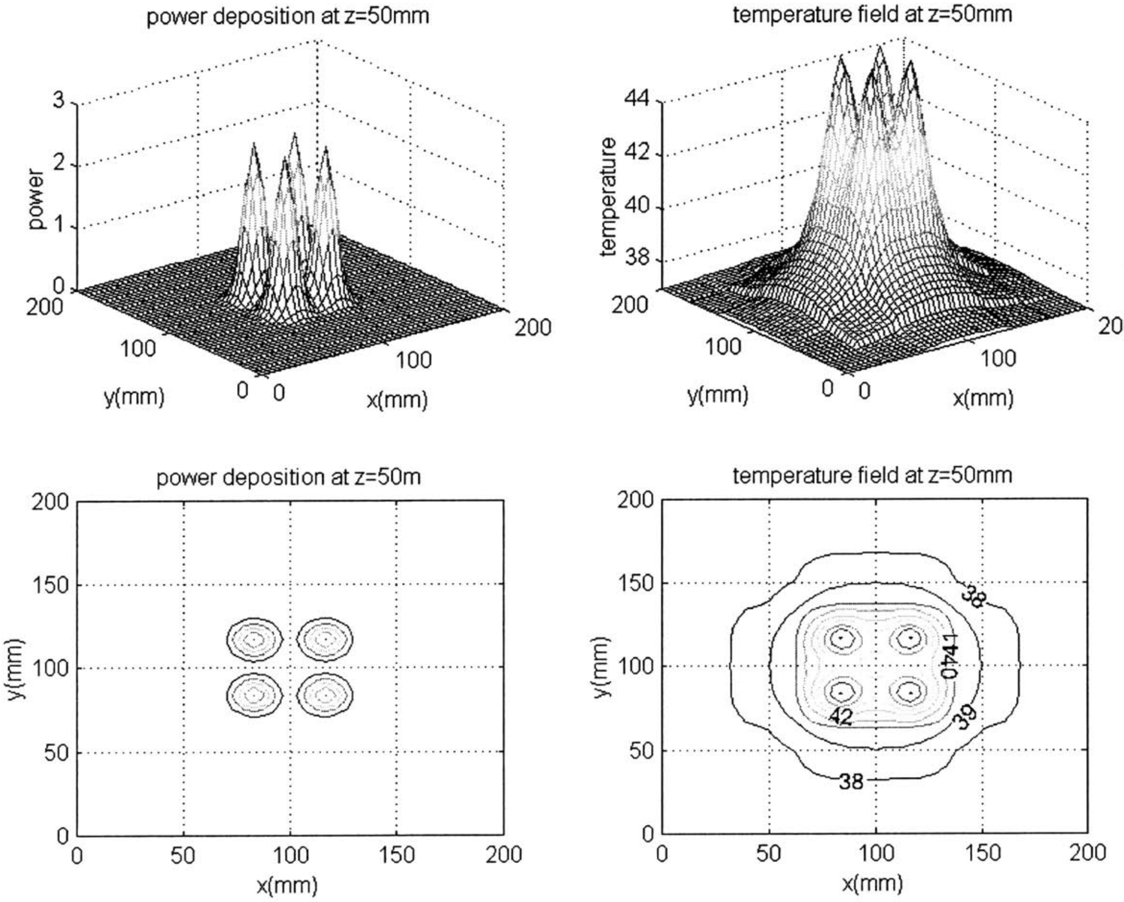

Figure 3-16 Power and temperature distribution for combined inverse thermal analysis (Spherical tumor, boundary plane view, Pe=0.1, RMS = 0.8322°C)

3.4.4 Ellipsoidal Tumor Model

The geometry of an ellipsoidal tumor model is showed in Figure 3-17. The center of the ellipsoidal tumor is located at the center of the domain, i.e. at $x=100\ mm$, $y=100\ mm$ and $z=100\ mm$. This spindle shaped ellipsoid is the surface revolution obtained by rotating an ellipse about its major axis. The polar radius c is 55.3 mm. The equatorial radius a is half of c, i.e. 27.6 mm. The volume of the ellipsoidal tumor is $0.177\times10^6\ mm^3$, *17.7%* of the volume of the cubic tumor and 1/4 of the volume of the spherical tumor. The surface area is $2.65\times10^4\ mm^2$, *44%* of the surface area of the cubic tumor and *69%* of the surface area of the spherical tumor.

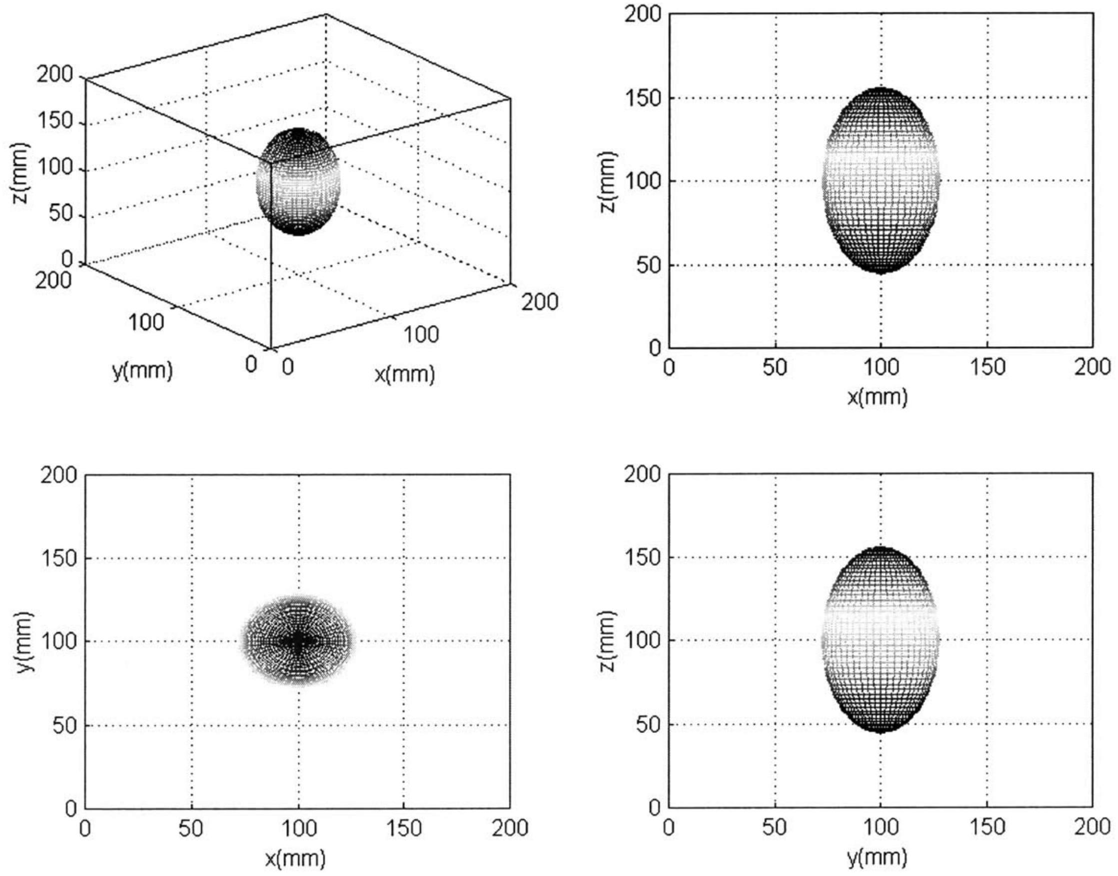

Figure 3-17 The geometry of an ellipsoidal tumor

First we use the same source placement scheme used before for the cubic tumor and spherical tumor for simplicity and ease of comparison. The sources that are placed outside of the tumor have to be turned off. The cross-section view of source placement for the ellipsoidal tumor model is showed in Figure 3-18. There are no sources on the first and last layers, or boundary planes. 4 sources are placed on each of the inner layers. All 8 sources are placed on the boundary.

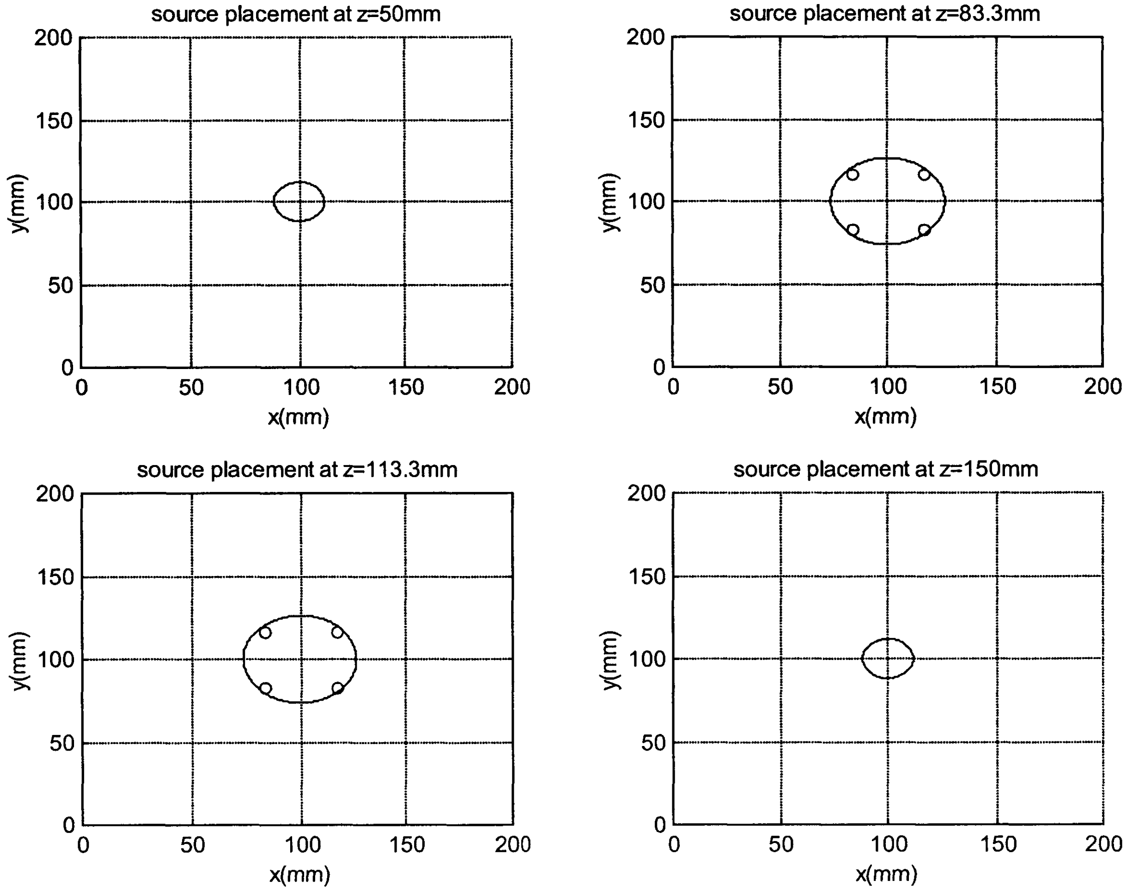

Figure 3-18 Cross-section view of source placement for ellipsoidal tumor

Figure 3-19 shows the central plane view of the power and temperature distribution for the ellipsoidal tumor model. The left column plots in the figure are power deposition field, where the upper plot is a 3-D view and the lower plot is a 2-D contour view. The right column plots in the figure are temperature field, where the upper plot is a 3-D view and the lower plot is a 2-D contour view. The figure shows the temperature distribution is close to uniform inside the tumor region.

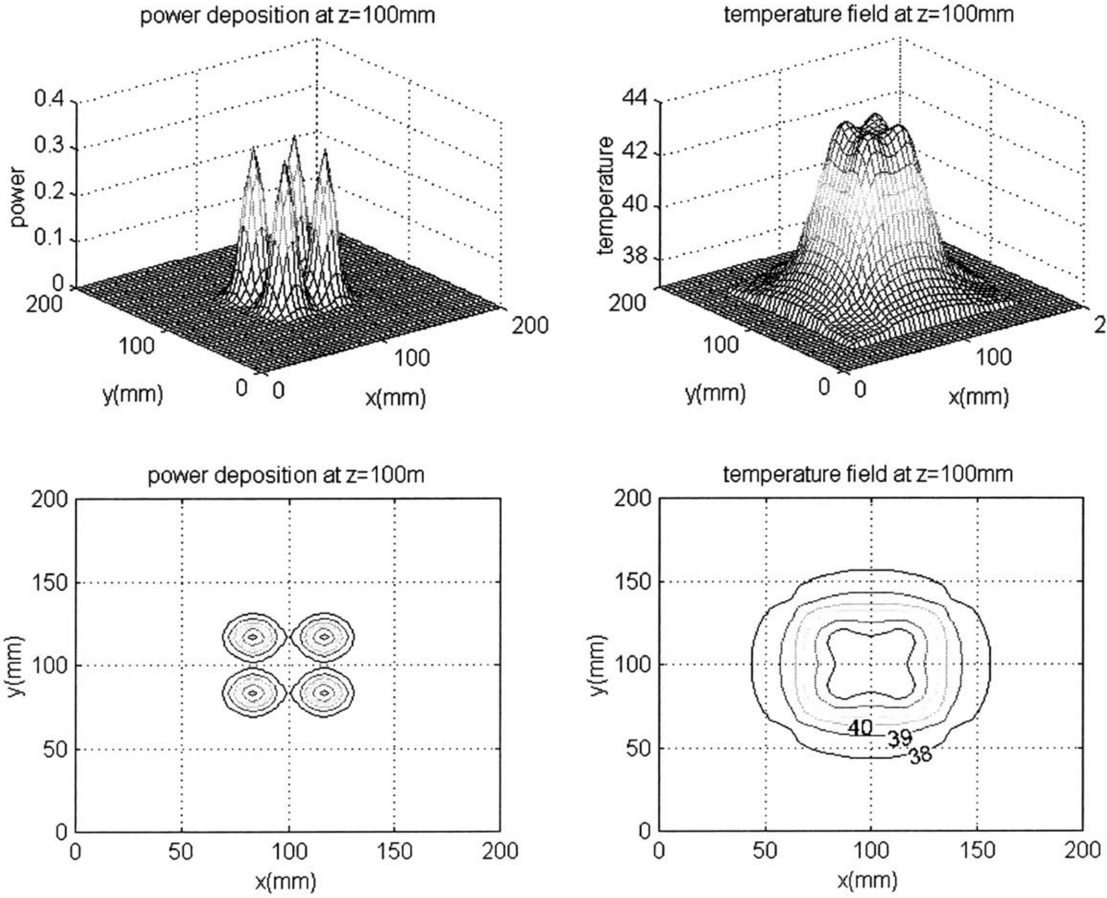

Figure 3-19 Power and temperature distribution for combined inverse thermal analysis (Ellipsoidal tumor, central plane view, Pe=0.1, RMS = 1.978°C)

Figure 3-20 shows the boundary plane view of the power and temperature distribution for the ellipsoidal tumor model. Since there is no source nearby, the temperature in the tumor region is really low at about 39°C comparing to the optimal temperature at 43°C. The RMS is 1.978°C, which is really unacceptable. The cause of the problem is unwisely source placement. There is no source to cover the region.

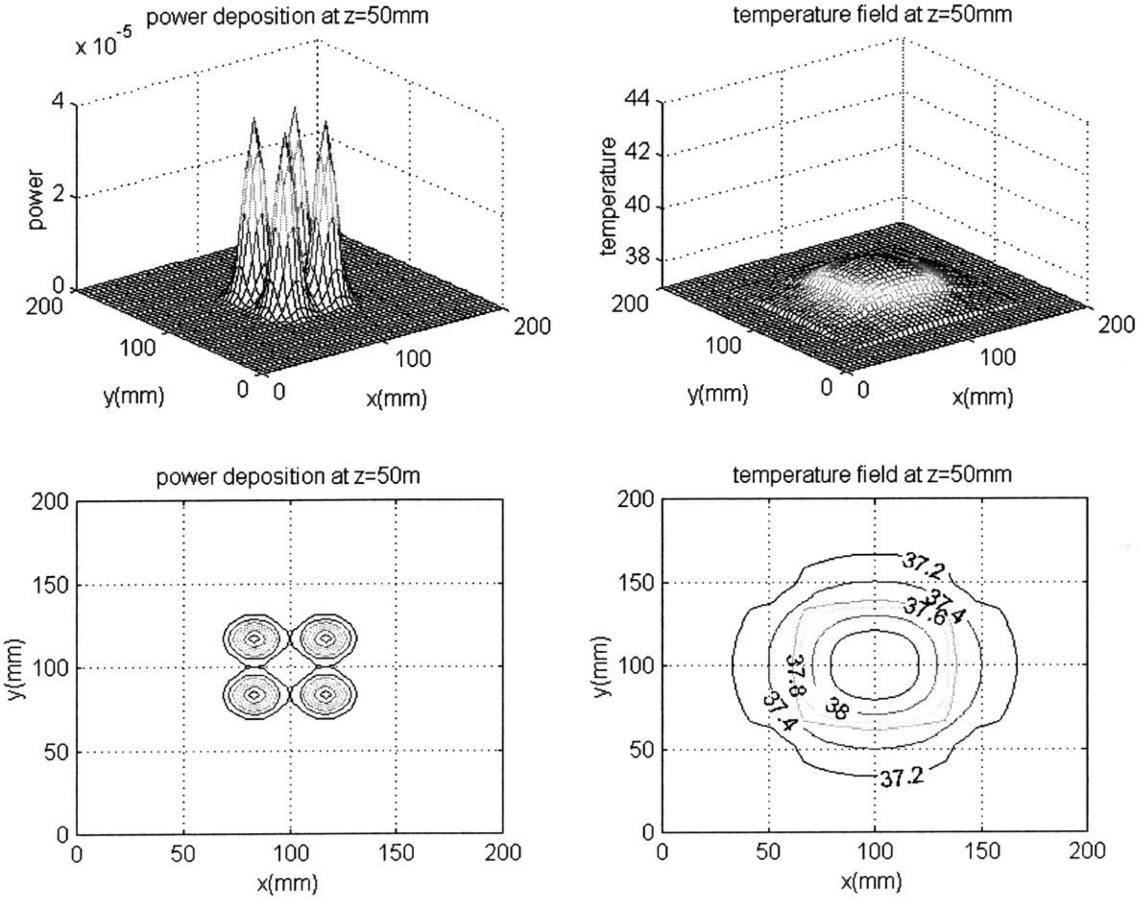

Figure 3-20 Power and temperature distribution for combined inverse thermal analysis (Ellipsoidal tumor, boundary plane view, Pe=0.1, RMS = 1.978°C)

3.4.5 Source Placement

Source placement is very important. Unwisely source placement might cause underheated or overheated, as showed in the previous session. Figure 3-21 shows a modified source placement for the ellipsoidal tumor model. A source is placed each of the boundary layers. Therefore the total number of sources increases to 10, which is 15.6% of the total sources used in the cubic tumor model and 31.2% of those in the spherical tumor model.

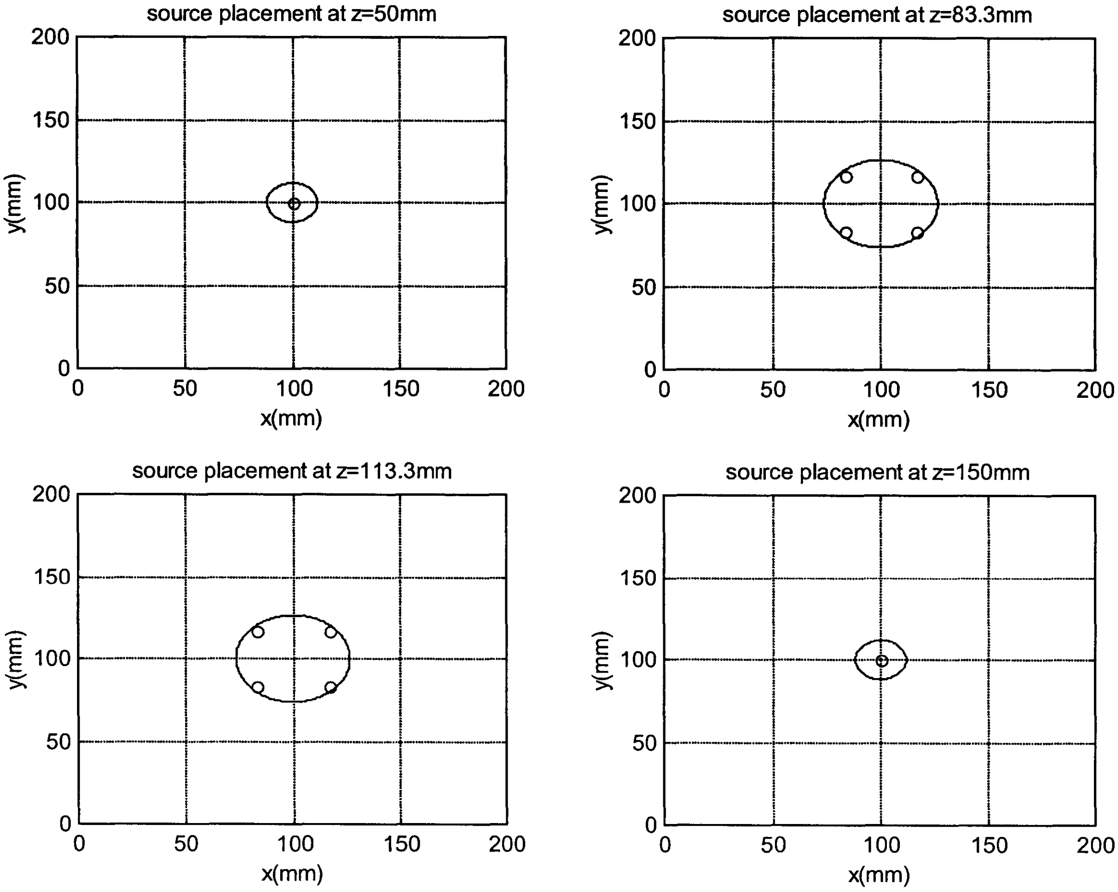

Figure 3-21 Source placement of ellipsoidal tumor (modified source placement)

Figure 3-22 shows the central plane view of the power and temperature distribution for the ellipsoidal tumor model, modified source placement. The temperature in the tumor region is close to the optimal temperature. We don't see much difference before and after the modified source placement on the central plane.

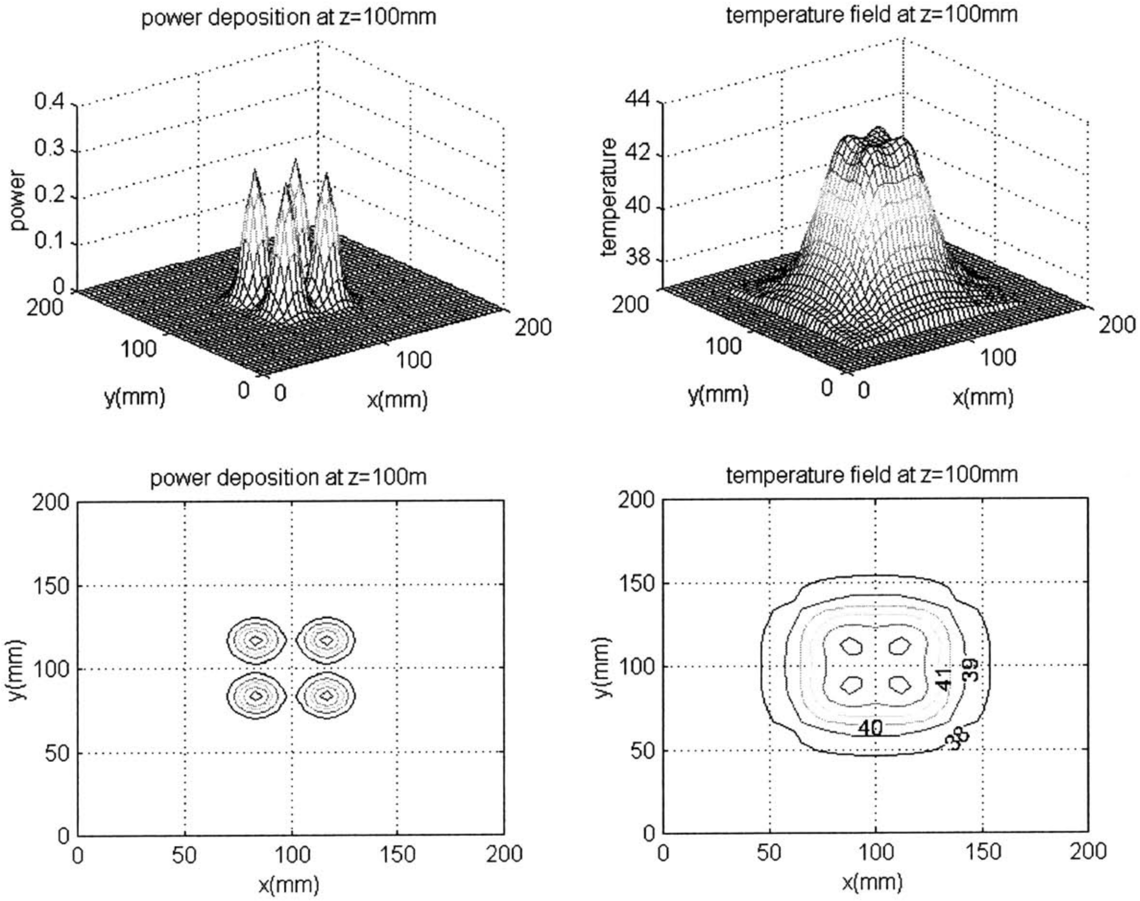

power deposition at z=100mm

temperature field at z=100mm

power deposition at z=100m

temperature field at z=100mm

Figure 3-22 Power and temperature distribution for combined inverse thermal analysis (Ellipsoidal tumor, modified source placement, central plane view, Pe= 0.1, RMS= 0.981°C)

Figure 3-23 shows the power and temperature distribution on the boundary plane. The temperature in the tumor region is close to optimal temperature, although overheat in a small volume near the source focus point is well noticed. The RMS drops to 0.981°C compared to 1.978°C in the previous scheme. This shows that the improvement in source placement can reduce the temperature disparity. Thus improve the effectiveness and safety of the therapy.

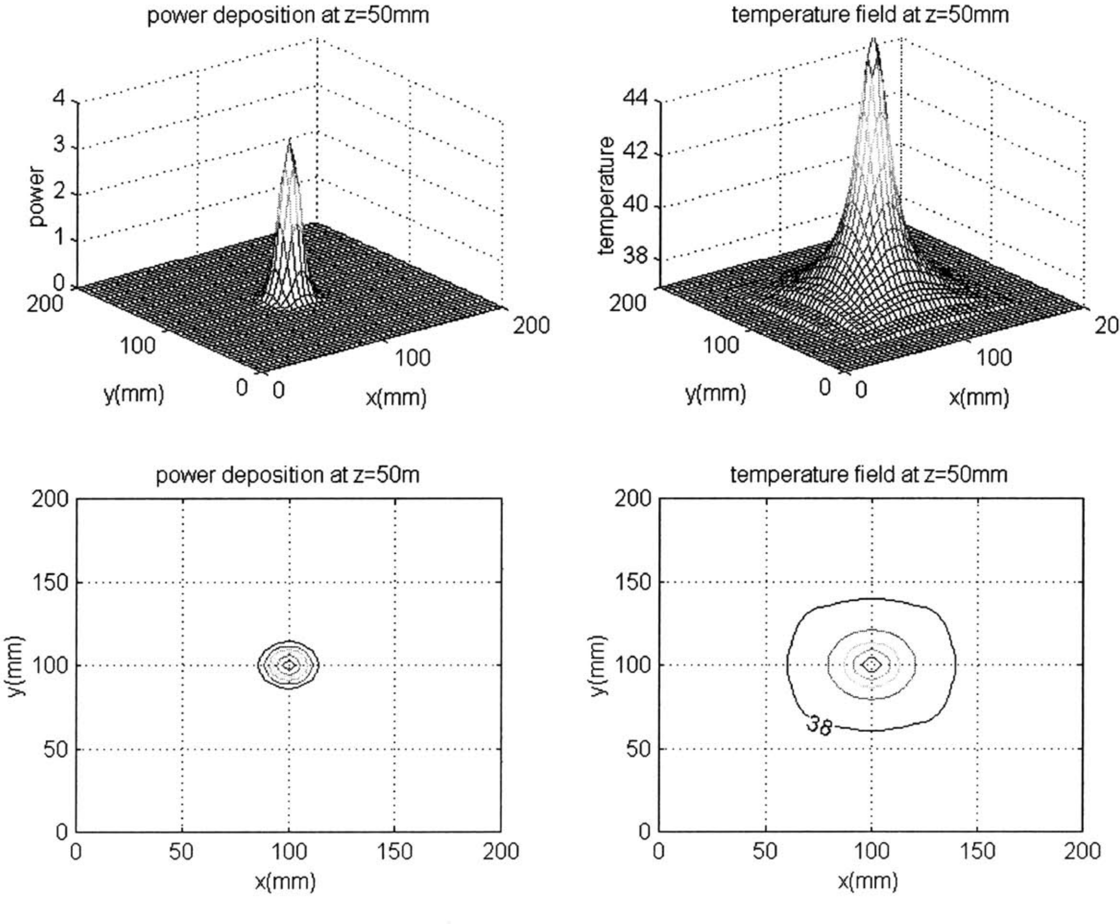

Figure 3-23 Power and temperature distribution for combined inverse thermal analysis (Ellipsoidal tumor, modified source placement, boundary plane view, Pe=0.1, RMS= 0.981°C)

3.4.6 Perfusion Effect

Perfusion has great effect on heat removal. Figure 3-24 shows the power and temperature distribution on the central plane for Pe=1.0. The source placement is similar to the previous one as showed in Figure 3-21. The root mean square error is 2.6707°C, which is really high. The figure shows that even within the tumor region, some small areas are still underheated while the small areas within the source focus are overheated. This suggests that more sources are needed for the high perfusion region.

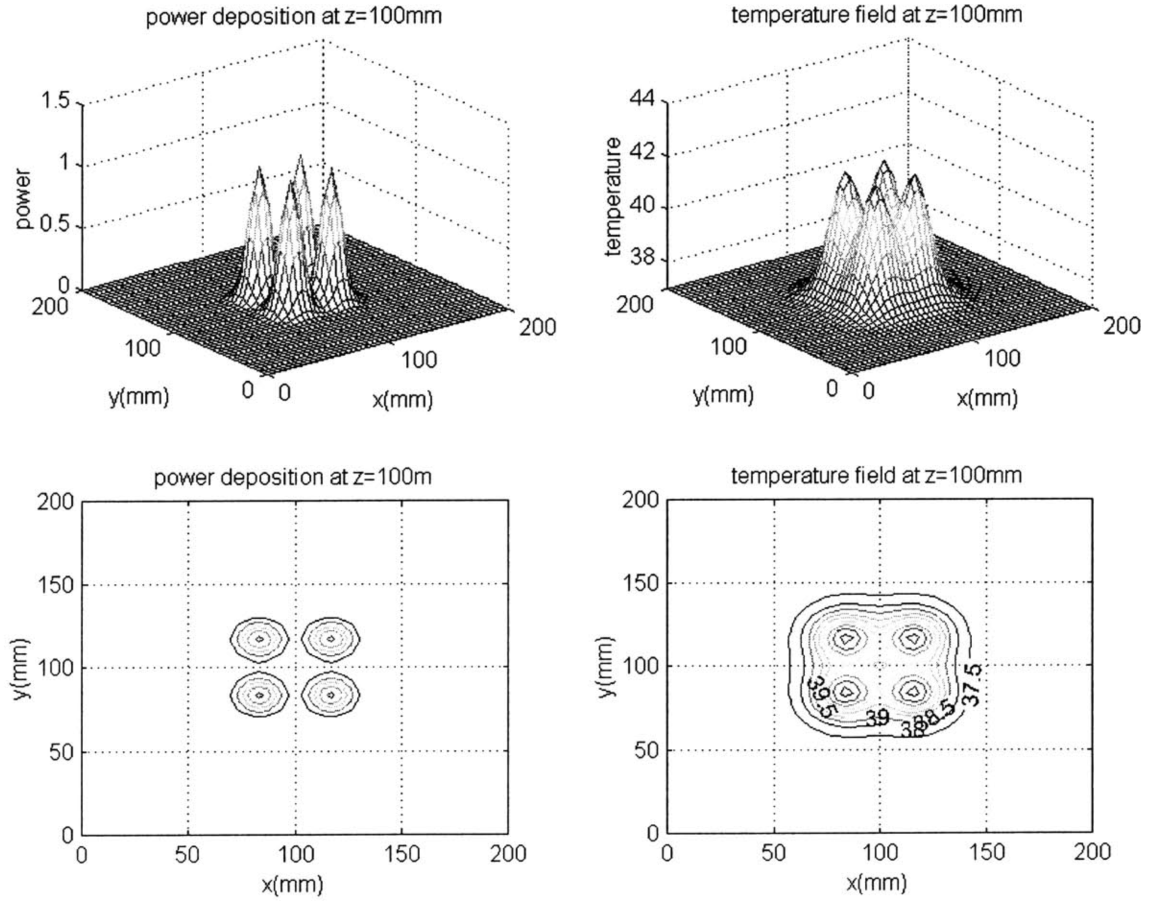

Figure 3-24 Power and temperature distribution for combined inverse thermal analysis (Ellipsoidal tumor, modified source placement, central plane view, Pe=1.0, RMS= 2.6707°C)

A dense source placement is adopted for the high perfusion region. There are 7 layers of sources in z-direction, i.e. at z=50, 66.7, 83.3, 100, 116.7, 133.3, 150 mm. The source placement for the first four layers is showed in Figure 3-25. The source placement on other layers can be obtained by symmetry. There are 39 sources in total.

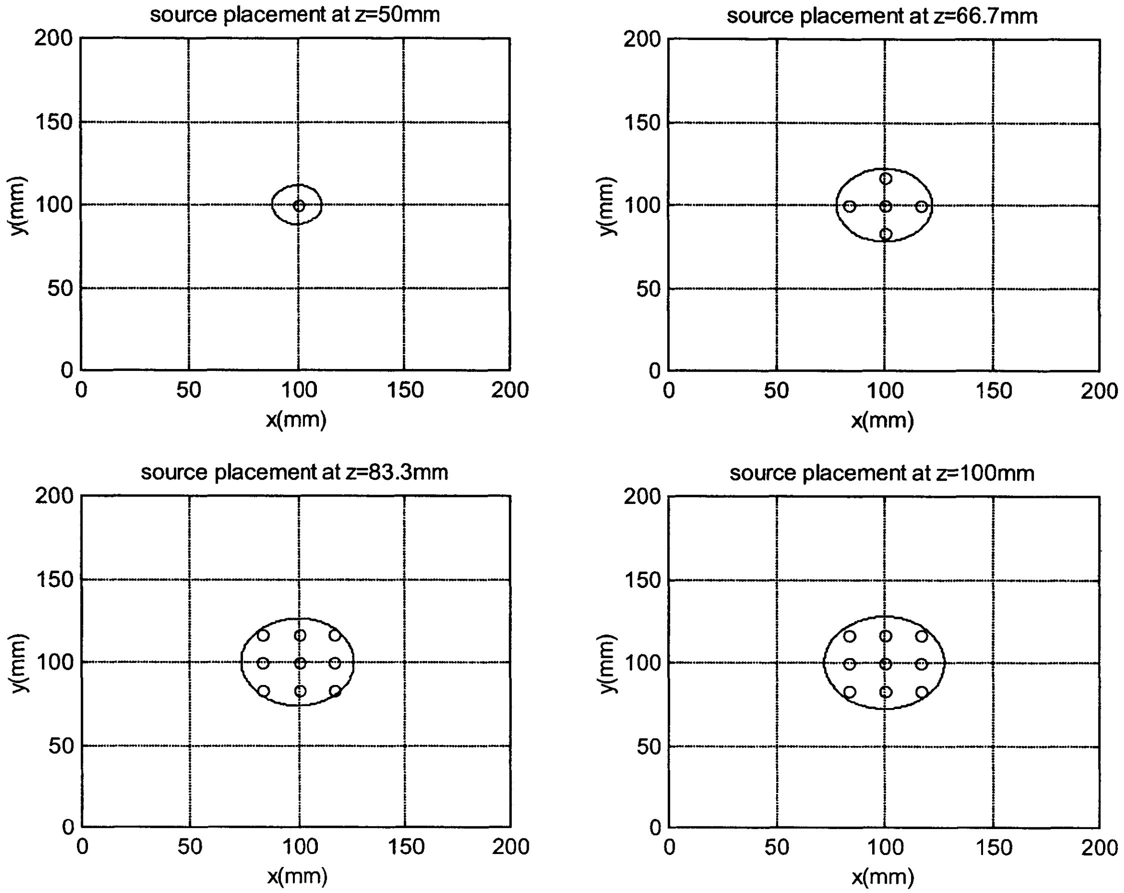

Figure 3-25 Cross-section view of dense source placement for ellipsoidal tumor (Pe= 1)

Figure 3-26 shows the central plane view of the power and temperature distribution for the ellipsoidal tumor model, dense source placement for Pe=1.0. The temperature in the tumor region is close to the optimal temperature. The root mean square is 0.8987°C, which is much less than 2.6707°C, the RMS when the regular modified source placement scheme is used. From the power plot in the left column, the sources are so close to each other such that it is hard to distinguish individual source.

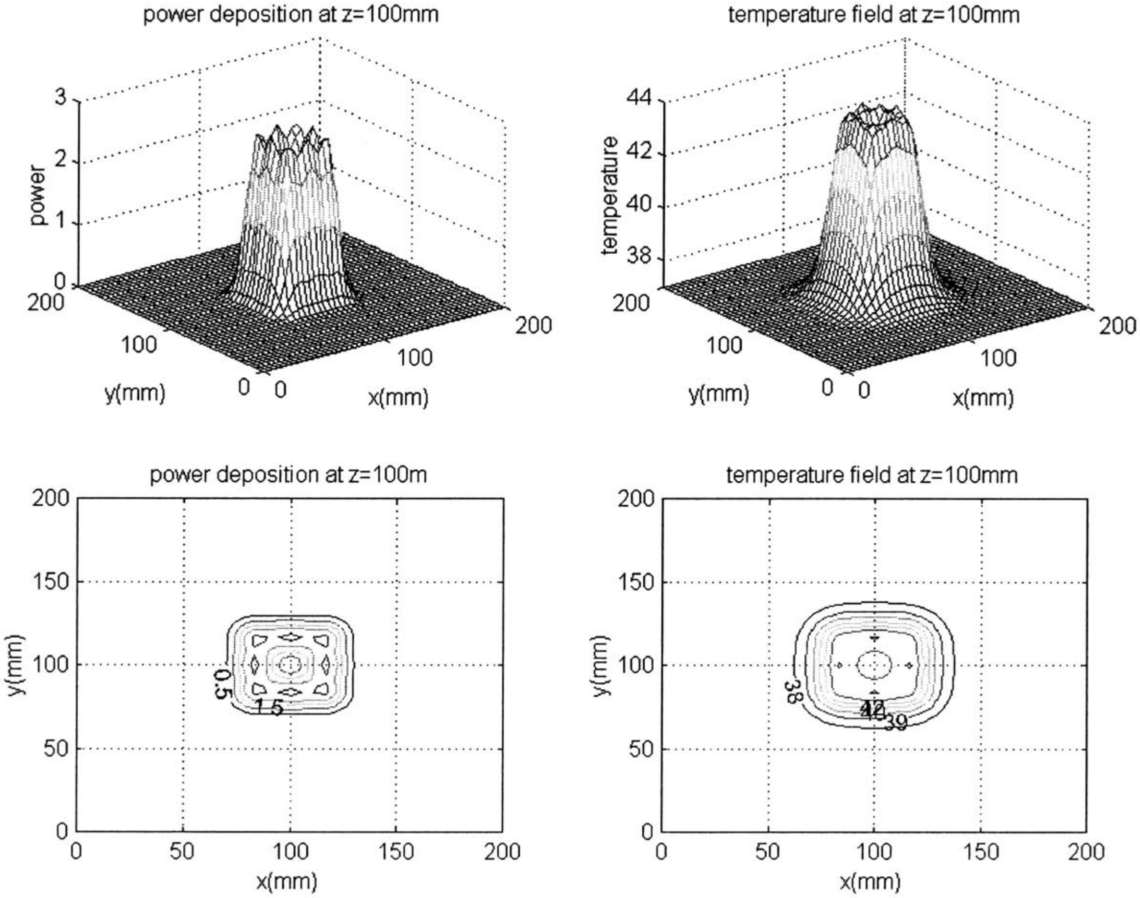

Figure 3-26 Power and temperature distribution for combined inverse thermal analysis (Ellipsoidal tumor, dense source placement, central plane view, Pe=1.0, RMS= 0.8987°C)

Figure 3-27 shows the boundary plane view of the power and temperature distribution for the ellipsoidal tumor model, dense source placement for Pe=1.0. The temperature in the tumor region is close to the optimal temperature though overheating in a small area near the source focus can be seen.

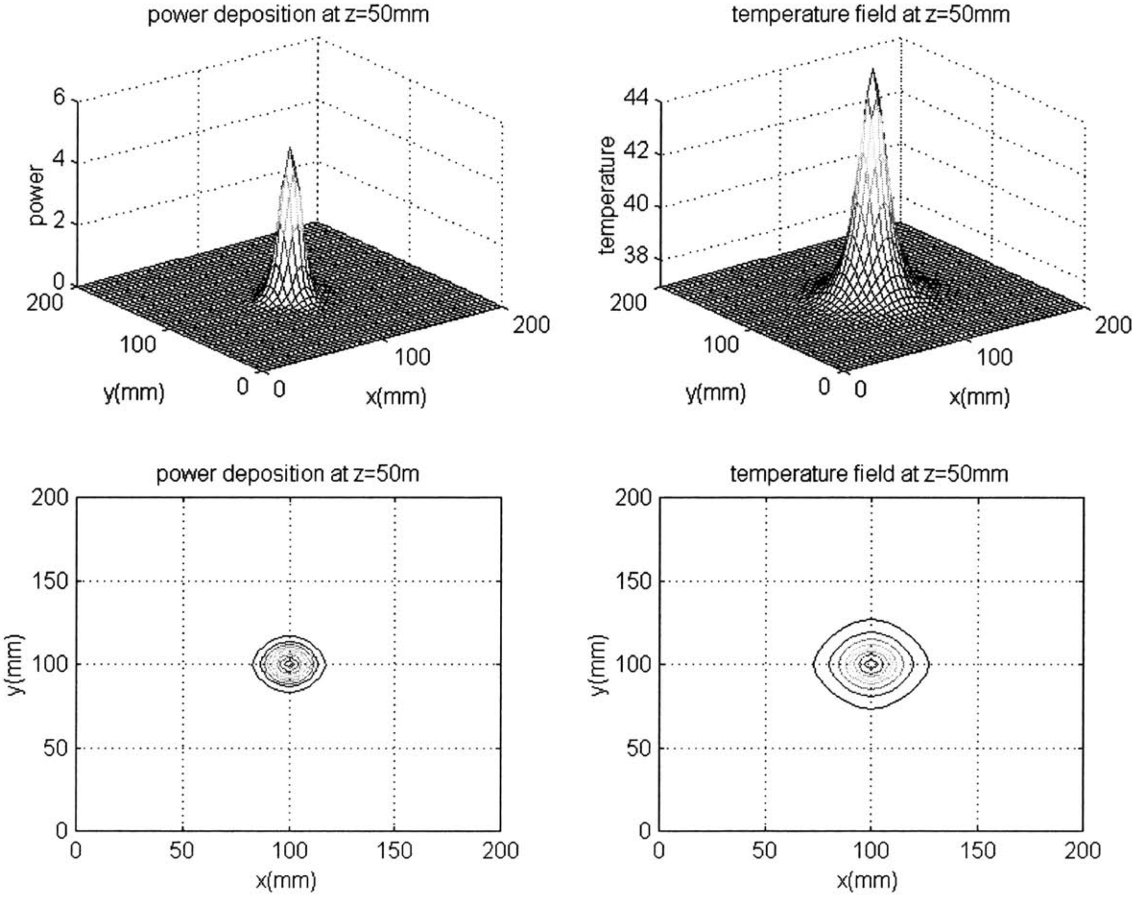

Figure 3-27 Power and temperature distribution for combined inverse thermal analysis (Ellipsoidal tumor, dense source placement, boundary plane view, Pe=1.0, RMS= 0.8987°C)

3.4.7 Discussions

The combined inverse thermal analysis has been simulated for three tumor models with various thermal properties and perfusion. The heating source is simplified as normalized source array. Although in reality this assumption is not valid for most of the energy delivery machine, the algorithm doesn't depend on a certain kind of energy delivery machine. This assumption is used to facilitate the simulation.

The simulation results show that the temperature inside the tumor region can be maintained close to optimal temperature. On the boundary between tumor and normal tissue region, the temperature is hard to maintain uniform and overheating may occur within a small volume of source focal point. This is due to the limitation of concentrated source. The analytical results show that two kinds of sources, i.e. volume distributed source and boundary surface source, can maintain a uniform temperature within the tumor region. The concentrated source in essence is distributed source. It is very difficult for an array of concentrated sources to represent the surface source unless the concentrated sources are so concentrated that they might be treated as point sources. Therefore if the concentrated level of the energy delivery machine may be adjusted, it is desirable to have high level concentrated sources be placed around the tumor boundary while low level concentrated sources be placed inside the tumor region.

Source placement method plays an important role in maintaining a uniform temperature field. The choice of source placement in the thesis is based on intuition rather than numerical optimization. Theoretically, the location of the sources can be treated as optimization variables besides the intensities of the sources. However, since the location of the sources is the function of the three-dimensional coordinates and there are multiple sources available, this procedure is much more complicated. One way to solve this problem is to compute numerically along the possible combination of sources' location, and the solution that minimizes RMS error and the required power is the optimal solution.

Perfusion is also an important factor in inverse analysis. The results show that perfusion level, together with the size and geometry of the tumor, are the major factors in determining the number of sources used in the application. Higher perfusion level requires more sources to be placed inside the tumor region. This is understandable because higher perfusion means more blood flow, more blood flow means more heat being carried out by blood flow, so it requires more energy to be deposited into the tumor region. It is interested to note that higher perfusion makes the source "look like" more concentrated since the perfusion length is shorter thus makes the effect of the source less noticeable for the same distance.

3.5 Summary of Inverse Thermal Analysis

In this chapter, the inverse thermal analysis is the sole focus of the study. A brief introduction to inverse thermal problems and a review of current progress in inverse thermal problems for clinical hyperthermia are given in the beginning of the chapter. Then the focus is on the modeling and solution method formulation for the two inverse hyperthermia thermal problems, i.e. inverse thermal analysis for desired power field and combined inverse thermal analysis, which can link the optimal temperature field to the control parameters of the energy delivery machine.

The inverse thermal analysis for desired power field is solved analytically for one-dimensional tumor model and numerically for three-dimensional cubic tumor model. The result shows that two different kinds of sources, i.e. distributed source and concentrated surface source are the ideal sources for tumor heating. The inverse algorithms for FBEM and FEM have been formulated. The numerical results from FBEM and FEM are presented and compared, as well as their speed and accuracy.

The algorithm for combined inverse thermal analysis is derived. The concept of using normalized source to represent a concentrated source and placing normalized sources into source array is introduced. The numerical simulations using normalized source array as the heating source are presented in three tumor models, i.e. the cubic tumor model, the spherical tumor model and the ellipsoidal tumor model. The simulation results show that with the judicial choice of source placement, by adjusting the strength of the individual source in the source array, the resulting temperature field is within a therapeutic temperature range. The effect of source placement and perfusion are also discussed.

Chapter 4

Transient Thermal Analysis

The ideal hyperthermia thermal management system should be able to provide therapist tools for treatment planning before the therapy, real-time temperature and power field information during the therapy, and thermal dose evaluation after the therapy. So far, our thermal models are based on steady state model suitable for therapy planning and evaluation. The transient thermal analysis, while taking whatever sparse temperature and power field measurement data, should be able to provide real-time full field temperature information during the therapy, for either manual feedback by therapist or automatic feedback control by a computer. Ideally, the complete temperature field should be provided by non-invasive thermal tomographic thermometry. However, the non-invasive temperature sensing systems, which include magnetic resonance imaging (MRI) (Zhang, 1992), electrical impedance tomography (EIT) (Blad, 1992) and microwave (Chive, 1990), are still in the early stage of development. Current hyperthermia practice depends on invasive thermometry at a limited number of selected measurement sites restricted by patient safety and comfort, which in turn can not provide all the significant information needed in a scientific experiment (Bowman, 1991).

This chapter describes the theoretical background and algorithm formulation of a fast computational method for temperature field reconstruction during hyperthermia therapy. The theoretical basis of the method is to apply Laplace transform to the transient bioheat transfer equation in order to get the "steady state" equation in complex domain, then derive the Green's function solution of the "steady state" equation in complex domain, and finally apply inverse Laplace transform to get the solution in time domain. The theory of Finite Basis Element Method

(FBEM) has been introduced in Chapter 2, as well as the steady state bioheat transfer equations in FBEM form. The focus of this chapter is on the transient analysis and the unique properties that related to the transient elements.

4.1 Theoretical Background

It is much more convenient to solve the bioheat transfer equation in dimensionless form. The dimensionless transient bioheat transfer equation is:

$$\frac{\partial T}{\partial t^+} = \nabla^{+2} T - Pe \cdot T + q^+ \tag{4.1}$$

the dimensionless parameters are defined as:

$$\begin{cases} r^+ = \dfrac{r}{a} \\ t^+ = \dfrac{\alpha_m}{a^2} t \\ Pe = \dfrac{\omega \rho_b c_b}{k_m} a^2 \\ q^+ = \dfrac{Q a^2}{k_m} \end{cases} \tag{4.2}$$

where a is the characterized length.

For transient problem, Laplace transform is used to transform the partial differential equations and boundary conditions into "steady state form" in complex domain. Applying:

$$\theta(\mathbf{r}^+, s) = \mathcal{L}\left[T(\mathbf{r}^+, t^+)\right] = \int_0^\infty T(\mathbf{r}^+, t^+) e^{-st^+} dt^+ \tag{4.3}$$

to the dimensionless bioheat transfer equation, we have:

$$\nabla^{+2}\theta - (Pe + s)\theta + \frac{q^+}{s} + T_0 = 0 \tag{4.4}$$

where T_0 is the initial temperature of the domain of interest. Similar to the procedure for the steady state, the Green's function solution for the above equation is:

$$\theta(\mathbf{r}) = \int_V \left(\frac{q^+}{s} + T_0\right) u(\mathbf{r}, \mathbf{r}_p) dV - \int_S \theta_B(s) \mathbf{n} \cdot \nabla u ds \tag{4.5}$$

The Green's function for transient problem is:

$$u(\boldsymbol{r},\boldsymbol{r}_p)=\frac{e^{-\sqrt{Pe+s}\cdot|r-r_p|}}{4\pi|\boldsymbol{r}-\boldsymbol{r}_p|} \tag{4.6}$$

The remain procedures are similar to those of steady state except that we need to apply inverse transform to get temperature in time domain.

The effects of heat sources are divided into small spherical elements in the near field and a microscopic element accounting for the effects of the sources in the far field. The irregular geometry with variable internal heat generation, the piece-wise thermal properties and perfusion, and the boundary condition (both homogeneous and non-homogeneous) will be taken in consideration while formulating the elements. For mathematical and computational simplicity, the elements are formed spheres in close hexagonal packing. The effects of the sources in the void volume are average by multiply a packing factor to all the elements.

In the following sections, various transient elements are formulated. These elements represent the geometry and thermal properties variation that commonly encountered in clinical hyperthermia therapy with applicable assumption and accuracy allowable mathematical simplification. These elements are free-space elements, including transient uniform Finite Basis Element and transient Finite Basis Element with nonzero initial temperature, bounded elements, including planar boundary element and spherical boundary element, and elements for variable thermal properties and perfusion, including internal planar boundary element and internal spherical boundary element.

4.2 Formulation of Free-Space Elements

The simplest and most important elements are free-space elements. The free-space element is used in situation where the spherical source is thermally distant from any thermal disturbance, such as external and internal boundary and variation of thermal properties and perfusion. The element can be approximated as a spherical source placed in an infinite domain with uniform thermal properties and perfusion.

4.2.1 Steady State Uniform Finite Basis Element

Before going further into solving transient problem, the derivation of steady state uniform Finite Basis Element is provided here. The problem statement is expressed in spherical coordinates as:

$$\frac{\partial^2}{\partial r^{+2}}(r^+T) - Pe \cdot r^+T = -r^+q^+ \tag{4.7}$$

Boundary conditions are:

$$\begin{cases} q^+ = 1, r^+ \le 1 \\ q^+ = 0, r^+ > 1 \end{cases} \tag{4.8}$$

The general solution for equation (4.7) is:

$$r^+T = C_1\, sinh(r^+\sqrt{Pe}) + C_2\, cosh(r^+\sqrt{Pe}) \tag{4.9}$$

For $r^+ \le 1$, the equation is non-homogeneous, the particular solution is:

$$T_p = \frac{1}{Pe} \tag{4.10}$$

The continuity requirements at $r^+ = 1$ are:

$$\begin{cases} T\big|_{r^+=1^+} = T\big|_{r^+=1^-} \\ (\frac{dT}{dr^+})\Big|_{r^+=1^+} = (\frac{dT}{dr^+})\Big|_{r^+=1^-} \end{cases} \tag{4.11}$$

The final solutions are:

$$T = \begin{cases} \frac{1}{Pe} - e^{-\sqrt{Pe}}(\frac{1}{Pe} + \frac{1}{\sqrt{Pe}}), r^+ = 0 \\ \frac{1}{Pe} - \frac{1}{r^+Pe} e^{-\sqrt{Pe}} \sinh(r^+\sqrt{Pe})(1 + \frac{1}{\sqrt{Pe}}), 0 < r^+ \le 1 \\ \frac{1}{r^+Pe} e^{-r^+\sqrt{Pe}} \left[\cosh(\sqrt{Pe}) - \frac{1}{\sqrt{Pe}} \sinh(\sqrt{Pe}) \right], r^+ > 1 \end{cases} \tag{4.12}$$

The above equations showed that the temperature is the function of Peclet number and dimensionless radius. In the region out of the unit sphere, the temperature attenuates exponentially ($e^{-r^+\sqrt{Pe}}$) over distance. Figure 4-1 shows the temperature profiles created by a unit free-space uniform finite source with different Peclet numbers. The figure shows that the source influence length of the spherical source depends on the Peclet number. The figure also shows that the larger the Peclet number, the shorter the influence length and the lower the temperature elevated. For constant characteristic length, larger peclet number means higher blood perfusion.

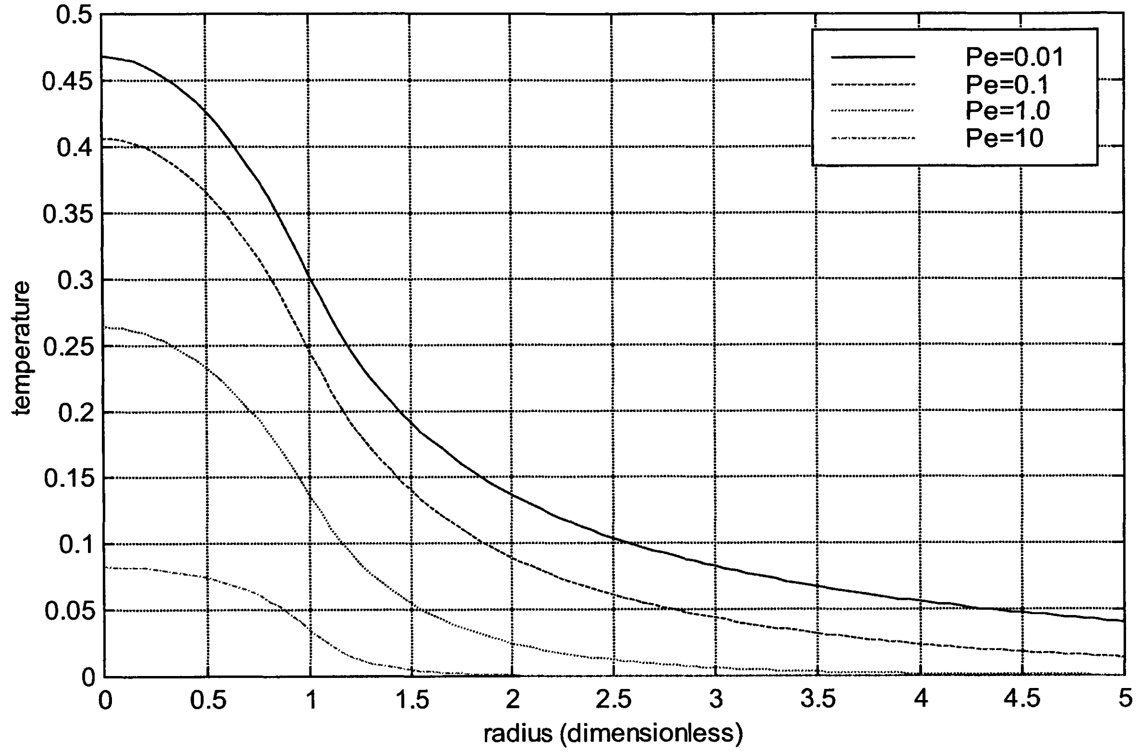

Figure 4-1 Temperature profiles created by a unit free-space uniform finite source with different Peclet numbers

4.2.2 Transient Uniform Finite Basis Element

The most important transient basis element is believed to be the transient free-space uniform finite element. The problem statement in spherical coordinates is:

$$\frac{\partial}{\partial t^{+}}(r^{+}T)=\frac{\partial^{2}}{\partial r^{+2}}(r^{+}T)-Pe\cdot(r^{+}T)+r^{+}q^{+} \qquad (4.13)$$

The initial condition is homogeneous, i.e. zero temperature initially. The heat source is only within the unit sphere. Therefore the initial and boundary conditions are:

$$\begin{cases} T = 0, t^+ \le 0 \\ q^+ = 1, r^+ \le 1 \\ q^+ = 0, r^+ > 1 \end{cases} \tag{4.14}$$

In order to solve the partial differential equation, Laplace Transform is used:

$$\theta(r^+, s) = \mathcal{L}[T(r^+, t^+)] = \int_0^\infty T(r^+, t^+) e^{-st^+} dt^+ \tag{4.15}$$

to transform the partial differential equation into ordinary differential equation:

$$\begin{cases} \frac{d^2}{dr^{+2}}(r^+\theta) - (Pe + s) \cdot r^+\theta = -\frac{r^+ q^+}{s}, r^+ \le 1 \\ \frac{d^2}{dr^{+2}}(r^+\theta) - (Pe + s) \cdot r^+\theta = 0, r^+ > 1 \end{cases} \tag{4.16}$$

The above equation is basically the same as the steady state equation except *Pe* has been replaced by *Pe*+*s*. It can be solved by the same method to yield:

$$\theta = \begin{cases} \frac{1}{s(Pe+s)} - \frac{e^{-\sqrt{Pe+s}}}{s}\left(\frac{1}{Pe+s} + \frac{1}{\sqrt{Pe+s}}\right), r^+ = 0 \\ \frac{1}{s(Pe+s)} - \frac{e^{-\sqrt{Pe+s}}}{r^+ s(Pe+s)} \sinh(r^+\sqrt{Pe+s})\left(1 + \frac{1}{\sqrt{Pe+s}}\right), 0 < r^+ \le 1 \\ \frac{e^{-r^+\sqrt{Pe+s}}}{r^+ s(Pe+s)} \left[\cosh(\sqrt{Pe+s}) - \frac{1}{\sqrt{Pe+s}} \sinh(\sqrt{Pe+s})\right], r^+ > 1 \end{cases} \tag{4.17}$$

The inverse Laplace transform gives:

$$T(r^+, t^+) = \begin{cases} \frac{1 - e^{-Pe \cdot t^+}}{Pe} + \frac{L_5(1) - L_1(1)}{Pe} - L_3(1), & r^+ = 0 \\ \frac{1 - e^{-Pe \cdot t^+}}{Pe} - \frac{1}{2r^+ Pe}[L_1(1 - r^+) - L_1(1 + r^+) - L_5(1 - r^+) + L_5(1 + r^+) & \\ \quad + L_3(1 - r^+) - L_3(1 + r^+) - L_4(1 - r^+) + L_4(1 + r^+)], & 0 < r^+ \le 1 \\ \frac{1}{2r^+ Pe}[L_1(r^+ - 1) + L_1(r^+ + 1) - L_5(r^+ - 1) - L_5(r^+ + 1) & \\ \quad - L_3(r^+ - 1) + L_3(r^+ + 1) + L_4(r^+ - 1) - L_4(r^+ + 1)], & r^+ > 1 \end{cases} \tag{4.18}$$

where

$$L_1(r^+) = L^{-1}\left(\frac{e^{-r^+\sqrt{s+Pe}}}{s}\right) = \frac{1}{2}\left[e^{-r^+\sqrt{Pe}} erfc\left(\frac{r^+}{2\sqrt{t^+}} - \sqrt{Pe \cdot t^+}\right) + e^{r^+\sqrt{Pe}} erfc\left(\frac{r^+}{2\sqrt{t^+}} + \sqrt{Pe \cdot t^+}\right)\right] \tag{4.19}$$

$$L_3(r^+) = L^{-1}[\frac{e^{-r^+\sqrt{s+Pe}}}{s\sqrt{s+Pe}}] = \frac{1}{2\sqrt{Pe}}[e^{-r^+\sqrt{Pe}}erfc(\frac{r^+}{2\sqrt{t^+}} - \sqrt{Pe\cdot t^+}) - e^{r^+\sqrt{Pe}}erfc(\frac{r^+}{2\sqrt{t^+}} + \sqrt{Pe\cdot t^+})] \tag{4.20}$$

$$L_4(r^+) = L^{-1}[\frac{e^{-r^+\sqrt{s+Pe}}}{(s+Pe)^{3/2}}] = e^{-Pe\cdot t^+}[2e^{-\frac{r^{+2}}{4t^+}}\sqrt{\frac{t^+}{\pi}} - r^+\cdot erfc(\frac{r^+}{2\sqrt{t^+}})] \tag{4.21}$$

$$L_5(r^+) = L^{-1}(\frac{e^{-r^+\sqrt{s+Pe}}}{s+Pe}) = e^{-Pe\cdot t^+}\cdot erfc(\frac{r^+}{2\sqrt{t^+}}) \tag{4.22}$$

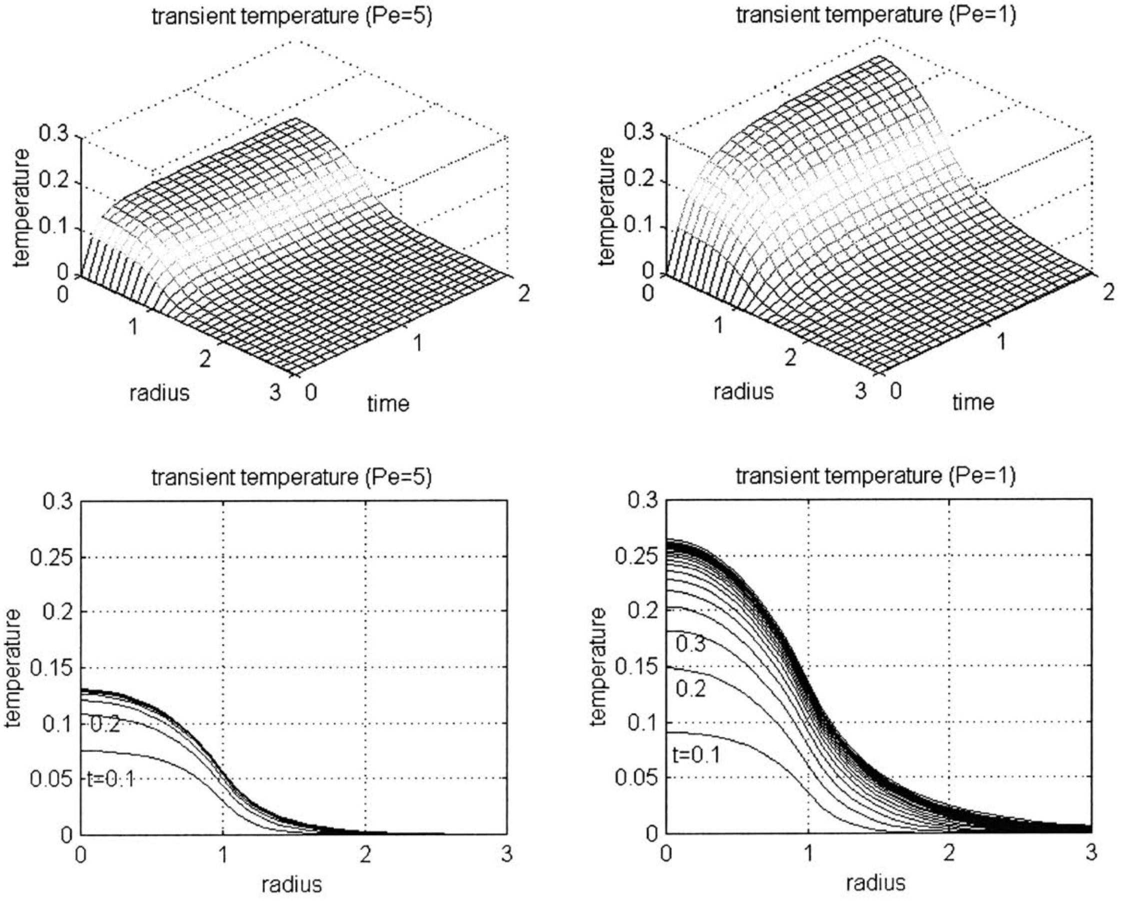

transient temperature (Pe=5)

transient temperature (Pe=1)

transient temperature (Pe=5)

transient temperature (Pe=1)

Figure 4-2 Transient temperature responses to a unit free-space uniform spherical source

The transient temperature response to a unit free-space uniform source is showed in Figure 4-2 for Peclet number of 1 and 5. The upper subplots are three-dimensional view and the lower subplots are two-dimensional view. The left column subplots are for Peclet number equals to 5 and the right column for Peclet number equals to 1. The figure shows that the larger the Peclet number, the faster it reaches the steady state.

Special Case: *Pe=0,* no perfusion

From equation (4.17), let $Pe=0$, we have:

$$\theta = \begin{cases} \dfrac{1}{s^2} - \dfrac{e^{-\sqrt{s}}}{s}\left(\dfrac{1}{s} + \dfrac{1}{\sqrt{s}}\right), r^+ = 0 \\ \dfrac{1}{s^2} - \dfrac{e^{-\sqrt{s}}}{r^+ s^2} \sinh(r^+\sqrt{s})\left(1 + \dfrac{1}{\sqrt{s}}\right), 0 < r^+ \leq 1 \\ \dfrac{e^{-r^+\sqrt{s}}}{r^+ s^2}\left[\cosh(\sqrt{s}) - \dfrac{1}{\sqrt{s}}\sinh(\sqrt{s})\right], r^+ > 1 \end{cases} \qquad (4.23)$$

For $r^+ = 0$:

$$T(r^+, t^+) = t^+\left[1 - erfc\left(\frac{1}{2\sqrt{t^+}}\right)\right] + \frac{1}{2} erfc\left(\frac{1}{2\sqrt{t^+}}\right) - \sqrt{\frac{t^+}{\pi}} e^{-\frac{1}{4t^+}} \qquad (4.24)$$

For $0 < r^+ \leq 1$:

$$\begin{aligned} T(r^+, t^+) = \frac{t^+}{r^+}\Bigg[& r^+ - 2i^2 erfc\left(\frac{1-r^+}{2\sqrt{t^+}}\right) + 2i^2 erfc\left(\frac{1+r^+}{2\sqrt{t^+}}\right) - \\ & - 4\sqrt{t^+} \cdot i^3 erfc\left(\frac{1-r^+}{2\sqrt{t^+}}\right) + 4\sqrt{t^+} \cdot i^3 erfc\left(\frac{1+r^+}{2\sqrt{t^+}}\right)\Bigg] \end{aligned} \qquad (4.25)$$

For $r^+ > 1$:

$$\begin{aligned} T(r^+, t^+) = \frac{2t^+}{r^+}\Bigg[& i^2 erfc\left(\frac{r^+ - 1}{2\sqrt{t^+}}\right) + i^2 erfc\left(\frac{r^+ + 1}{2\sqrt{t^+}}\right) \\ & - 2\sqrt{t^+} \cdot i^3 erfc\left(\frac{r^+ - 1}{2\sqrt{t^+}}\right) + 2\sqrt{t^+} \cdot i^3 erfc\left(\frac{r^+ + 1}{2\sqrt{t^+}}\right)\Bigg] \end{aligned} \qquad (4.26)$$

Where

$$\begin{cases} i^0 erfc(x) = erfc(x) \\ ierfc(x) = \frac{1}{\sqrt{\pi}} e^{-x^2} - x \cdot erfc(x) \\ i^n erfc(x) = \frac{1}{2n}\left[i^{n-2} erfc(x) - 2x \cdot i^{n-1} erfc(x) \right], n \geq 2 \end{cases} \tag{4.27}$$

4.2.3 Transient Finite Basis Element with Nonzero Initial Temperature

Another important free-space finite basis element is the effect of initial non-zero temperature. The problem statement in the spherical coordinates is:

$$\frac{\partial}{\partial t^+}(r^+T) = \frac{\partial^2}{\partial r^{+2}}(r^+T) - Pe \cdot (r^+T) \tag{4.28}$$

Note that there is no internal heat generation in the equation. The initial conditions at *t=0* are:

$$\begin{cases} T = 1, r^+ \leq 1 \\ T = 0, r^+ > 1 \end{cases} \tag{4.29}$$

Applying Laplace transform to the above equations, we have:

$$\begin{cases} \frac{d^2}{dr^{+2}}(r^+\theta) - (Pe + s) \cdot r^+\theta + r^+ = 0, r^+ \leq 1 \\ \frac{d^2}{dr^{+2}}(r^+\theta) - (Pe + s) \cdot r^+\theta = 0, r^+ > 1 \end{cases} \tag{4.30}$$

The solution for the above equations is:

$$\theta = \begin{cases} \frac{1}{Pe+s} - \frac{e^{-\sqrt{Pe+s}}}{\sqrt{Pe+s}}(1 + \frac{1}{\sqrt{Pe+s}}), r^+ = 0 \\ \frac{1}{Pe+s} - \frac{e^{-\sqrt{Pe+s}}}{r^+(Pe+s)}(1 + \frac{1}{\sqrt{Pe+s}}) sinh(r^+\sqrt{Pe+s}), 0 < r^+ \leq 1 \\ \frac{e^{-r^+\sqrt{Pe+s}}}{r^+(Pe+s)}[cosh(\sqrt{Pe+s}) - \frac{1}{\sqrt{Pe+s}} sinh(\sqrt{Pe+s})], r^+ > 1 \end{cases} \tag{4.31}$$

The inverse Laplace transform gives the temperature as:

$$T(r^+,t^+)=\begin{cases} e^{-Pe\cdot t^+}-\dfrac{1}{\sqrt{\pi t^+}}e^{-(Pe\cdot t^+ +\frac{1}{4t^+})}-L_5(1), r^+=0 \\ e^{-Pe\cdot t^+}-\dfrac{1}{2r^+}[L_5(1-r^+)-L_5(1+r^+)+L_4(1-r^+)-L_4(1+r^+)], 0<r^+\le 1 \\ \dfrac{1}{2r^+}[L_5(r^+-1)+L_5(r^+ +1)-L_4(r^+-1)+L_4(r^+ +1)], r^+>1 \end{cases}$$

(4.32)

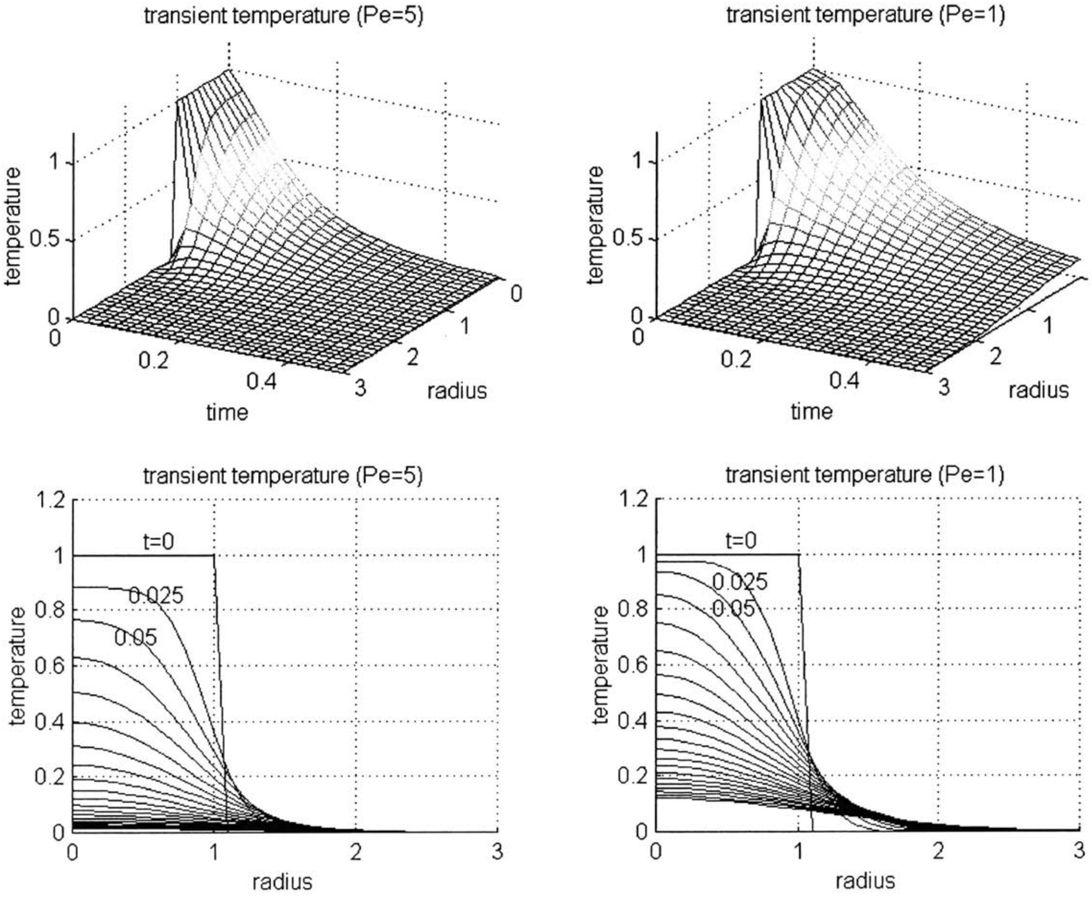

Figure 4-3 Transient temperature responses to unit sphere with non-zero initial temperature

Figure 4-3 shows the transient temperature responses to unit sphere with nonzero initial temperature for Peclet number of 1 and 5. The upper subplots are three-dimensional view and the lower subplots are two-dimensional view. The left column subplots are for Peclet number equals to 5 and the right column for Peclet number equals to 1. The figure shows that temperature attenuates rapidly inside and outside of the unit sphere. The attenuate speed depends on the Peclet number, the larger the Peclet number, the faster the temperature goes to zero.

4.3 Formulation of Bounded Elements

The free-space transient finite basis element is no longer valid whenever there is a boundary near the point of interest. Special bounded transient finite basis elements are needed to take into account the effect of various boundary conditions.

Considering the linearity of the bioheat transfer equation, the general solution for non-homogeneous boundary conditions can be obtained by the method of superposition. Each of the components of superposition can be simplified to contain only one non-homogeneous part either in the equation or part of the boundary. The problem statement can be generalized as:

$$\left.\begin{array}{ll} \Omega: & \dfrac{\partial T}{\partial t^{+}} = \nabla^{+2} T - Pe \cdot T + q^{+} \\ S: & \dfrac{\partial T}{\partial n} + Bi \cdot T = f_b \\ \tau: & T = T_0 \end{array}\right\} \quad (4.33)$$

Applying Laplace transform, we have a transformed problem statement as:

$$\left.\begin{array}{ll} \Omega: & \nabla^{+2}\theta - (Pe+s)\theta + \dfrac{q^{+}}{s} + T_0 = 0 \\ S: & \dfrac{\partial \theta}{\partial n} + Bi \cdot \theta = \int_0^{\infty} f_b e^{-st^{+}} dt^{+} \end{array}\right\} \quad (4.34)$$

The above transformed bioheat transfer equation has two non-homogeneous parts in the equation. The first one is the power deposition q^{+} and the second is the effect of nonzero initial temperature T_0. There might be several kinds of non-homogeneous boundary conditions. Decompose all the non-homogeneous pieces into several cases such that in each case there is only one piece of non-homogeneous component left. Then each case can be solved separately and the temperature is the superposition of all the cases. The decomposing process can be showed in the following:

$$\left.\begin{aligned} \Omega_1: &\quad \nabla^{+2}\theta_1 - (Pe+s)\theta_1 + \frac{q^+}{s} = 0 \\ S_1: &\quad \frac{\partial \theta_1}{\partial n} + Bi\cdot\theta_1 = 0 \end{aligned}\right\} \tag{4.35}$$

$$\left.\begin{aligned} \Omega_2: &\quad \nabla^{+2}\theta_2 - (Pe+s)\theta_2 + T_0 = 0 \\ S_2: &\quad \frac{\partial \theta_2}{\partial n} + Bi\cdot\theta_2 = 0 \end{aligned}\right\} \tag{4.36}$$

$$\left.\begin{aligned} \Omega_3: &\quad \nabla^{+2}\theta_3 - (Pe+s)\theta_3 = 0 \\ S_3: &\quad \frac{\partial \theta_3}{\partial n} + Bi\cdot\theta_3 = \int_0^\infty f_{b1} e^{-st^+}\,dt^+ \end{aligned}\right\} \tag{4.37}$$

• • •   • • •

For simplicity, the boundaries can be approximated as either piece-wise planar or spherical surfaces. The derivation of boundary elements is obtained by a convolution volume integration of the appropriate Green's function over the finite source distribution. However, if the close form of the integration is not readily available, a simplified approximation method will be used. The idea of the approximation is to applying a matching function, which representing a source located somewhere in the region, in order to maintain the required boundary condition on the boundaries.

4.3.1 Planar Boundary Element

Homogeneous boundary condition

When there is a planar homogeneous boundary near a source, the effect of homogeneous boundary condition might be computed by the superposition of a free-space Green's function and a matching function to maintain homogenous boundary condition. Supposed that the planar boundary is at $y=0$. The source is located at $(0,-y_p,0)$ as shown in Figure 4-4. The original Green's function and the matching function in open form is given as:

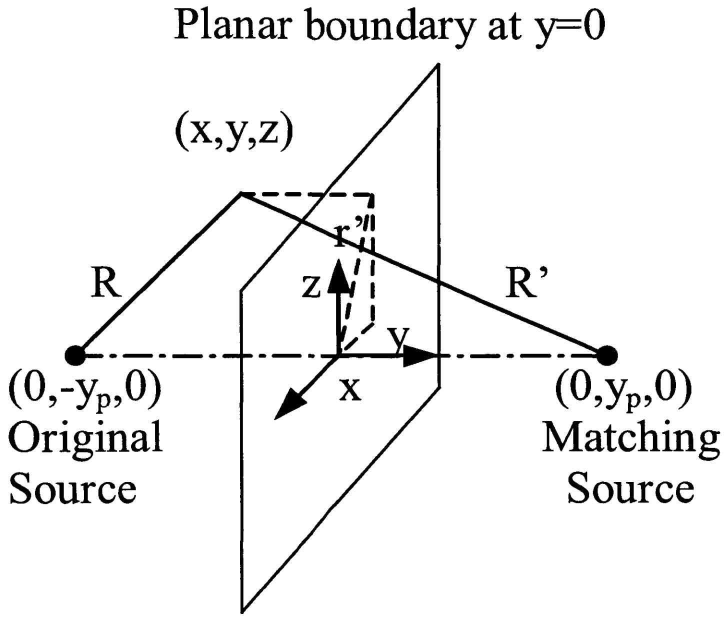

Figure 4-4 Schematic diagram of planar boundary for transient basis element

$$u = \frac{e^{-R\sqrt{Pe+s}}}{4\pi R} + \frac{1}{4\pi}\int_0^\infty Ae^{-\upsilon|y-y_p|}\frac{J_0(\eta r')}{\upsilon}\eta d\eta \tag{4.38}$$

Where:

$$\begin{cases} R = \sqrt{x^2 + (y+y_p)^2 + z^2} \\ \upsilon = \sqrt{\eta^2 + Pe + s} \\ r' = \sqrt{x^2 + z^2} \end{cases} \tag{4.39}$$

and $J_0(z)$ is the zeroth order Bessel function of the first kind. A is the Fourier-Bessel coefficient, which is found depending on the type of boundary condition.

It is very difficult to get a closed form Green's function expression by direct integration. From observation, we know that if there exists a single matching source, it will be located at $(0,y_p,0)$ with unknown strength of A, which can be solved by plug in the boundary condition. For any point (x,y,z) near the boundary, the Green's function is the superposition of the effect from original source and mirror source:

$$u = \frac{e^{-R\sqrt{Pe+s}}}{4\pi R} + A\frac{e^{-R'\sqrt{Pe+s}}}{4\pi R'} \tag{4.40}$$

where:

$$R' = x^2 + (y - y_p)^2 + z^2 \tag{4.41}$$

For the first kind homogeneous boundary condition *T=0,* plug in the boundary condition, at *y=0, T=0,* into the above equations, we have $A = -1$.

For the second kind homogeneous boundary condition $\frac{\partial T}{\partial y} = 0$, we have $A=1$.

For the third kind homogeneous boundary condition $\frac{\partial T}{\partial y} = Bi \cdot T$, the single mirror source cannot compensate all the effects of the original source. As an approximation, the strength of the mirror is:

$$A = \frac{\frac{y_p}{r'}(\sqrt{Pe} + \frac{a}{r'}) - Bi}{\frac{y_p}{r'}(\sqrt{Pe} + \frac{a}{r'}) + Bi} \tag{4.42}$$

Non-homogeneous boundary conditions

It is very difficult to find the exact solution for non-homogeneous boundary condition. The temperature component can be calculated from one-dimensional approximation of an infinite planar boundary:

$$\Omega: \quad \frac{\partial T(y^+, t^+)}{\partial t^+} = \frac{\partial^2}{\partial y^{+2}} T(y^+, t^+) - Pe \cdot T(y^+, t^+) \tag{4.43}$$

This equation may be solved by the method of Laplace transform. For the boundary condition of the first kind, $T=T_b$ at $y^+=0$, the solution is:

$$T(y^+, t^+) = T_b L_1(y^+) \tag{4.44}$$

For the second kind boundary condition $\frac{\partial T}{\partial y^+} = q_b$ at $y^+=0$, we have:

$$T(y^+, t^+) = -q_b L_3(y^+) \tag{4.45}$$

For the third kind boundary condition $\frac{\partial T}{\partial y^+} + Bi \cdot T = q_b$, we have:

$$T(y^+,t^+) = -\frac{1}{2}q_b Pe\cdot t^+[\frac{1}{\sqrt{Pe}-Bi}e^{-y^+\sqrt{Pe}}erfc(\frac{y^+}{2\sqrt{t^+}}-\sqrt{Pe\cdot t^+})-\frac{1}{\sqrt{Pe}+Bi}e^{y^+\sqrt{Pe}}$$
$$erfc(\frac{y^+}{2\sqrt{t^+}}+\sqrt{Pe\cdot t^+})]+\frac{Bi}{Bi^2-Pe}e^{-Bi\cdot y^+ + Bi^2 t^+}erfc(\frac{y^+}{2\sqrt{t^+}}-Bi\sqrt{t^+}) \tag{4.46}$$

4.3.2 Spherical Boundary Element

Boundaries between tumor and normal tissue are curved and highly irregular. These kinds of boundaries can be approximated as locally spherical boundaries. It is desirable to develop transient Basis Element that can deal with spherical boundary condition. We follow the similar procedures used in the previous section, i.e. we use Laplace transform to get "steady state" equations, solve the equations, then convert the results into time domain by inverse Laplace transform.

Homogeneous boundary condition

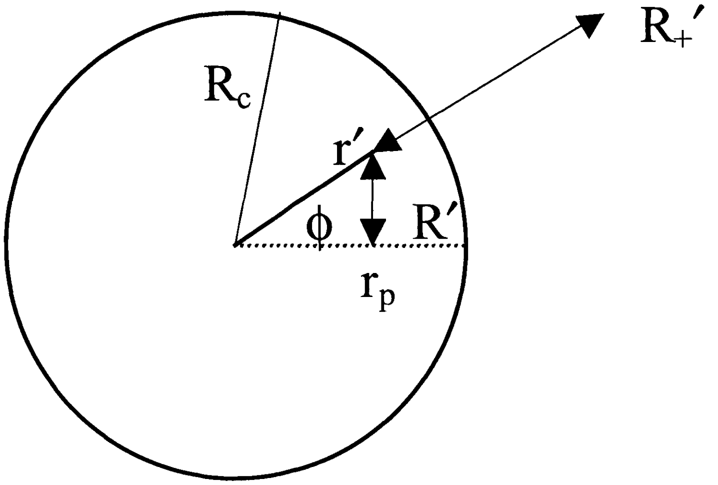

Figure 4-5 Schematic diagram of spherical boundary for transient basis element

Figure 4-5 shows a schematic diagram of the spherical boundary. Suppose a point source is at $(r_p, 0, 0)$ of the spherical polar coordinates. The point of interest is at $(r', \phi, 0)$. We can rotate the coordinates system to make the third coordinate become zero. Carslaw and Jaeger (1959 page 381) gave the solution in infinite series form for first kind boundary condition as:

$$u = \frac{e^{-R'\sqrt{Pe+s}}}{4\pi R'} - \frac{1}{4\pi\sqrt{r'r_p}}\sum_{n=0}^{\infty} A_n P_n(\mu) I_{n+\frac{1}{2}}(r'\sqrt{Pe+s}) \tag{4.47}$$

where

$$\mu = \cos\phi \tag{4.48}$$

$$R' = \sqrt{r'^2 + r_p^2 - 2r'r_p\cos\phi} \tag{4.49}$$

$I_{n+\frac{1}{2}}(z)$ is the modified Bessel function of the first kind and $P_n(\mu)$ is the Legendre polynomials of the first kind. The coefficients A_n are determined by the boundary condition. The simplest first kind boundary condition is zero temperature on the boundary. Other non-zero temperature can be modified to zero temperature by adjusting baseline temperature. The Green's function for the zero temperature on the spherical boundary condition is:

$$u = \frac{e^{-R'\sqrt{Pe+s}}}{4\pi R'} - \frac{1}{4\pi\sqrt{r'r_p}}\sum_{n=0}^{\infty}(2n+1)P_n(\mu)K_{n+\frac{1}{2}}(R_c\sqrt{Pe+s})I_{n+\frac{1}{2}}(r'\sqrt{Pe+s})\frac{I_{n+\frac{1}{2}}(r_p\sqrt{Pe+s})}{I_{n+\frac{1}{2}}(R_c\sqrt{Pe+s})}$$

(4.50)

where $K_{n+\frac{1}{2}}(z)$ is a modified Bessel function of the second kind and R_c is radius curvature of the surface.

The solution is in open form (infinite series). It is desirable to simplify it into a closed form. Martin (1995) derived the approximation:

$$\frac{I_{n+\frac{1}{2}}(z_1)I_{n+\frac{1}{2}}(z_2)}{I_{n+\frac{1}{2}}(z_3)} \approx I_{n+\frac{1}{2}}\left(\frac{z_1 z_2}{z_3}\right) \tag{4.51}$$

which is valid in the following cases: (1) z_1 and z_2 is a small number; (2) z_1 is close to z_3; (3) z_3 is close to z_2. Note that:

$$\frac{e^{-R'\sqrt{Pe+s}}}{R'} = \sum_{n=0}^{\infty}(2n+1)P_n(\mu)K_{n+\frac{1}{2}}(r'\sqrt{Pe+s})I_{n+\frac{1}{2}}(r_p\sqrt{Pe+s}) \tag{4.52}$$

where r′ > r_p, otherwise r′ and r_p are interchanged. Thus the approximate Green's function is:

$$u \approx \frac{e^{-R'\sqrt{Pe+s}}}{4\pi R'} - \frac{e^{-R'_+\sqrt{Pe+s}}}{4\pi R'_+} \tag{4.53}$$

$$R'^2_+ = R_c^2 + (\frac{r' r_p}{R_c})^2 - 2r' r_p \cos(\phi) \tag{4.54}$$

The Green's function for the second kind boundary condition differs from equation (4.53) by only a sign change:

$$u \approx \frac{e^{-R'\sqrt{Pe+s}}}{4\pi R'} + \frac{e^{-R'_+\sqrt{Pe+s}}}{4\pi R'_+} \tag{4.55}$$

Non-homogeneous boundary conditions

The equation for non-homogeneous boundary condition is:

$$\frac{\partial}{\partial t^+}(r^+ T) = \frac{\partial^2}{\partial r^{+2}}(r^+ T) - Pe \cdot (r^+ T) \tag{4.56}$$

The Laplace transform equation is:

$$\frac{d^2}{dr^{+2}}(r^+\theta) = (s + Pe)\cdot(r^+\theta) \tag{4.57}$$

The general solution after using symmetry condition is:

$$r^+\theta = C\sinh(r^+\sqrt{s+Pe}) \tag{4.58}$$

The boundary condition of the first kind is $T=T_b$ at $r^+=R_b$. In the complex domain, the boundary condition is $\theta = T_b/s$. Applying the boundary condition to the above equation, we have:

$$\theta = \frac{R_b T_b}{s r^+}\frac{\sinh(r^+\sqrt{s+Pe})}{\sinh(R_b\sqrt{s+Pe})} \tag{4.59}$$

This equation can be expanded in a series by the binomial theorem, thus:

$$\theta = \frac{R_b T_b}{r^+}\sum_{n=0}^{\infty}\frac{1}{s}\left\{e^{-\sqrt{s+Pe}\left[(2n+1)R_b - r^+\right]} - e^{-\sqrt{s+Pe}\left[(2n+1)R_b + r^+\right]}\right\} \tag{4.60}$$

The solutions in temperature domain is:

$$T = \frac{R_b T_b}{r^+}\sum_{n=0}^{\infty}\left\{L_1\left[(2n+1)R_b - r^+\right] - L_1\left[(2n+1)R_b + r^+\right]\right\} \tag{4.61}$$

4.4 Formulation for Variable Thermal Properties and Perfusion

In the Finite Basis Element model, the differentiation of the thermal properties and perfusion are treated as piecewise variation in the domain while homogeneous within an element. Figure 4-6 shows the schematic diagram of a domain with variable thermal properties and perfusion. The domain can be divided into continuous zones and transition zone. In the continuous zones, the free-space element model can be used. In the transition zone, the special internal boundary elements are needed. The boundary is approximated piece-wisely as either planar or spherical.

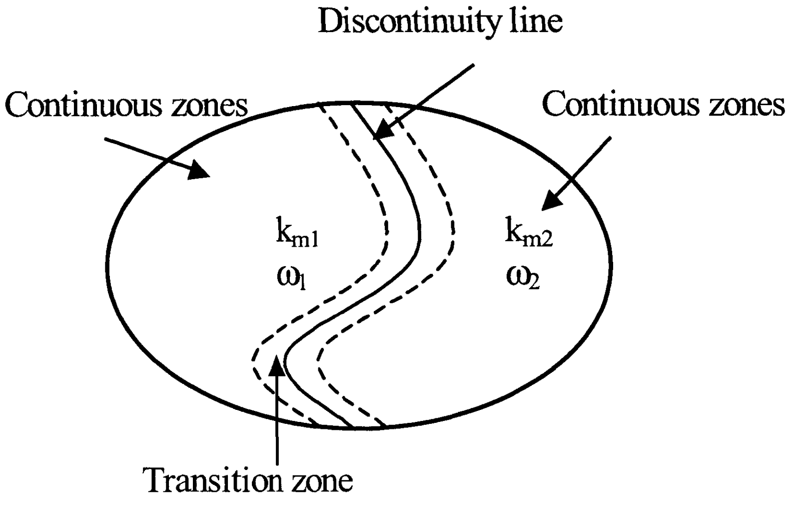

Figure 4-6 Schematic diagram of a domain with variable thermal properties and perfusion

4.4.1 Planar Internal Boundary Element

Martin (1995) has developed a close form approximation, which is based on the open form solution of Carslaw and Jaeger (1959, page 275), for the two regions with different thermal properties and perfusion separated by planar boundary. In order to be able to perform inverse

Laplace transform, we assume that the source strength is constant with respect to time. Thus the approximate solution for the Green's function in subdomain 1 is:

$$u_1 \approx \frac{e^{-R'\sqrt{\lambda_1^2+\frac{s}{\alpha_{m1}}}}}{4\pi R'} + \frac{e^{-R'_+\sqrt{\lambda_1^2+\frac{s}{\alpha_{m1}}}}}{4\pi R'_+}\left[\frac{\lambda_1\kappa r' + \kappa - \lambda_2 r' - 1}{\lambda_1\kappa r' + \kappa + \lambda_2 r' + 1}\right] \qquad (4.62)$$

and in subdomain 2 is:

$$u_2 \approx \frac{e^{-R'\sqrt{\lambda_2^2+\frac{s}{\alpha_{m2}}}}}{4\pi R'}\kappa e^{-r'(\lambda_1-\lambda_2)}\left[1+\frac{\lambda_1\kappa r' + \kappa - \lambda_2 r' - 1}{\lambda_1\kappa r' + \kappa + \lambda_2 r' + 1}\right] \qquad (4.63)$$

where

$$\begin{cases} R' = \sqrt{x^2+(y+y_p)^2+z^2} \\ R'_+ = \sqrt{x^2+(y-y_p)^2+z^2} \\ r' = \sqrt{x^2+z^2} \\ \kappa = k_{m2}/k_{m1} \end{cases} \qquad (4.64)$$

4.4.2 Spherical Internal Boundary Element

Martin (1995) has developed a close form approximation, which is based on the open form solution of Carslaw and Jaeger (1959, page 381), for the two regions with different thermal properties and perfusion separated by spherical boundary. In order to be able to perform inverse Laplace transform, we assume that the source strength is constant with respect to time. Thus the approximate solution for the Green's function in subdomain 1 is:

$$u_1 \approx \frac{e^{-R'\sqrt{\lambda_1^2+\frac{s}{\alpha_{m1}}}}}{4\pi R'} - \frac{e^{-R'_+\sqrt{\lambda_1^2+\frac{s}{\alpha_{m1}}}}}{4\pi R'_+}\left[\frac{1+\dfrac{1}{\lambda_1 R_c}-\dfrac{1}{\kappa}-\dfrac{1}{\kappa\lambda_2 R_c}}{1+\dfrac{1}{\lambda_1 R_c}+\dfrac{1}{\kappa}+\dfrac{1}{\kappa\lambda_2 R_c}}\right] \qquad (4.65)$$

and in subdomain 2 is:

$$u_2 \approx \frac{e^{-R'\sqrt{\lambda_2^2+\frac{s}{\alpha_{m2}}}}}{4\pi R'}\frac{e^{-R'_+(\lambda_1-\lambda_2)}}{\kappa}\left[1-\frac{1+\dfrac{1}{\lambda_1 R_c}-\dfrac{1}{\kappa}-\dfrac{1}{\kappa\lambda_2 R_c}}{1+\dfrac{1}{\lambda_1 R_c}+\dfrac{1}{\kappa}+\dfrac{1}{\kappa\lambda_2 R_c}}\right] \qquad (4.66)$$

where

$$\begin{cases} R' = \sqrt{r'^2 + r_p^2 - 2r'r_p \cos\phi} \\ R'_+ = \sqrt{R_c^2 + (\frac{r'r_p}{R_c})^2 - 2r'r_p \cos(\phi)} \end{cases} \tag{4.67}$$

The geometry is showed in Figure 4-5.

4.5 Validation

Martin (1995) has validated the steady state Finite Basis Element Method (FBEM) analytically, numerically and experimentally. Therefore while demonstrating the validity of the transient FBEM, the focus of the validation is on the computational properties associated with the transient problems. The transient algorithm is validated by the comparison of a series test problems, where either analytical solutions or numerical solutions from other standard method, such as Finite Element Method (FEM), exist. The problems in which the exact analytical solutions exist are generally related to simple geometry and uniform thermal properties and blood perfusion. For complex geometry or non-uniform perfusion the comparison is made from Finite Element Method (FEM). The thermal properties and perfusion data used in the validation are listed in Table 3-1, except those specified in each test case.

4.5.1 Infinite Domain with Uniform Properties

Uniform Internal Heat Generation

This is the simplest test case. It resembles the start of the heating process in hyperthermia therapy. The uniform and homogeneous properties reduce the problem to only one variable in the differential equation. The problem statement is:

$$\frac{dT}{dt^+} = -Pe \cdot T + q^+ \tag{4.68}$$

The initial conditions are

$$\begin{cases} T = 0, t^+ \le 0 \\ q^+ = 1, t^+ > 0 \end{cases} \tag{4.69}$$

The analytical solution is:

$$T(t^+) = \frac{q^+}{Pe}(1 - e^{-Pe \cdot t^+}) \tag{4.70}$$

Figure 4-7 shows the temperature profile for an infinite domain with uniform heat generation and homogeneous initial condition. The perfusion length is 7.75mm in the test case. The clinical perfusion rate is W=11.98 *(ml/min-100g)*. The power strength is $Q=10^5$ *(W/m³)*. The radius of the elements is fixed at one-third of the perfusion length, i.e. 2.58mm. The integration lengths are different, i.e. twice, four times and six times of the perfusion length, i.e. 15.5mm, 31.0mm and 46.5mm respectively. The analytical solution is drawn in solid line and the numerical results are shown in circles and triangles. The agreement of the computational results to the analytical ones is good except for large time increment the disparity becomes obvious for low integration volume (N_p=2)

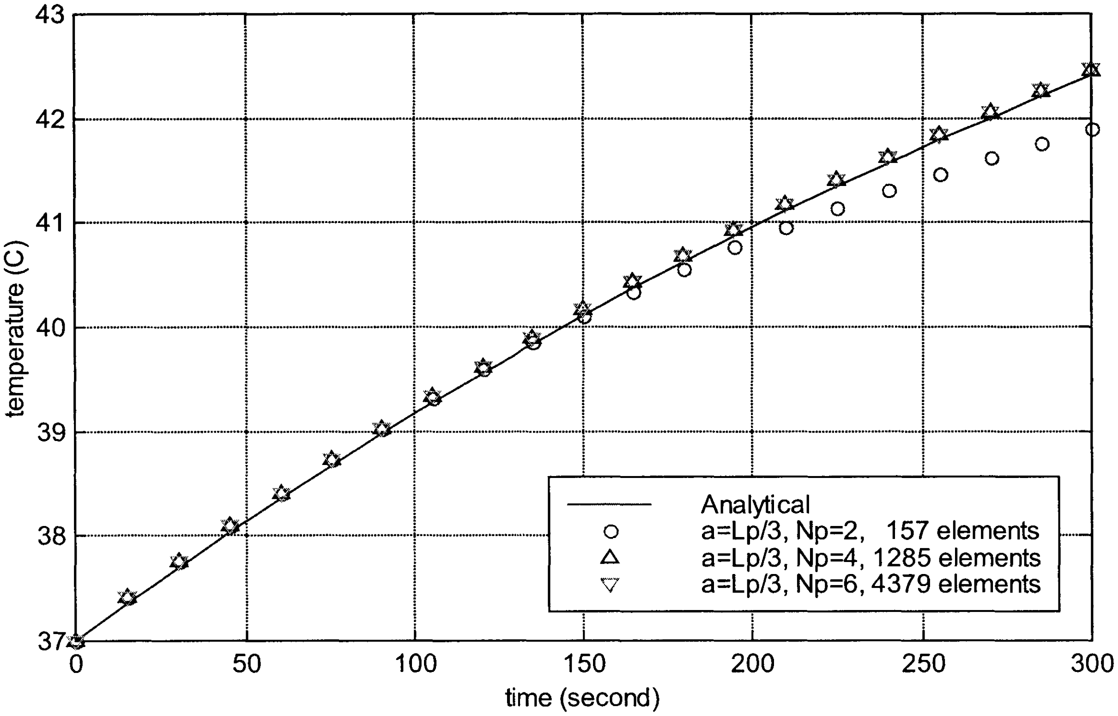

Figure 4-7 Temperature profile for an infinite domain with uniform heat generation and homogeneous initial condition

The integration length effect on the computational errors of transient finite basis element method is showed in Figure 4-8. The clinical perfusion rate is W=11.98 *(ml/min-100g)*. The power strength is $Q=10^5$ (W/m^3). For a small time increment, the error doesn't depend on the integration volume. Therefore, even with a really small integration volume, only 157 elements in this case, the error is still small for a small time increment. This is understandable since the effect of the thermal distance propagates at a certain speed. The error is constant until the effect of the thermal disturbance reaches the integration boundary. After that, dramatic error of underestimate of the temperature appears due to the small integration volume. A larger integration length is good for a large time increment.

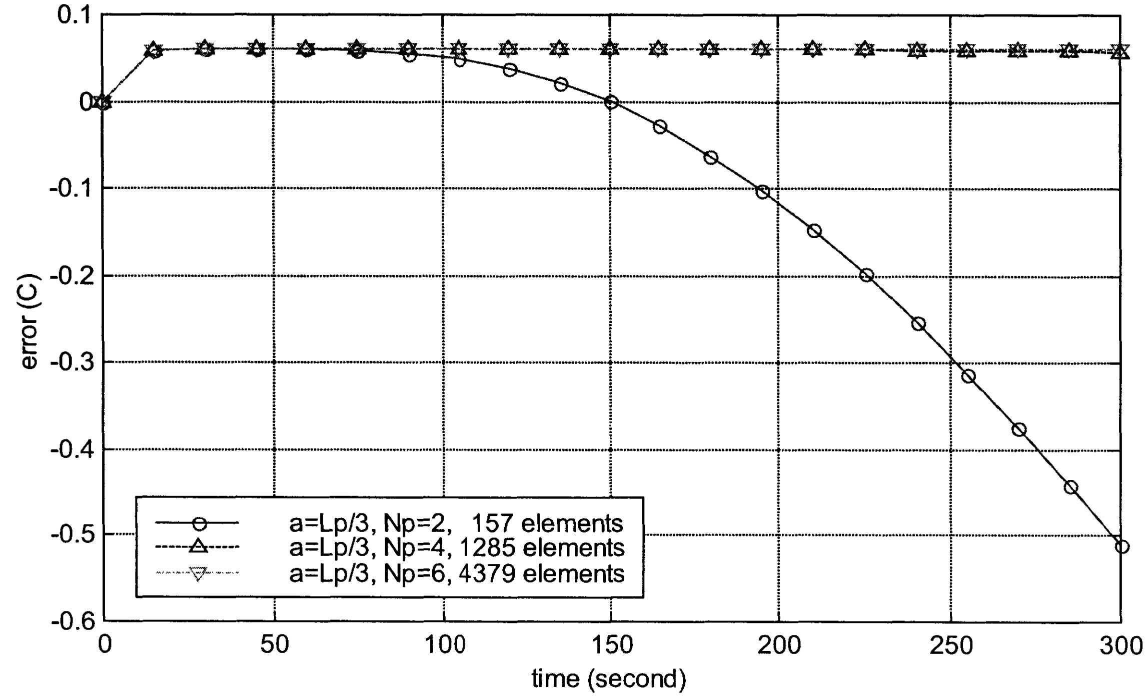

Figure 4-8 The effect of integration length on the computational errors of Transient Finite Basis Element Method for infinite domain with uniform heat generation and homogeneous initial condition ($a = L_p/3$)

Figure 4-9 shows the effect of element's size on the computational errors. The perfusion length is 7.75mm. The clinical perfusion rate is W=11.98 *(ml/min-100g)*. The power strength is $Q=10^5$ (W/m^3). The radius of the elements is one half, one-fourth and one-eighth of the perfusion length, i.e. 3.9mm, 1.9mm and 0.97mm respectively. The integration length is same at 3 times of the perfusion length, i.e. 23.2mm. Therefore, a large element size has less number of elements. The figure shows that for small time increment, the error depends on the size of the elements, the smaller the element, the less the error. The figure also shows that the integration length (3 times of the perfusion length) is not enough for the time increment greater than 300 seconds. The errors start to pile up after 300 seconds.

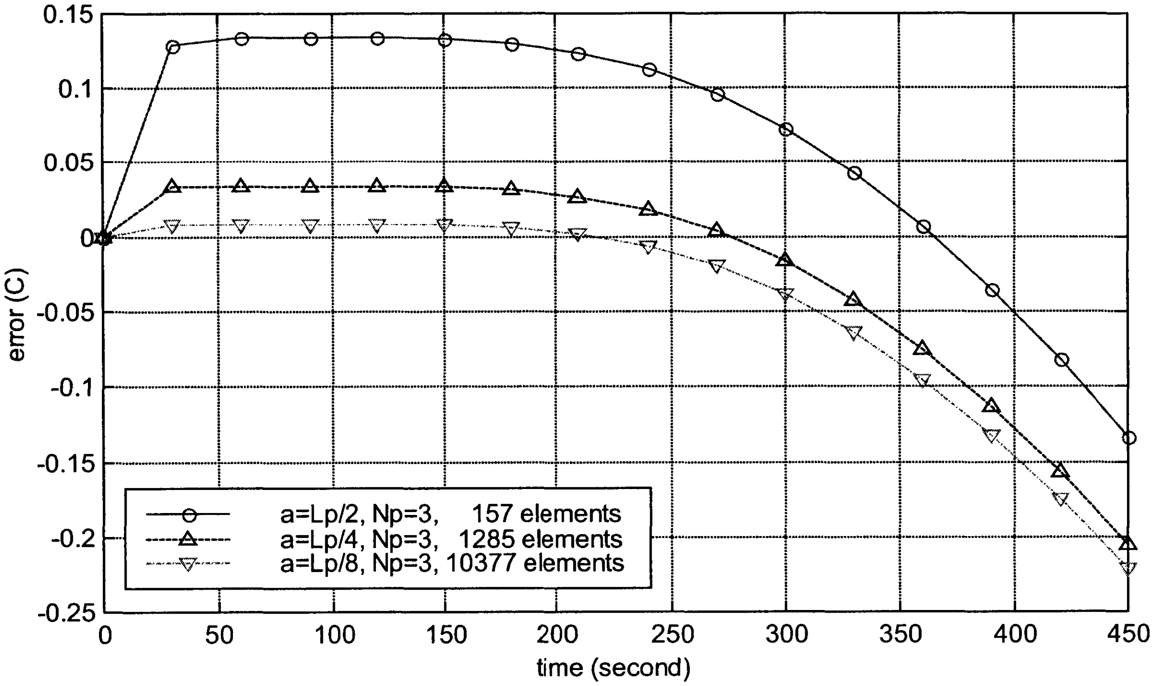

Figure 4-9 The effect the element's size on the computational errors of Transient Finite Basis Element Method for infinite domain with uniform heat generation and homogeneous initial condition (N_p= 3)

Figure 4-10 shows the effect of constant number of integration elements on the computational errors. The constant number of integration elements generally means constant computational effort, i.e. constant CPU cost and constant speed of computation. Although the number of the integration elements is constant, the accuracy is different, which depends on the size of the element. Therefore the choice of the size of the element and the number of perfusion length used in the integration is very important for accuracy and speedy computation. The large integration volume (like $N_p=8$ in this case) is not necessary if the time increment is not large enough, since the thermal disturbance doesn't reach most of the integration volume.

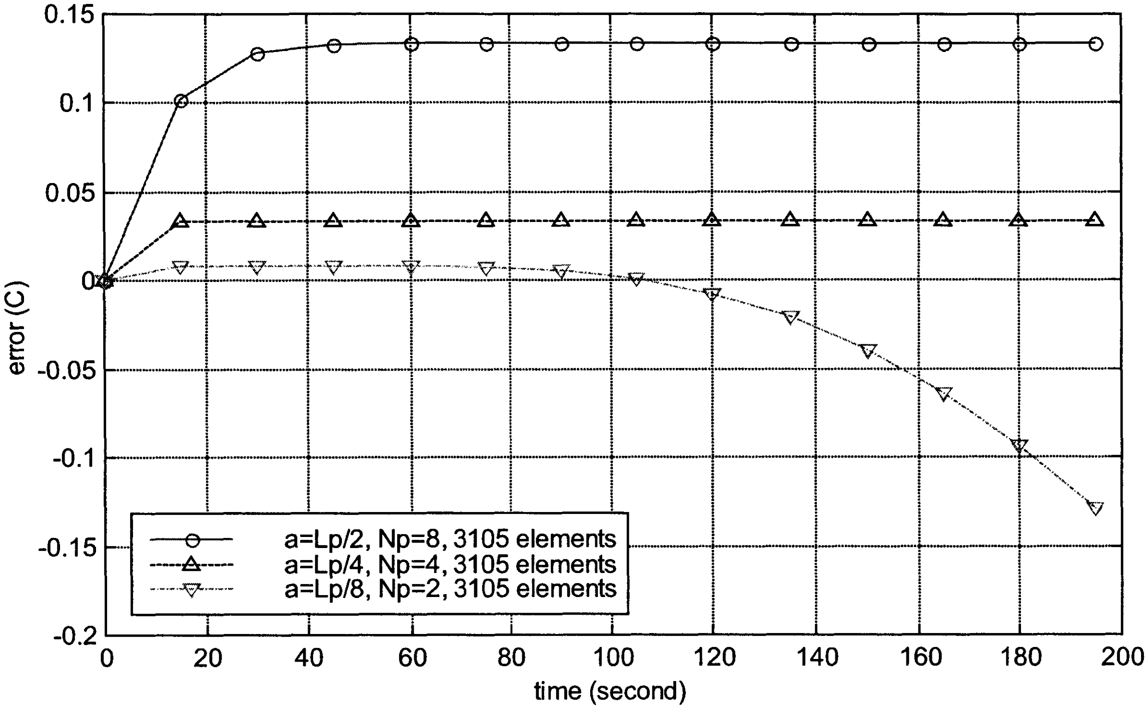

Figure 4-10 The effect of constant number of integration elements on the computational errors of Transient Finite Basis Element Method for infinite domain with uniform heat generation and homogeneous initial condition

Nonzero Initial Temperature

In this test case, there is no internal heat generation. The initial temperature is nonzero. This test case resembles that at the end of the therapy, the heating machine is turnoff, and the tissue is cool off by blood perfusion. The analytical solution is:

$$T(t^+) = T_0 e^{-Pe \cdot t^+} \qquad (4.71)$$

Figure 4-11 shows the temperature profile for an infinite domain with nonzero initial temperature and no internal heat generation. The clinical perfusion rate is W=11.98 *(ml/min-100g)*. The size of the elements is fixed at one-third of the perfusion length. The integration volume is different, i.e. twice, four times and six times of the perfusion length. The agreement of the computational results to the analytical ones is good overall for $N_p=4$ and $N_p=4$. While for $N_p=2$ the disparity becomes obvious from 100 seconds.

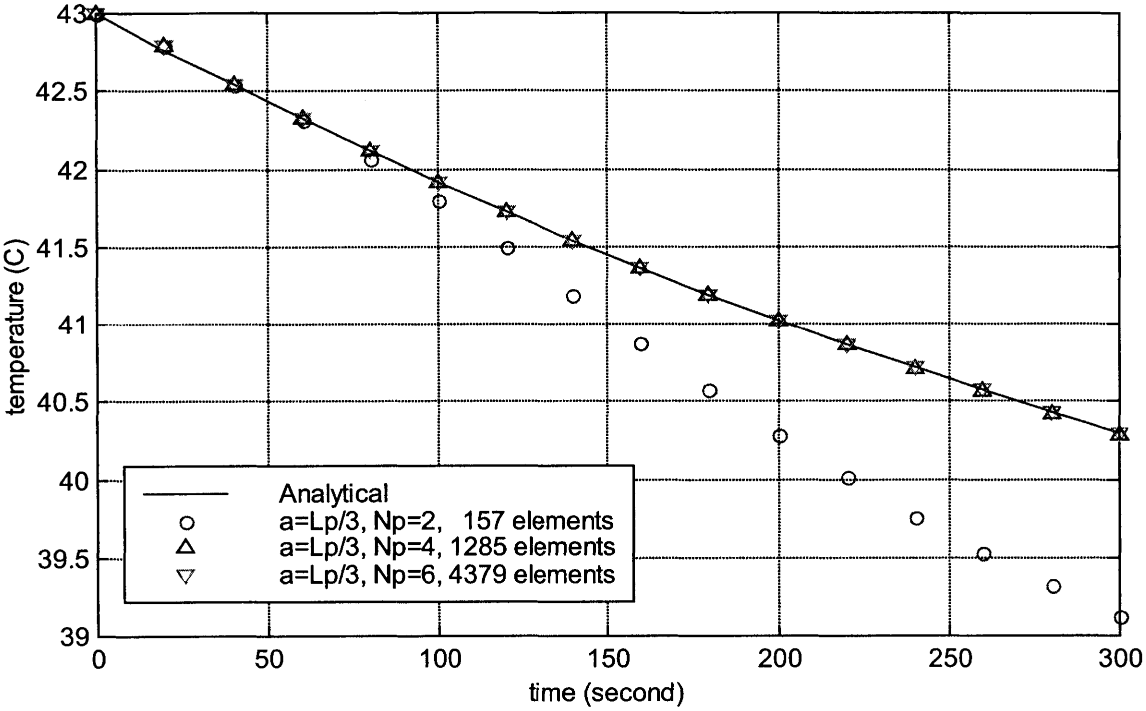

Figure 4-11 Temperature profile for an infinite domain with nonzero initial temperature and no internal heat generation

Figure 4-12 shows the effect of integration length on the computational errors. For a small time increment (t<60 second), the integration length has no effect on the accuracy. For a large time increment, longer integration length is needed in order to maintain enough computational accuracy.

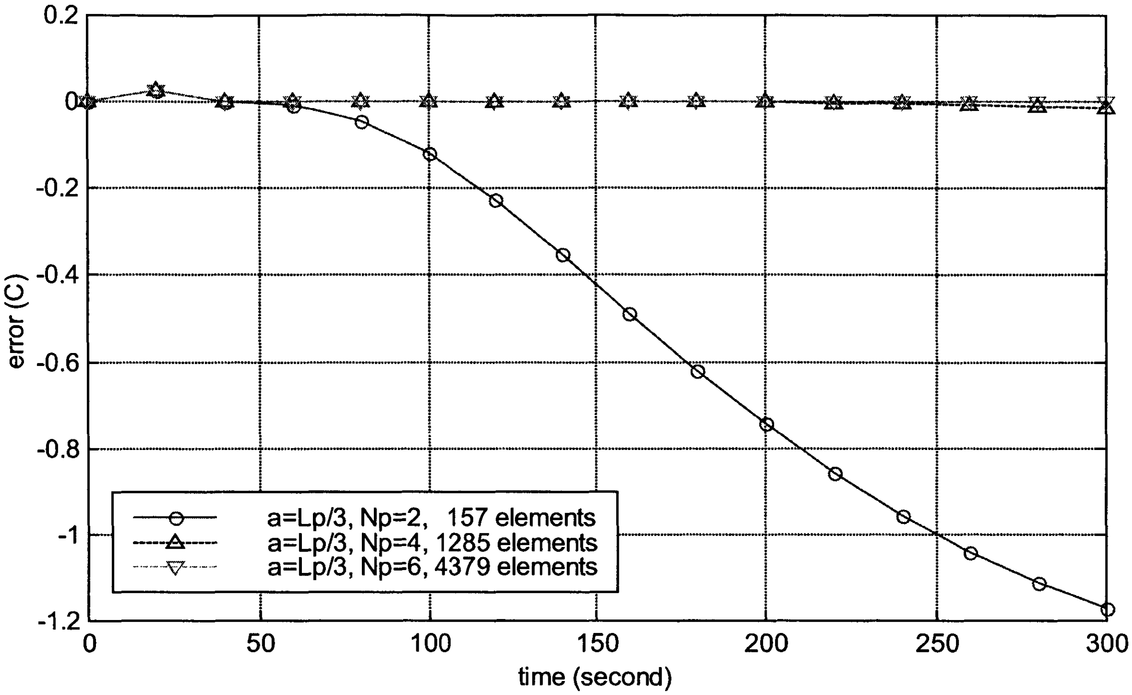

Figure 4-12 The effect of integration length on the computational errors of Transient Finite Basis Element Method for infinite domain with nonzero initial temperature and no internal heat generation (a = $L_p/3$)

Figure 4-13 shows the effect the element's size on the computational errors. The sizes of the elements are a half, one-fourth and one-eighth of the perfusion length respectively. The integration length is same at 3 times of the perfusion length. The Figure shows that the accuracy depends on the size of the element. It is also interested that if the size of the element is small enough ($a \le L_p/3$) the error is zero.

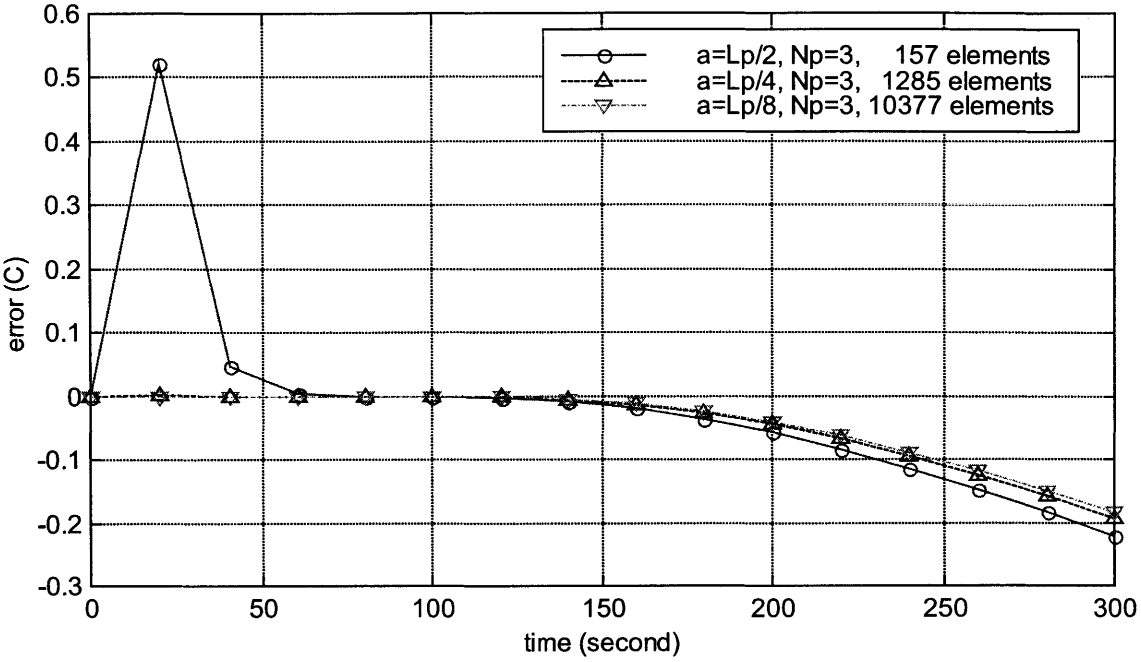

Figure 4-13 The effect the element's size on the computational errors of Transient Finite Basis Element Method for infinite domain with nonzero initial temperature and no internal heat generation (N_p= 3)

Piecewise Oscillating Heating

The last two test cases addressed the process of therapy beginning and therapy ending. When the therapy is in process, the initial temperature is not zero and the heating machine is on. The problem statement for this situation is:

$$\frac{dT}{dt^+} = -Pe \cdot T + q^+ \tag{4.72}$$

The initial conditions are:

$$\begin{cases} T = T_0, t^+ = 0 \\ q^+ = 1, t^+ > 0 \end{cases} \tag{4.73}$$

The analytical solution is:

$$T(t^+) = \frac{q^+}{Pe} - (\frac{q^+}{Pe} - T_0)e^{-Pe \cdot t^+} \tag{4.74}$$

A piecewise oscillating heating process is used as a test case. The purpose of this process is to maintain the tumor tissue's temperature within a therapeutic range. In the test case, the range is 42~44°C. The heating machine is switched to high power level when the tissue temperature drops below 42°C, and switched to low power level when the tissue temperature goes higher than 44°C.

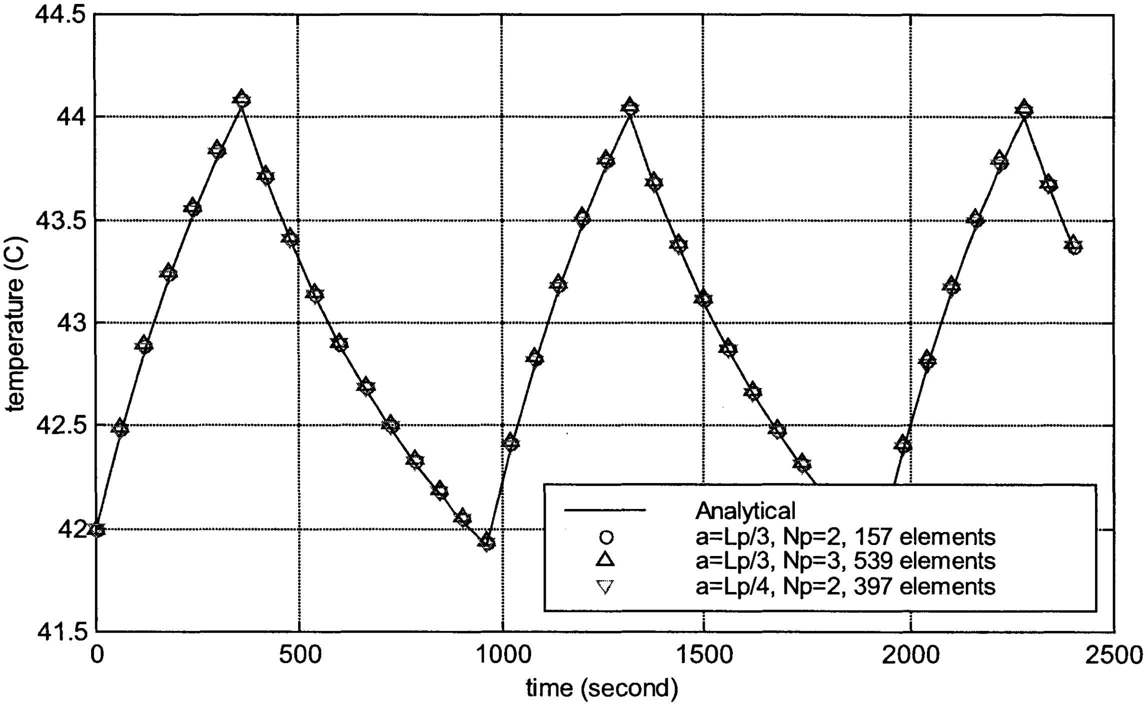

Figure 4-14 The temperature profile of piecewise oscillating heating process

Figure 4-14 shows the temperature profile of piecewise oscillating heating. The sizes of elements are 1/3 and 1/4 of the perfusion length respectively, while the integration length is only 2 and 3 times of the perfusion length. The relatively small number of elements can reduce the computational effort. The temperature is recalculated once every 60 seconds. The high power level is set to be 1.5 times the normal power level, i.e. 75000 W/m^3. The low power level is set to be 1/1.5 times of the normal power level, i.e. 33333 W/m^3. The high power process lasts 6 minutes, followed by 10 minutes of low power process. The agreement of numerical method and analytical method is good.

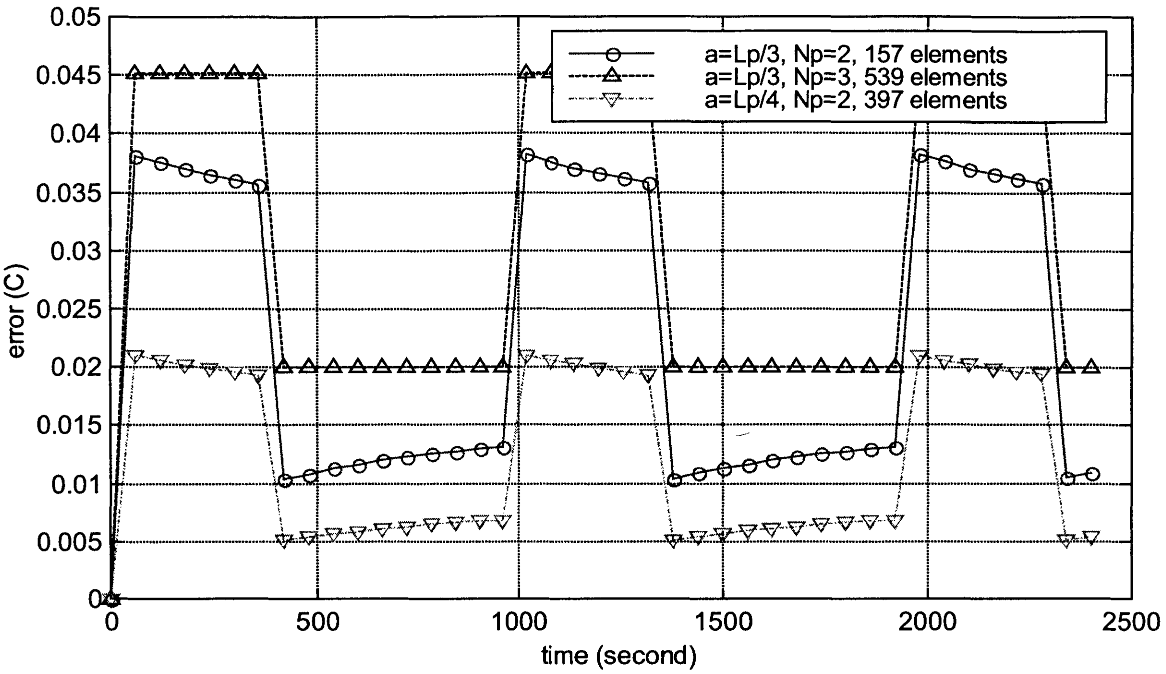

Figure 4-15 The numerical errors of piecewise oscillating heating process

Figure 4-15 shows the numerical errors of piecewise oscillating heating process. The errors are very small although the integration length is small. The errors in the high power level heating process are higher than those in the lower power level heating process.

Half-Space Heating

In local hyperthermia therapy, only target tissue region is heated. Half-space heating is used to resemble this situation. The problem statement is:

$$\begin{cases} \Omega_1 : \dfrac{\partial T_1}{\partial t^+} = \dfrac{\partial^2 T_1}{\partial {y^+}^2} - Pe \cdot T_1 \qquad (y^+ < 0) \\ \Omega_2 : \dfrac{\partial T_2}{\partial t^+} = \dfrac{\partial^2 T_2}{\partial {y^+}^2} - Pe \cdot T_2 + q^+ \qquad (y^+ \geq 0) \end{cases} \tag{4.75}$$

The boundary and initial conditions are:

$$\begin{cases} T_1 = T_2, y^+ = 0 \\ \dfrac{\partial T_1}{\partial y^+} = \dfrac{\partial T_2}{\partial y^+}, y^+ = 0 \\ q^+ = 1, t^+ > 0 \end{cases} \tag{4.76}$$

The solutions in complex domain are:

$$\begin{cases} \Omega_1 : \theta_1 = \dfrac{e^{y^+\sqrt{Pe+s}}}{2s(Pe+s)} \qquad (y^+ < 0) \\ \Omega_2 : \theta_2 = \dfrac{1}{s(Pe+s)}(1 - \dfrac{1}{2}e^{-y^+\sqrt{Pe+s}}) \qquad (y^+ \geq 0) \end{cases} \tag{4.77}$$

The solutions in time domain are:

$$\begin{cases} \Omega_1 : T_1 = \dfrac{1}{2Pe}\left[L_1(-y^+) - L_5(-y^+)\right] \qquad (y^+ < 0) \\ \Omega_2 : T_2 = \dfrac{1}{Pe}(1 - e^{-Pe \cdot t^+}) - \dfrac{1}{2Pe}\left[L_1(y^+) - L_5(y^+)\right] \qquad (y^+ \geq 0) \end{cases} \tag{4.78}$$

Figure 4-16 shows the temperature profile for infinite domain with half-space heating (*a*=L_p/4, *Np*=3). The heating occurs in the region of y>0. The source strength is 10^5 W/m^3.

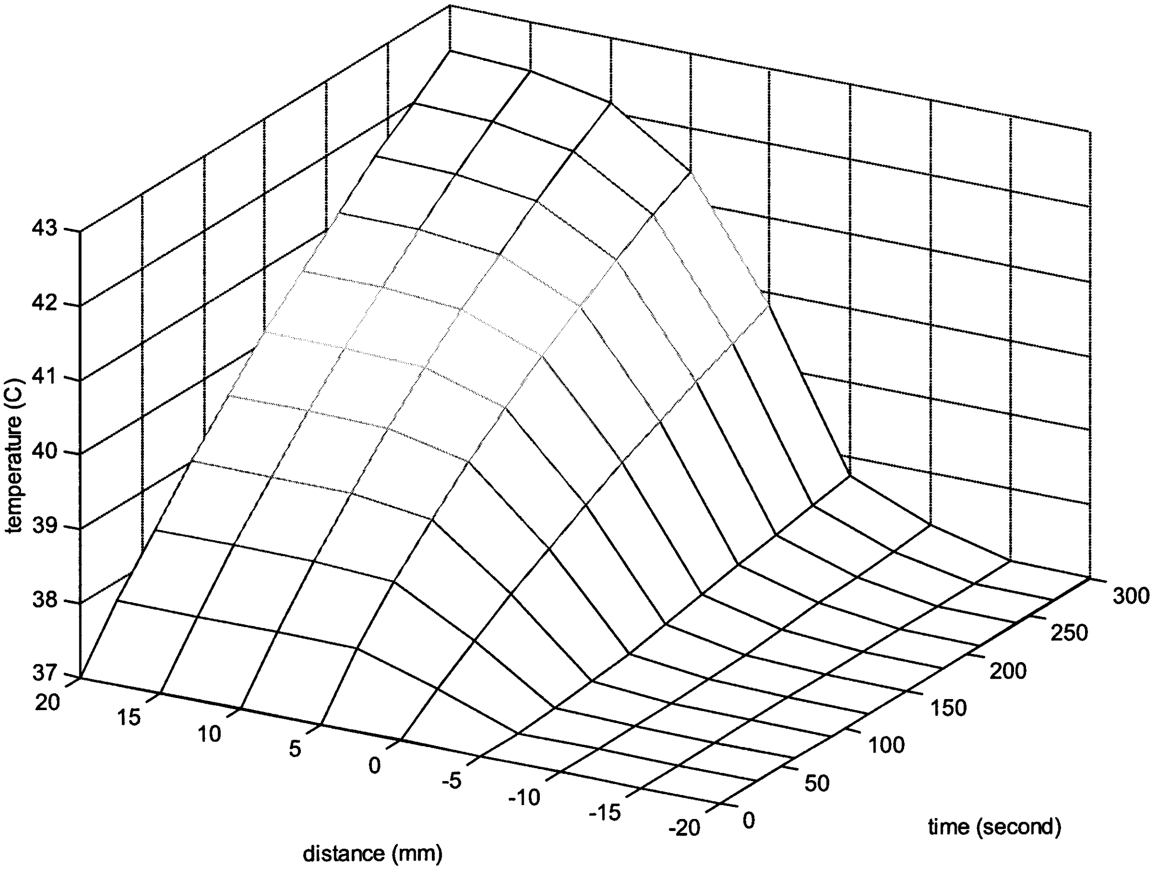

Figure 4-16 The temperature profile for infinite domain with half-space heating (*a*=L_p/4, *Np*=3)

The computational errors for infinite domain with half-space heating (*a*=L_p/4, *Np*=3) are showed in Figure 4-17. The upper plot is a 3-D view and the lower plot is a 2-D view of the error in 30, 90 and 180 seconds time increment. The error is small in general, probably due to the use of small size elements. If the element's size were large, the discontinuity in heating would have significant effect on the accuracy level. The error disturbance area is not large, only about ±10 mm in the test case. Therefore, small size of elements can be used near the boundary for higher level of accuracy and large size of elements can be used in other areas to increase the speed of computation.

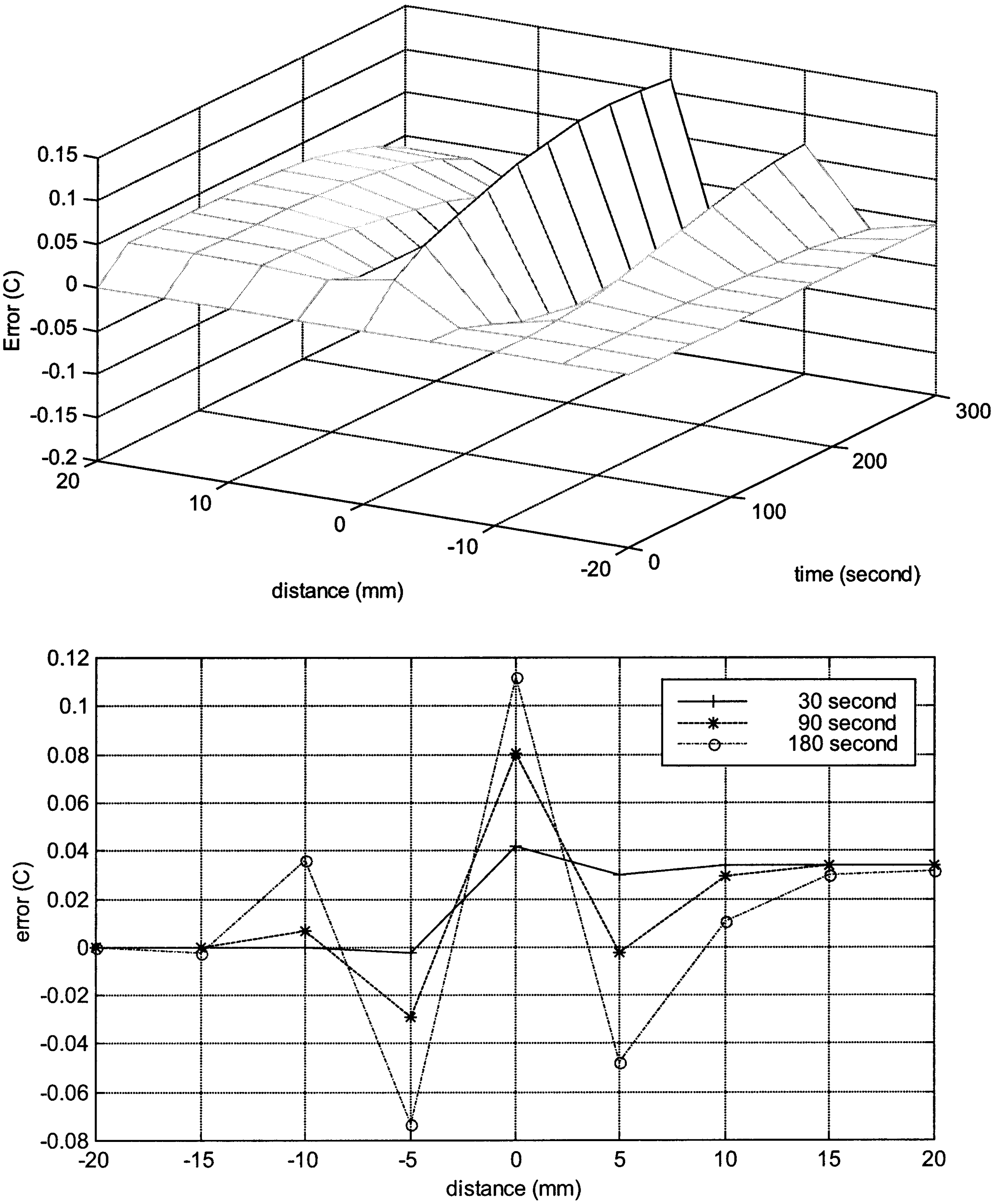

Figure 4-17 The computational errors for infinite domain with half-space heating (*a*=L_p/*4*, *Np*=*3*)

4.5.2 Semi-Infinite Domain with Planar Boundary Conditions

The problem statement is:

$$\frac{\partial T}{\partial t^+} = \frac{\partial^2 T}{\partial y^{+2}} - Pe \cdot T + q^+ \qquad (y^+ \geq 0) \tag{4.79}$$

The initial conditions are:

$$\begin{cases} T = 0, t^+ = 0 \\ q^+ \neq 0, t^+ > 0 \end{cases} \tag{4.80}$$

For 1st kind boundary condition:

$$T = T_0, y^+ = 0 \tag{4.81}$$

The solution is:

$$T = (T_0 - \frac{q^+}{Pe})L_1(y^+) + \frac{q^+}{Pe}L_5(y^+) + \frac{q^+}{Pe}(1 - e^{-Pe \cdot t^+}) \tag{4.82}$$

For 2nd kind boundary condition:

$$\left.\frac{\partial T}{\partial y^+}\right|_{y^+=0} = q_b^+ \tag{4.83}$$

The solution is:

$$T = -q_b^+ L_3(y^+) + \frac{q^+}{Pe}(1 - e^{-Pe \cdot t^+}) \tag{4.84}$$

There is no closed form exact solution for 3rd kind boundary condition due to the difficulty in applying inverse Laplace transform.

Figure 4-18 shows the temperature profile for semi-finite domain with planar boundary condition (1st kind) (*$a=L_p/6$, $Np=3$*). The boundary condition is at y=0 mm, T_0=0 (i.e. baseline temperature 37°C). The heat generation is uniform at 5×10^4 W/m^3.

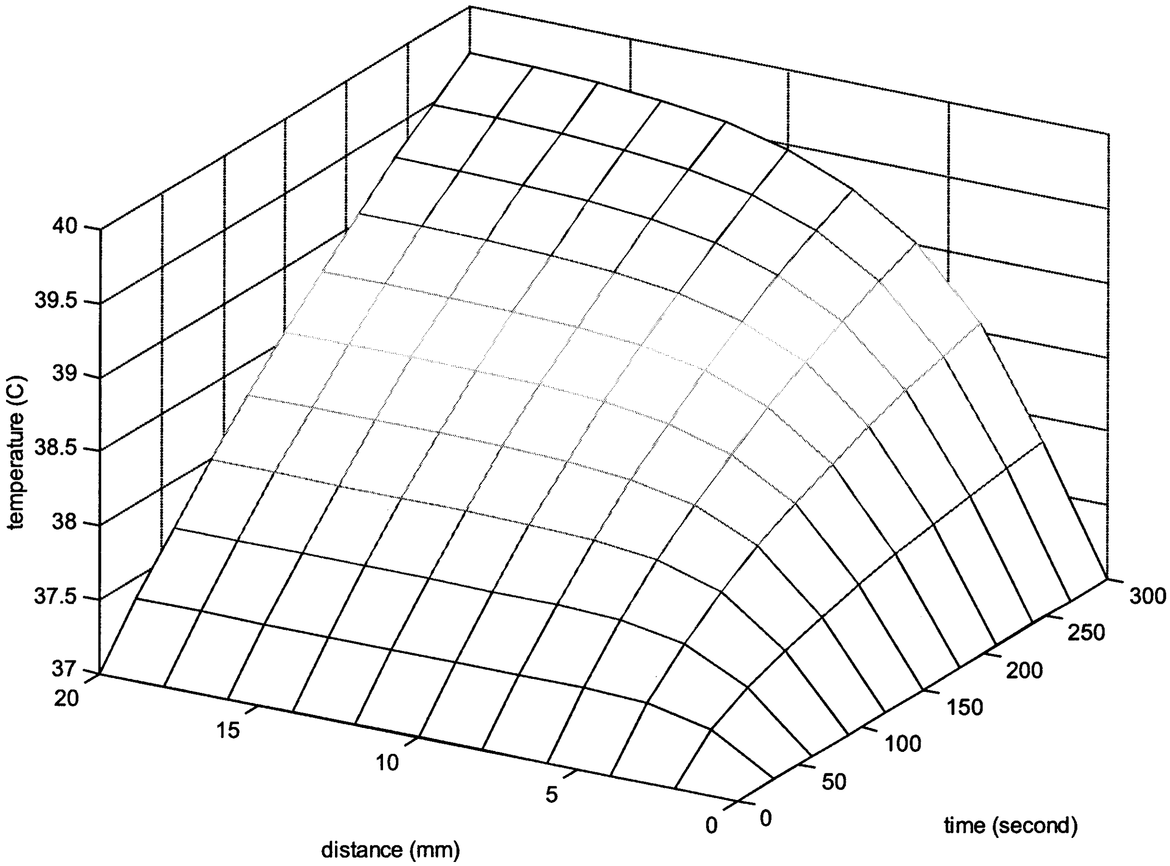

Figure 4-18 The temperature profile for semi-finite domain with planar boundary condition (1^{st} kind) ($a=L_p/6$, $Np=3$)

The computational errors for semi-finite domain with planar boundary condition (1^{st} kind) ($a=L_p/6$, $Np=3$) are showed in Figure 4-19. The 3-D view of the error profile is showed in the upper plot while 2-D view of error profile for time increments at 30, 90 and 180 seconds is showed in the lower plot. Most of the errors are near the boundary. The size of the elements is very small ($a=L_p/6$) in order to obtain a high level accuracy.

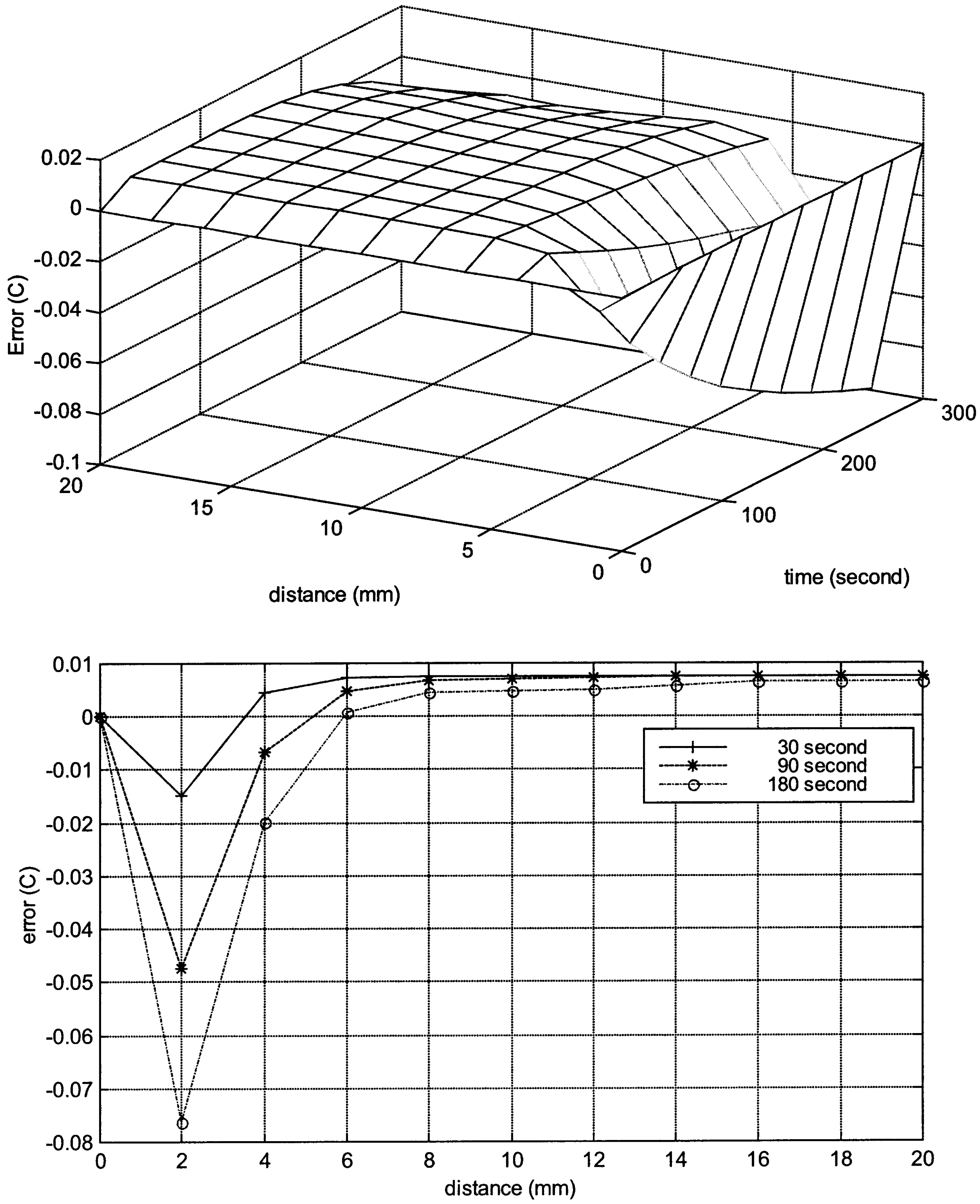

Figure 4-19 The computational errors for semi-finite domain with planar boundary condition (1st kind) ($a=L_p/6$, $Np=3$)

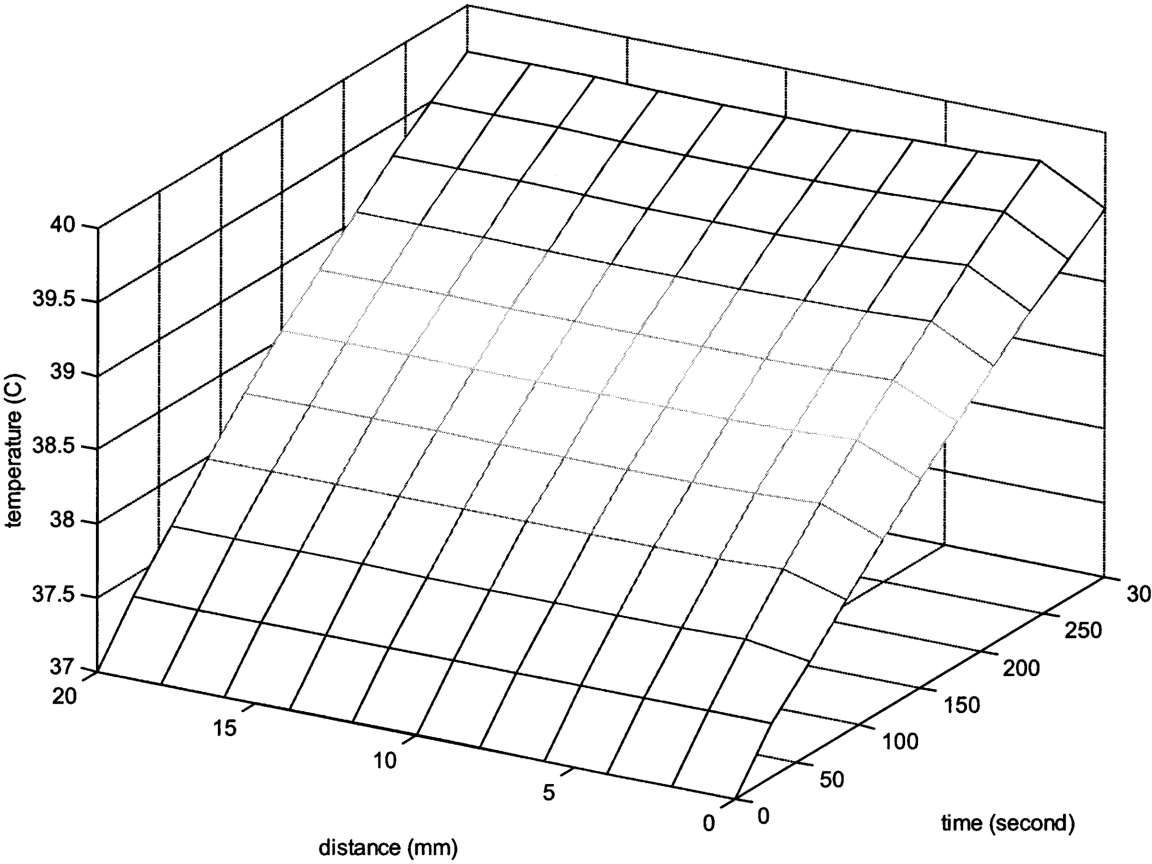

Figure 4-20 The temperature profile for semi-finite domain with planar boundary condition (2^{nd} kind) ($a=L_p/7$, $Np=3$)

The temperature profile for semi-finite domain with planar boundary condition (2^{nd} kind) ($a=L_p/7$, $Np=3$) is showed in Figure 4-20. The boundary condition is homogeneous, i.e. at $y=0$ mm, $q_b^+=0$. The heat generation is uniform at 5×10^4 W/m^3.

Figure 4-21 shows the computational errors for semi-finite domain with planar boundary condition (2^{nd} kind) ($a=L_p/7$, $Np=3$). The 3-D view of the error profile is showed in the upper plot while 2-D view of error profile for time increments at 30, 90 and 180 seconds is showed in the lower plot. Errors can be observed near the boundary. The size of the elements is $L_p/7$.

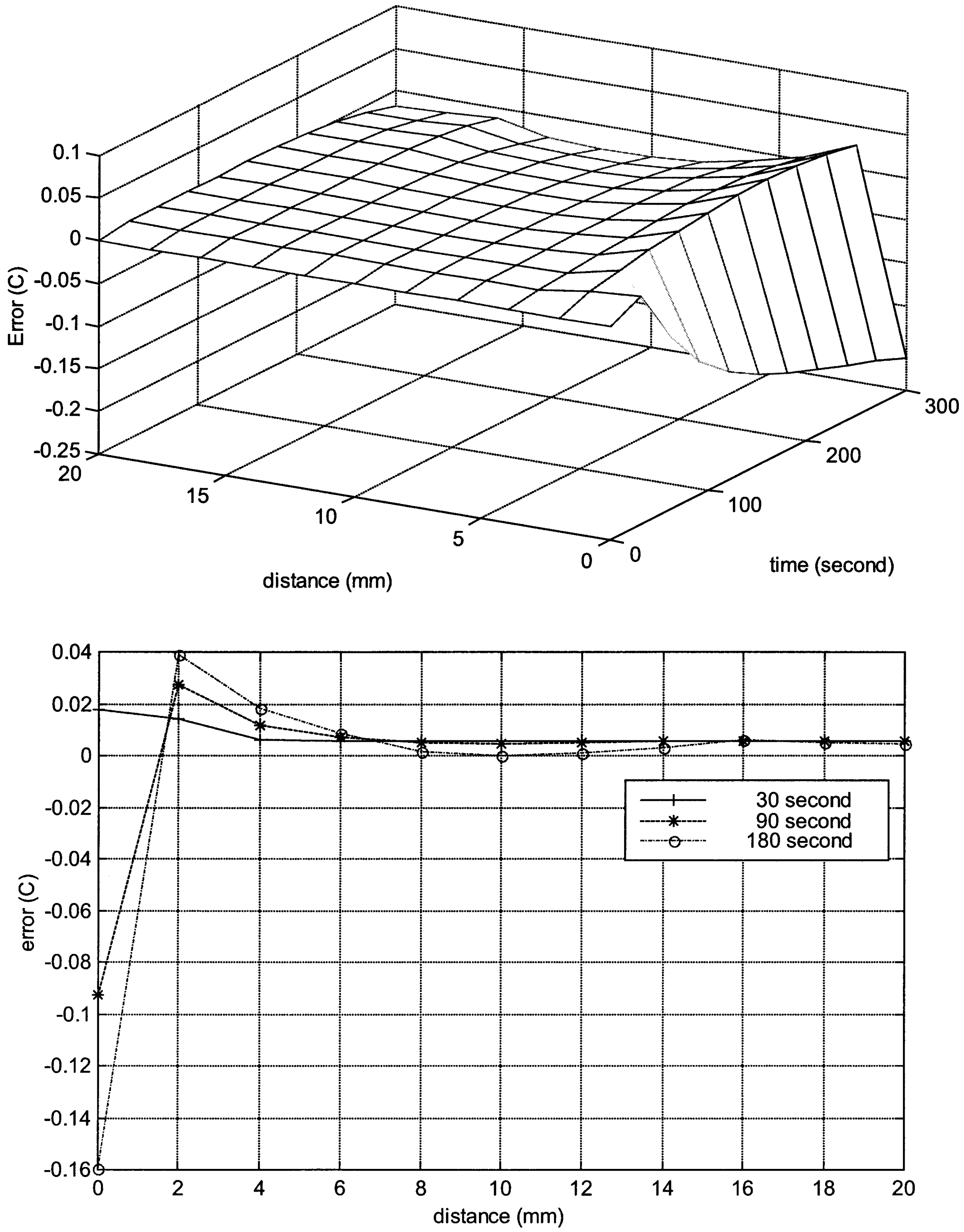

Figure 4-21 The computational errors for semi-finite domain with planar boundary condition (2^{nd} kind) ($a=L_p/7$, $Np=3$)

4.5.3 Comparison with Finite Element Solutions

Finite Element Method is a standard numerical method to solve partial differential equations. Therefore, it is a useful to compare the transient Finite Basis Element Method to transient Finite Element Method. The transient method used in the comparison is implicit backward Euler method. The bioheat transfer equation is:

$$\frac{1}{\alpha_m}\frac{\partial T}{\partial t} = \nabla^2 T - \lambda^2 T + \frac{Q}{k_m} \tag{4.85}$$

discretizing time, where n+1 is the next time step, n is the previous time step:

$$\frac{\partial T}{\partial t} = \frac{T^{(n+1)} - T^{(n)}}{\Delta t} \tag{4.86}$$

Other terms in the equation are in time step (n+1):

$$\frac{1}{\alpha_m}\frac{T^{(n+1)} - T^{(n)}}{\Delta t} = \nabla^2 T^{(n+1)} - \lambda^2 T^{(n+1)} + \frac{Q}{k_m} \tag{4.87}$$

Combining the coefficient of common terms, we have:

$$(\nabla^2 - \lambda^2 - \frac{1}{\alpha_m \Delta t})T^{(n+1)} + \frac{Q}{k_m} + \frac{T^{(n)}}{\alpha_m \Delta t} = 0 \tag{4.88}$$

The implicit backward Euler method is stable for all Δt theoretically. The level of accuracy is first order of Δt. Therefore, for large time increment, this method has to compute through multiple time steps in order to maintain a certain level of accuracy.

The geometry used in the test is the cubic tumor model used in the previous chapter. Uniform source (10^5 W/m^3) is applied to the tumor region. The thermal properties and perfusion are uniform in the whole domain. The clinical perfusion rate is W=11.98 *(ml/min-100g)*. The perfusion length is 7.75mm. The temperature profile of tumor region heating with homogeneous initial condition (zero initial temperature elevation) for time increment of 60 seconds is showed in Figure 4-22. The tumor region is between 50~150mm. For transient FBEM, the element radius is 1/4 of the perfusion length, i.e. 1.94mm. The integration length is 3 times of perfusion length, i.e. 31mm. For FEM, two time steps are used, which are 10 second and 60 second respectively. For time step equals to 10 second, FEM needs to compute 6 times before the results for time increment of 60 seconds are obtained. For time step equals to 60 second, FEM needs to compute only once to get the results for time increment of 60 seconds. For FBEM, the computation is only once. The figure shows that the numerical results agree with the analytical solution.

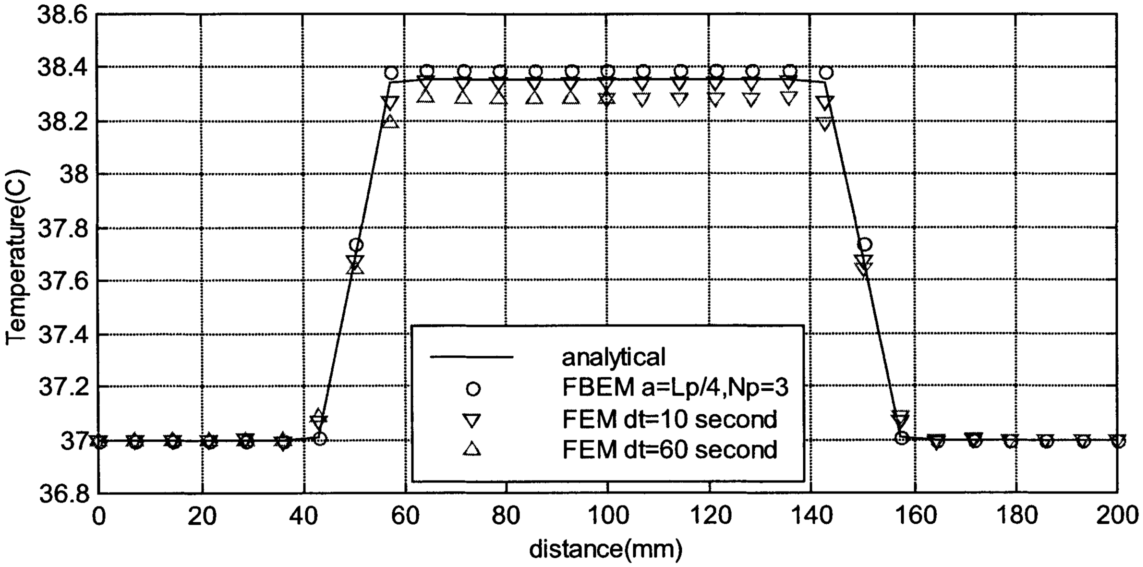

Figure 4-22 The temperature profile of tumor region heating with homogeneous initial condition for transient FBEM and FEM comparison (t=60 second)

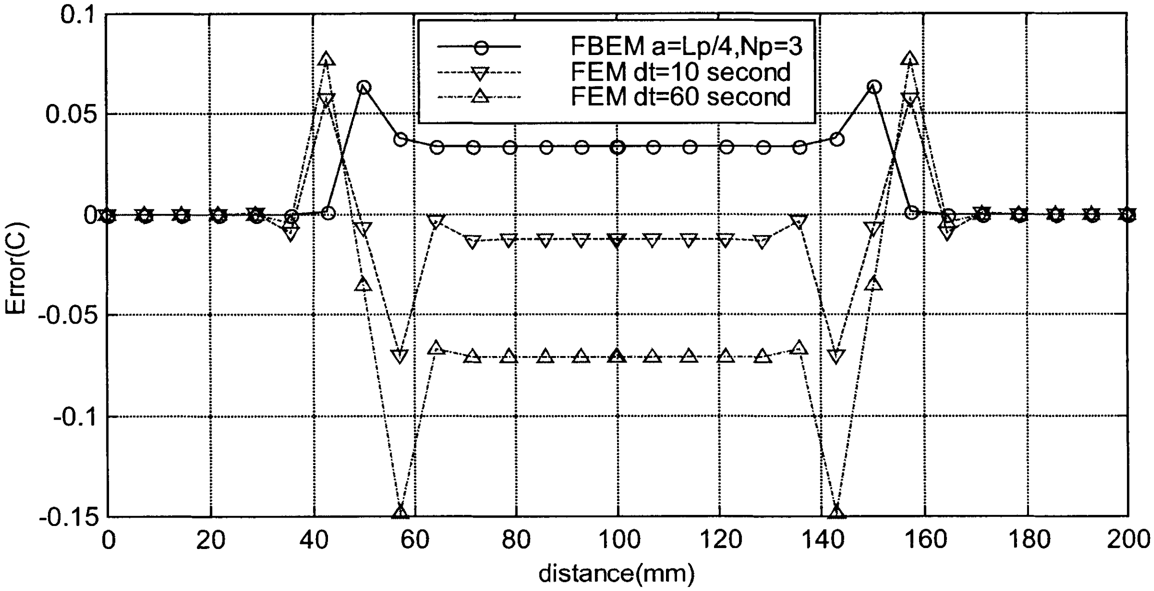

Figure 4-23 The error profile of tumor region heating with homogeneous initial condition for transient FBEM and FEM comparison (t=60 second)

The error comparison of tumor region heating with homogeneous initial condition (zero initial temperature elevation) for time increment of 60 seconds is showed in Figure 4-23. The figure shows that the errors near the boundary are larger than those inside the tumor region. FEM with dt=10 has the same accuracy level as FBEM on the boundary region, while it is more accurate inside the tumor region. FEM with dt=60 has the largest errors. This is due to that the error is proportional the time step, the larger the time step, the higher the error. For FBEM, there is no time step limitation. It can compute at any time increment. The only limitation for large time increment is that the integration length needs to be long enough such that the effect of the heat source doesn't penetrate the integration boundary.

The advantage of transient FBEM over FEM is much more obvious for large time increment. Figure 4-24 shows the temperature profile of tumor region heating with homogeneous initial condition for t=180 second. For FEM with dt=10 second, it needs to compute 18 times to get the solution for t =180 second. For FEM with dt=60 second, 3 times of the computation are needed. However, for transient FBEM, it still can get the solution by one computation. The agreement of the numerical and analytical solutions is good at a glance.

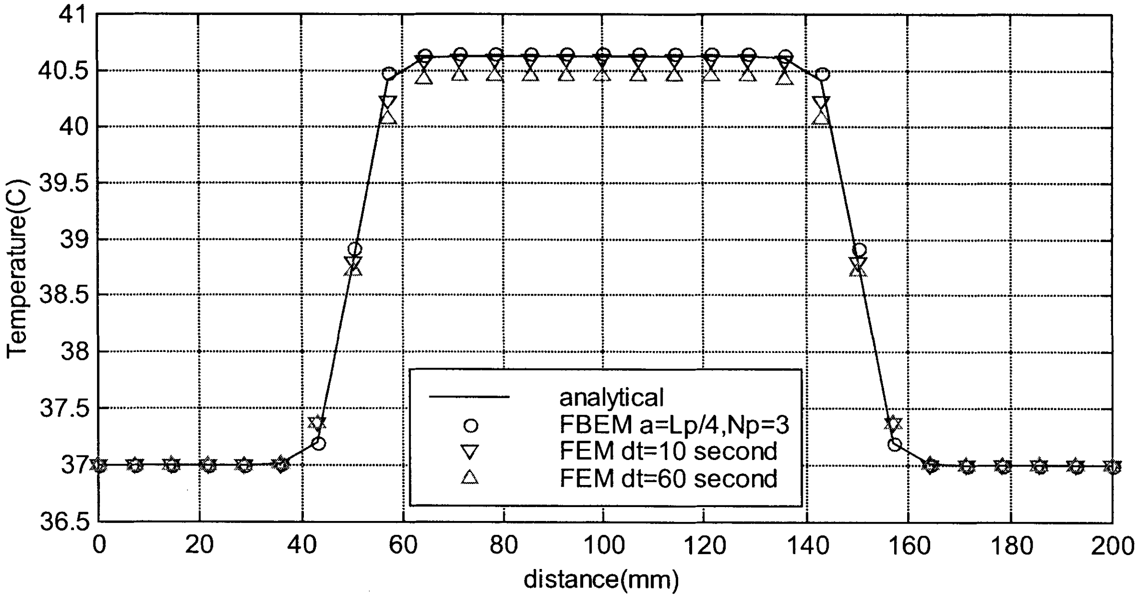

Figure 4-24 The temperature profile of tumor region heating with homogeneous initial condition for transient FBEM and FEM comparison (t=180 second)

The error comparison of tumor region heating with homogeneous initial condition (zero initial temperature elevation) for time increment of 180 seconds is showed in Figure 4-24. The figure shows that the accuracy level for FEM with dt=10 is close to that of the FBEM on the boundary, as well as inside the tumor region. FEM with dt=60 still has the largest errors. Considering the fact that it requires 18 iterations over the time step to get the solution for FEM with dt=10, the computational advantage is clearly on the side of transient FBEM.

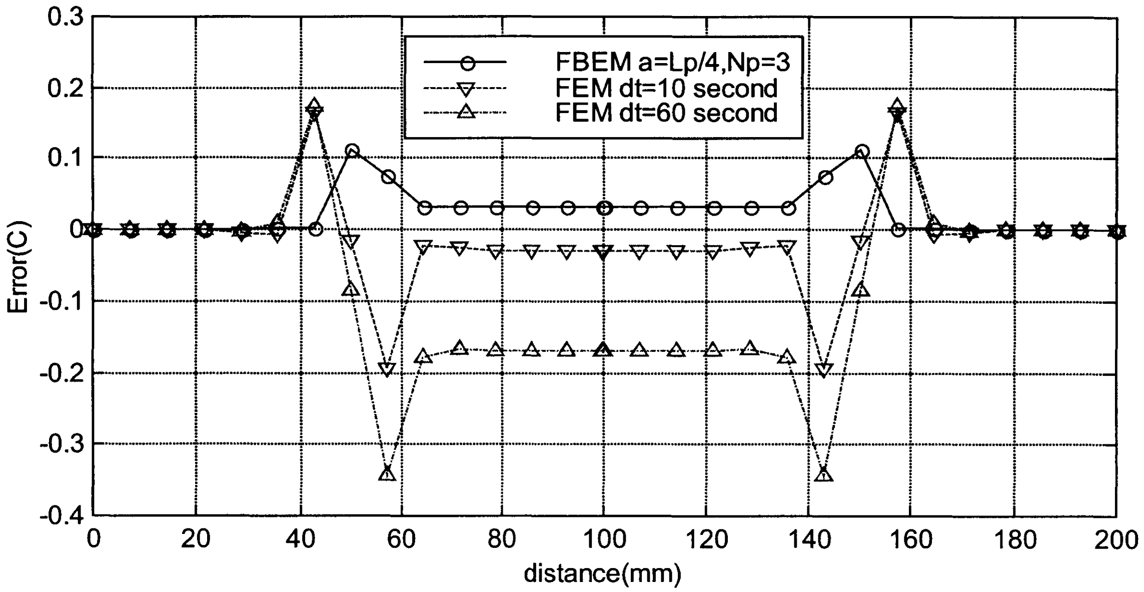

Figure 4-25 The error profile of tumor region heating with homogeneous initial condition for transient FBEM and FEM comparison (t=180 second)

4.5.4 Validation Discussions

Volume of Integration

In FBEM, the temperature is calculated by the contribution of the sources within a limited volume. The contribution of the sources outside of the volume is too small to be included in the calculation. The integration volume in transient Finite Basis Element Method is determined by balancing the speed-accuracy trade-off. Figure 4-26 shows the computational errors as a function of the integration volume for infinite domain with uniform heat generation and homogeneous initial condition (a = $L_p/3$). The perfusion length is 7.75mm. The clinical perfusion rate is W=11.98 *(ml/min-100g)*. The power strength is $Q=10^5$ (W/m^3). Same sizes of the elements are used. The radius of the elements is $L_p/3$. The time increments are 60, 180, 600, and 1800 second respectively. The figure shows that for time increment equals to 60 seconds, the accuracy level doesn't change within the radius range of 1~8 times of the perfusion length. The reason is that since the time increment is small, the thermal disturbance length is so short that it has not penetrated the integration boundary. For t=1800 second, which is close to steady state, the thermal disturbance length is about 6 times of the perfusion length. Any integration length less than that value lead to underestimate of temperature and large error. For t=180 and 600 second, the thermal disturbance lengths are about 2 and 4 times of the perfusion length respectively.

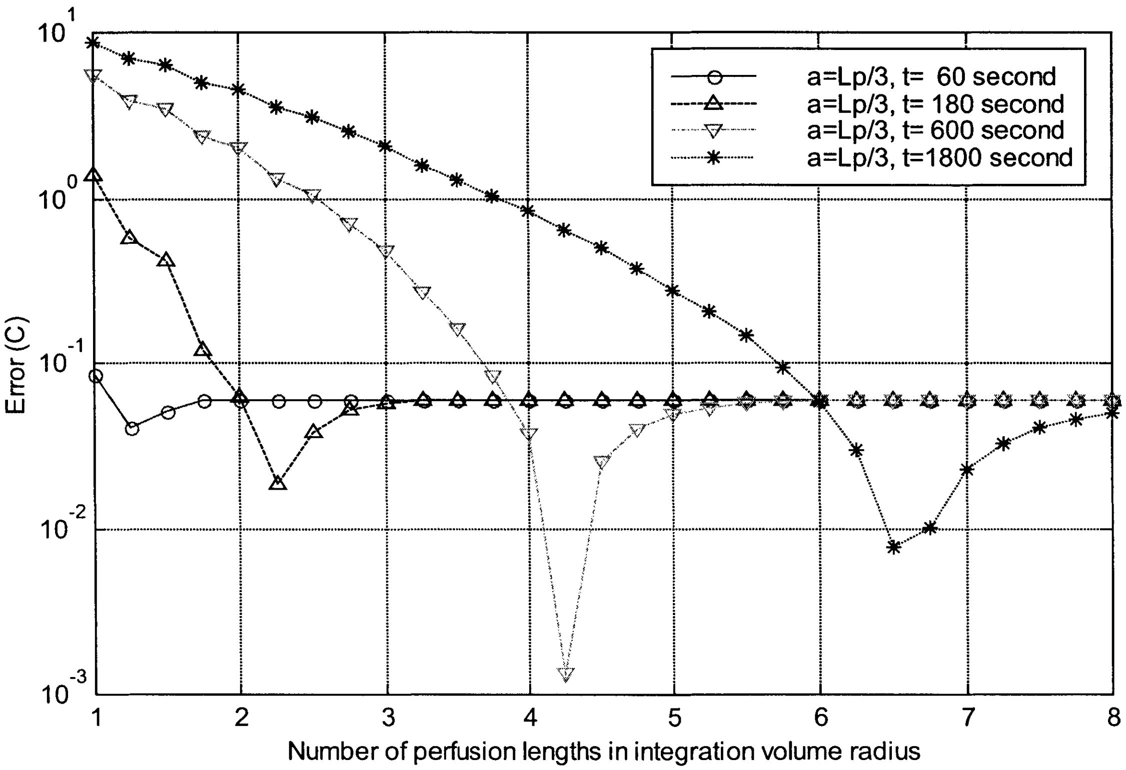

Figure 4-26 The computational errors as a function of the integration volume for infinite domain with uniform heat generation and homogeneous initial condition (a=$L_p/3$)

The figure also shows that, if the temperature field needs to be recalculated once every 1~3 minutes, an integration length of 1~2 times of the perfusion length is enough. Since the volume is proportional to the cubic of the length, the number of elements required for transient FBEM is much less than the number of elements required for steady state FBEM. For example, comparing to the integration length of 6 perfusion length for steady state, the integration length is about 1~2 perfusion length for time increment of 180 second, therefore only 1/216~1/27 of the elements are needed in this case comparing to the steady state situation. This is clearly a huge advantage for transient FBEM over the steady state FBEM.

Size of Element

In practice, spherical elements are used in FBEM. These elements cannot occupy the whole volume, which leads to void volume that cannot be represented by elements. Packing factor is introduced to alleviate the effect. In theory, smaller elements present the distributed source more accurate than large elements, which results in more accurate in temperature computation. Therefore, the size of the element determines the level of accuracy that can be reached by transient FBEM. Figure 4-27 shows the computational errors as a function of the element size for infinite domain with uniform heat generation and homogeneous initial condition (N_p=6). The perfusion length is 7.75mm. The clinical perfusion rate is W=11.98 *(ml/min-100g)*. The power strength is $Q=10^5$ (W/m^3). The perfusion length is chosen to be large enough for all the time increments. The figure shows that the smaller the size, the smaller the computational error. However, the use of smaller elements increases the number of the elements if the integration volume doesn't change, thus increases the computation time. For general-purpose computation, the computational error around 0.1°C is acceptable. The corresponding element radius is about 1/2~1/4 of the perfusion length from the figure.

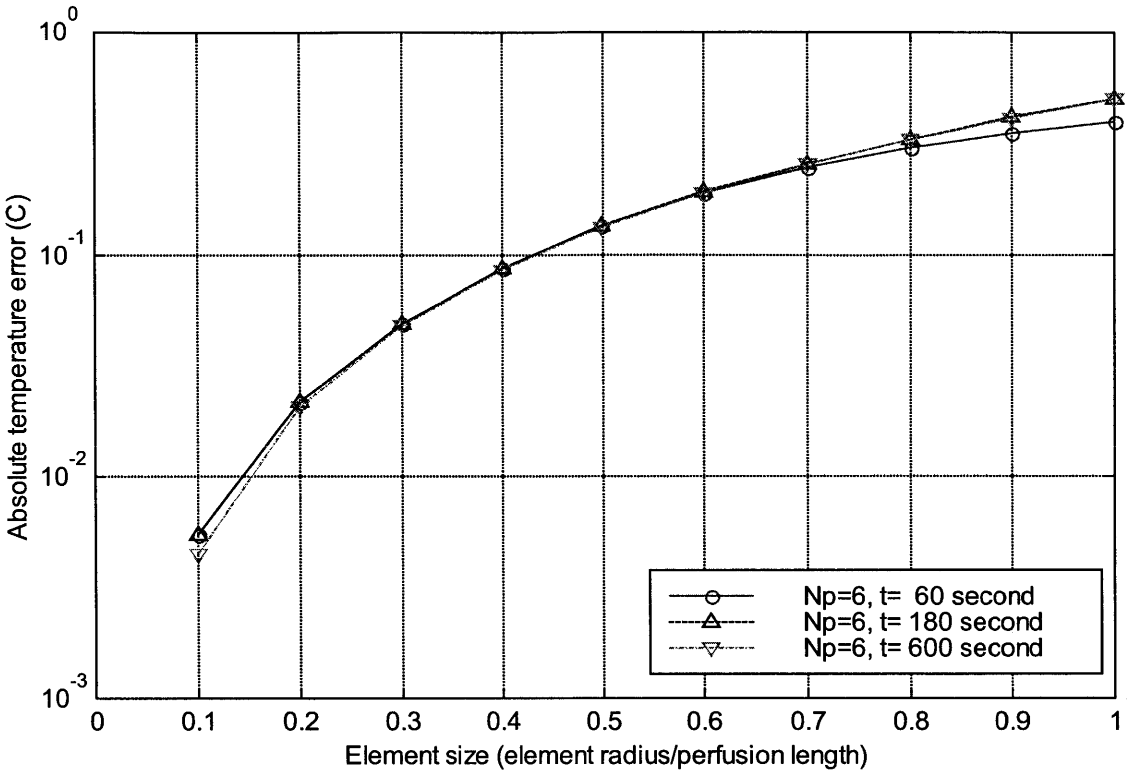

Figure 4-27 The computational errors as a function of the element size for infinite domain with uniform heat generation and homogeneous initial condition (N_p=6)

Speed-Accuracy Comparison

The computation time is proportional to the number of elements in the integration volume. For each element calculation, the computation burden is on the calculation of square root function, exponential function and error function. Figure 4-28 shows the computational errors as a function of the computation time per node for infinite domain with uniform heat generation and homogeneous initial condition. The figure shows that for the computational error around 0.1°C, the computation time per node is about 1 second. If the temperature field needs to be recalculated every 2 minutes, the total nodes that can be calculated within the time frame is about 120. In order to speed up the computation, the combined element method is used. This method automatically combines the elements that make the same contribution to temperature elevation. This generally refers to the elements with the same distance away from the node point and the same thermal properties and perfusion. The element contribution to temperature elevation is only calculated once and then multiplied by the number of the combined elements. This method works really well for infinite domain with uniform properties and perfusion. It can reduce the number of elements needs to be calculated to about 1/10 of the original elements. The figure shows that for the combined element method, the computation time is about 0.1 second for the computational error around 0.1°C. Therefore, for a tumor volume with 1000-node-mesh, this method can recalculate the temperature in less than 2 minutes.

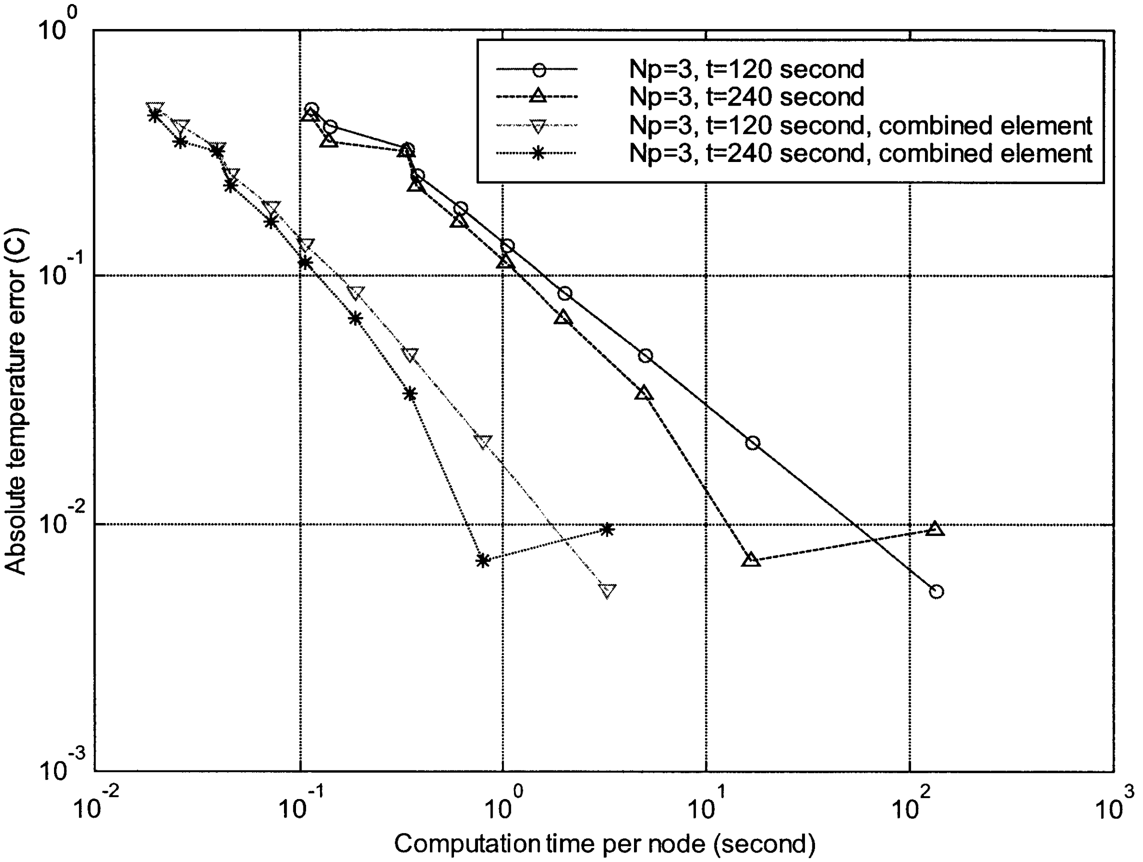

Figure 4-28 The computational errors as a function of the computation time per node for infinite domain with uniform heat generation and homogeneous initial condition

When there are boundaries nearby, either externally or internally, the effect of the combined element method is less significant. The reduce number is about 1/2 of the original elements in some cases. Another way to increase the computation speed is to use the “loop-up tables” for the computational intensive tasks such as the calculation of square root function, exponential function and error function. By modifying the computational intensive tasks to less intensive looking up table and interpretation, the speed of the computation should increase significantly.

4.6 Summary of Transient Thermal Analysis

This chapter describe the theoretical background based on Green's function solution and Laplace transform of transient thermal analysis; the formulation of various practical transient elements accounting for different source distribution conditions, initial conditions and boundary conditions, including external boundary conditions and internal boundary conditions due to discontinuity in source distribution or thermal properties and perfusion; the validation of the transient algorithm.

In the formulation section, two free-space transient elements are formulated, which includes transient uniform Finite Basis Element with nonzero source distribution and transient Finite Basis Element with nonzero initial temperature; two external bounded elements are developed, which includes planar boundary element and spherical boundary element; two internal boundary elements for variable thermal properties and perfusion are presented, which includes internal planar boundary condition and internal spherical boundary. In practice, most of the clinical hyperthermia situation can be represented by the combination of these elements.

In the validation section, the transient Finite Basis Element Method validation is performed by the comparisons to problems with exact analytical solutions. The comparison with Finite Element Method is also presented. The effects of integration volume, element size and boundary vicinity are also discussed.

Chapter 5

Conclusions

In this thesis, two critical components for the thermal management system, i.e. the inverse thermal analysis for creating an optimal temperature pattern in the tumor volume and the transient thermal analysis for real-time temperature reconstruction, have been developed. The conclusions will be presented in the following sections for inverse and transient thermal analysis respectively.

5.1 Inverse Thermal Analysis

The inverse thermal analysis in this thesis falls into two categories: the inverse thermal analysis for desired power field and the combined inverse thermal analysis which links the optimal temperature field to the control parameters of the energy delivery machine.

For the first category, the analytical solutions for one-dimensional half-space tumor model and spherical tumor model are derived. The inverse algorithms for FBEM and FEM have been developed respectively. The simulations for cubic tumor model using inverse FBEM and inverse FEM have been demonstrated. The results show two different kinds of power field are preferable for creating uniform temperature distribution within the tumor volume: the volumetric distributed source and the surface source. The volumetric distributed source is used to compensate the heat loss carried out by blood perfusion. The source strength depends on the temperature elevation and the blood perfusion rate. The surface source is used to compensate the heat loss across the tumor boundary. The source strength depends on the temperature gradient and tissue thermal conductivity. The surface source is a surface delta function with an infinitesimal small thickness. The strength of the surface source is very high generally. In practice, it is very difficult to create this kind of surface source distribution by current energy delivery machine. These conclusions can be used as general guidelines for the design of energy delivery machines. The speed-accuracy comparisons of FBEM and FEM show that both methods are computational intensive, however, FBEM is faster than FEM by an order of magnitude with moderate root mean square (RMS) errors.

For the second category, the algorithm for combined inverse thermal analysis, which can link the optimal temperature field to the control parameters of the energy delivery machines, is derived. Normalized source is used to represent the concentrated source and normalized source array is used to represent the effect of energy delivery machine with multiple transducers. The numerical simulations for the combined thermal analysis are presented in three tumor models, i.e. the cubic tumor model, the spherical tumor model and the ellipsoidal tumor model. The simulation results show that with the judicial choice of source placement, by adjusting the strength of the individual source in the source array, the resulting temperature field is within a therapeutic temperature range, with the RMS errors of less than 1°C. The source placement plays an important role in the outcome of the optimization. So far the choice of the source placement is based on experiences and intuition, rather than lumping the position parameters into the optimization process due to complexity. The perfusion level determines the number of sources required and the bandwidth of the sources.

5.2 Transient Thermal Analysis

For the transient thermal analysis, a fast algorithm based on source superposition, Green's function solution and Laplace transform has been developed. Various practical transient elements have been formulated. The method is validated by the comparisons to the exact solutions of problems with simple geometries.

In theory, there is no limit on the accuracy level that can be achieved by the transient FBEM. In practice, the packing method, the size of the element and the integration volume are the three major factors in determining the level of accuracy that can be achieved. The validations show that the numerical results approach the exact solutions as the size of the element decreases. The integration volume, unlike in the steady state, has less effect on the level of accuracy unless the thermal disturbance reaches the integration boundary. The required integration length in transient analysis is much less than the required integration length in steady state computation. For example, for the time increment of 3 minutes, the integration length is about 2~3 times of the perfusion length for transient computation, comparing to the 6 times of the perfusion length required for steady state computation. Therefore, the integration volume for transient analysis is much less than the volume for steady state. In this case it is about $(1/2)^3$, i.e. 1/8 since the volume is proportional to the cubic of the length.

The computation speed depends on the number of elements used in the computation. With less elements used in transient analysis, the computation speed is about 10 times faster than its steady state counterpart. The steady state FBEM is about 10 times faster than FEM demonstrated in the previous section. If the FEM needs more than 10 iterations to get the results, which is very possible, then the transient FBEM would be 1000 times faster than the FEM. Therefore, the speed advantage of FBEM in transient analysis is much dominant. The speed-accuracy comparisons show that the computation time per node is about 0.1 second with temperature errors around 0.1°C, which makes the algorithm very attractive for real-time temperature reconstruction.

References

Alifanov, O.M., Determination of Heat Loads from a Solution the Nonlinear Inverse Problem, *High Temperature*, 15(3), 498-504, 1977.

Alifanov, O.M., *Inverse Heat Transfer Problems*, Springer-Verlag, New York, 1994

Beck, J.V., Calculation of Surface Heat Flux from an Internal Temperature History, *ASME Paper* 62-HT-46, 1962

Beck, J.V., Blackwell, B. and St. Clair, C.R., *Inverse Heat Conduction: Ill-posed Problems*, Wiley Interscience, New York, 1985

Blad B., B. Persson and K. Lindstrom. Quantitative Assessment of Impedance Tomography for Temperature Measurements in Hyperthermia. *International Journal of Hyperthermia.* Vol.8, No.1, 33-43, 1992

Bodenhofer, M.A. A Multi-site Perfusion Monitoring Sub-system, *Ph.D. Thesis,* Massachusetts Institute of Technology 1998

Bowman, H.F., W.H. Newman, M.G. Curley, S.C. Summit, S. Kumar, G.T. Martin, J. Hansen and G.K. Svensson. Tumor Hyperthermia: Dense Thermometry, Dosimetry, and Effects of Perfusion. In J.J. McGrath, editor, *Advances in Biological Heat and Mass Transfer,* HTD-volume 189/BED-volume 18, pp 23-31, ASME, 1991

Breedlove, J.J., Heat transfer between blood vessels and perfused tissue during hyperthermia therapy, *Master Thesis,* Massachusetts Institute of Technology 1997

Carslaw, H.S. and J.C. Jaeger. *Conduction of Heat in Solids.* Clarendon Press, Oxford, 1959

Charny, C.K. and R.L. Levin. Three-Dimensional Finite Element Model for the Lower Leg Heating during Hyperthermia. In *26th National Heat Transfer Conference*, Vol.85(269), pp383-388, AIChE, 1989

Chato, J.C., J.J. Eckburg and E. Hurlburt. Comparison of three bioheat transfer models using finite difference techniques. In *Bioheat Transfer – Applications in Hyperthermia, Emerging Horizons in Instrumentation and Modeling,* Volume BED-12, pp17-21. ASME, 1989.

Chen, M.M. and K.R. Holmes. Microvascular Contribution in Tissue Heat Transfer. *Ann. New York Acad. Sci., 335:137-151, 1980*

Chive, M., Use of Microwave Radiometry for Hyperthermia Monitoring and as a Basis for Thermal Dosimetry. In *Methods of Hyperthermia Control,* Editor: M. Gautherie, Chapter 3, pp113-128. Springer-Verlag, Berlin, Germany, 1990

Clegg, S.T., Roemer, R.B., and Cetas, T.C. Estimation of Complete Temperature Fields from Measured Transient Temperatures. *Int. J. Hyperthermia,* Vol. 1, 265-286, 1985

Clegg, S.T. and R.B. Roemer. Toward the Estimation of Three-Dimensional Temperature Fields from Noisy Temperature Measurements During Hyperthermia. *Int. J. Hyperthermia*, vol.5, No.4, 467-484, 1989

DeFord J.A., C.F. Babbs, U.H. Patel, M.W. Bleyer, J.A. Marchosky and C.J. Morgan, Effective estimation and computer control of minimum tumour temperature during conductive interstitial hyperthermia. *International Journal of Hyperthermia,* 7(3): 441-453, 1991

Field, S.B. and Hand, J.W. (editor). *An Introduction to the Practical Aspects of Clinical Hyperthermia.* Taylor & Francis, 1990

Gautherie, M. (editor). *Biological Basis of Oncologic Thermotherapy.* Springer-Verlag, 1990.

Kim, J.C. Instrumented hyperthermia biopsy needle, *B.S Thesis,* Massachusetts Institute of Technology 1998

Kurpisz, K., and Nowak, A.J. *Inverse Thermal Problems.* Computational Mechanics Publications, 1995

Lele, P.P. Physical aspects and clinical studies with ultrasound hyperthermia. In F. K. Storm, Editor, *Hyperthermia in Cancer Therapy,* pp333-367. G.K. Hall & Co., 1983

Martin, G.T., A Thermal Model for Rapid Hyperthermia Therapy Planning and Evaluation. *Ph.D. Thesis,* Massachusetts Institute of Technology 1995

McGough, R.J., E.S. Ebbini, Direct Computation of Ultrasound Phased-Array Driving Signals from a Specified Temperature Distribution for Hyperthermia. *IEEE Transactions on Biomedical Engineering,* Vol.39, No.8, 1992

Moros, E.G., A.W. Dutton, R.B. Roemer, M. Burton and K. Hynynen. Experimental Evaluation of Two Simple Thermal Models Using Hyperthermia in Muscle in *vivo.* Int. J. Hyperthermia, Vol.9, No.4, pp581-598, 1992

Newman, W.H., P.P. Lele, and H.F. Bowman. Limitations and significance of thermal washout data obtained during microwave and ultrasound hyperthermia. *International Journal of Hyperthermia,* 6(4): 771-784, 1990

Newman, W.H., G.T. Martin, D.A. Sidney. Evaluation and Application of the Basis Element Method: A Rapid 3-D Algorithm for Bioheat Transfer Calculations. *Advances in Heat and*

Mass Transfer in Biotechnology – Proceedings of the ASME International Mechanical Engineering Congress and Exposition, HTD322, BED32:49-54, 1995

Nikita, K.S., N. Maratos, NK Uzunoglu, Optimal Steady State Temperature Distribution for a Phased Array Hyperthermia System, *IEEE Trans. Biomed. Eng.* 40(12):1299, 1993

Ocheltree, K.B. and L.A. Frizzell, Determination of Power Deposition Patterns for Localized Hyperthermia: A Steady State Analysis. *Int. Journal of Hyperthermia.* vol.3, No.3, pp269-279, 1987

Pennes, H.H. Analysis of Tissue and Arterial Blood Temperatures in the Resting Human Forearm. *Journal of Applied Physiology.* Vol.1, No.2, pp93-122, 1948

Roemer, R.B., E.G. Moros and K. Hynynen. A comparison of bioheat transfer and effective conductivity equation predictions to experimental hyperthermia data. In *Bioheat Transfer – Applications in Hyperthermia, Emerging Horizons in Instrumentation and Modeling,* Volume BED-12, pp11-15. ASME, 1989.

Sidney, D.A., Three-Dimensional Ultrasound Power Deposition Modeling, Thermal Field Visualization, and Clinical Integration for Hyperthermia Therapy. *Ph.D. Thesis*, Massachusetts Institute of Technology, 1997

Song, C.W., Physiological factors in hyperthermia. *Natl. Cancer Inst. Monogr.*, 61, 169, 1982

Song, W.J.; S. Weibaum, L.M. Jiji and D.E. Lemons, A Combined Macro and Microvascular Model for Whole Limb Heat Transfer. *Journal of Biomechanical Engineering.* Vol.110, pp259-268, 1988

Spiegel, R.J., M.B.E. Fatmi and T.R. Ward. Computer model of animals for hyperthermia studies. In *IEEE Ninth Annual Conference of the Engineering in Medicine and Biology Society*, volume CH2513, pp 1300-1301, 1987

Szajda, K.S. A High Resolution Integrated Circuit Biomedical Temperature Sensing System, *Ph.D. Thesis,* Massachusetts Institute of Technology 1995

Tikhonov, A.N., Inverse Problems in Heat Conduction, *J. Eng. Phys.,* 29(1), 816-820, 1975.

Weinbaum, S; L.M. Jiji and D.E. Lemons, Theory and Experiment for the Effect of Vascular Microstructure on Surface Tissue Heat Transfer: Part I & Part II. *ASME Journal of Biomechanical Engineering.* Vol.106, pp321-341, 1984

Xu, L.X.; M.M. Chen, K.R. Holmes and H. Arkin. The Theorectical Evaluation of the Pennes, the Chen-Holmes and the Weibaum –Jiji Bioheat Transfer Models in the Pig Renal Cortex. *Advances in Biological Heat and Mass Transfer,* Vol. BED-18, pp15-21, ASME, 1991

Zhang Y., T.V. Samulski, W.T. Joines, J. Mattiello, R.L. Levin and D. LeBihan. On the Accuracy of Non-Invasive Thermometry using Molecular Diffusion Magnetic Resonance Imaging. *International Journal of Hyperthermia.* Vol.8, No.2, 263-274, 1992